

RESIN FILM INFUSION (RFI) PROCESS MODELING FOR LARGE TRANSPORT AIRCRAFT WING STRUCTURES

Grant Number NAG-1-1881

Final Report

Period of Performance: December 1, 1996 - December 31, 1997

Alfred C. Loos
Aaron C. Caba
Keith W. Furrow

Department of Engineering Science and Mechanics
Virginia Polytechnic Institute and State University
Blacksburg, VA 24061

August 15, 2000

Prepared For:
Mr. H. Benson Dexter
NASA Langley Research Center
Hampton, VA 23681

ABSTRACT

This investigation completed the verification of a three-dimensional resin transfer molding/resin film infusion (RTM/RFI) process simulation model. The model incorporates resin flow through an anisotropic carbon fiber preform, cure kinetics of the resin, and heat transfer within the preform/tool assembly. The computer model can predict the flow front location, resin pressure distribution, and thermal profiles in the modeled part.

The formulation for the flow model is given using the finite element/control volume (FE/CV) technique based on Darcy's Law of creeping flow through a porous media. The FE/CV technique is a numerically efficient method for finding the flow front location and the fluid pressure. The heat transfer model is based on the three-dimensional, transient heat conduction equation, including heat generation. Boundary conditions include specified temperature and convection. The code was designed with a modular approach so the flow and/or the thermal module may be turned on or off as desired. Both models are solved sequentially in a quasi-steady state fashion.

A mesh refinement study was completed on a one-element thick model to determine the recommended size of elements that would result in a converged model for a typical RFI analysis. Guidelines are established for checking the convergence of a model, and the recommended element sizes are listed.

Several experiments were conducted and computer simulations of the experiments were run to verify the simulation model. Isothermal, non-reacting flow in a T-stiffened section was simulated to verify the flow module. Predicted infiltration times were within 12–20% of measured times. The predicted pressures were approximately 50% of the measured pressures. A study was performed to attempt to explain the difference in pressures.

Non-isothermal experiments with a reactive resin were modeled to verify the thermal mod-

ule and the resin model. Two panels were manufactured using the RFI process. One was a stepped panel and the other was a panel with two 'T' stiffeners. The difference between the predicted infiltration times and the experimental times was 4% to 23%.

Contents

- 1 Introduction** **1**

- 2 Literature Review** **4**
 - 2.1 Flow 4
 - 2.1.1 Analytical Methods 4
 - 2.1.2 Fixed Mesh Methods 5
 - 2.1.3 Moving Mesh Methods 7
 - 2.2 Heat Transfer 8

- 3 Theory** **10**
 - 3.1 Flow Model 10
 - 3.2 Heat Transfer Model 12
 - 3.3 Resin Model 14
 - 3.3.1 Cure Kinetics Sub-Model 15
 - 3.3.2 Viscosity Sub-Model 16

- 4 Finite Element Formulation** **17**
 - 4.1 Galerkin Approximation 17

4.1.1	Flow Model	17
4.1.2	Thermal Model	18
4.2	Finite Element/Control Volume Method	19
4.2.1	Domain Discretization	19
4.2.2	Resin Front Tracking	21
4.2.3	Flow Rate Calculation	23
4.2.4	Fill Factor Calculations	24
4.2.5	Time Step Calculation	24
5	Computer Program	26
5.1	Pre-processing	26
5.2	Processor	28
5.3	Post-processing	31
5.4	Capabilities and Limitations	31
6	Material Characterization	34
6.1	3501-6 Reduced Catalyst Resin Model	34
6.1.1	Cure Kinetics Sub-Model	34
6.1.2	Viscosity Sub-Model	35
6.2	Textile Preform Model	37
6.2.1	Permeability	38
6.2.2	Compaction	39
7	Mesh Refinement Study	42

7.1	Flow and Thermal Model Considerations	43
7.2	Model Description	43
7.2.1	Geometry	45
7.2.2	Boundary Conditions	45
7.2.3	Materials	47
7.3	Procedure	48
7.3.1	Description of the Finite Element Meshes	48
7.4	Thermal Error Calculations	49
7.5	Results	53
7.5.1	Flow Model Convergence	53
7.5.2	Thermal Model Convergence	53
7.6	Discussion	62
7.7	Conclusions	63
7.8	Future Work	65
8	Flow Model Verification	66
8.1	Experiment	67
8.2	Simulation Model	70
8.2.1	Geometry and Boundary Conditions	70
8.2.2	Permeability Calculation	72
8.2.3	Mesh Convergence	73
8.3	Results	75
8.4	Discussion	84

8.4.1	Inlet Pressure	84
8.4.2	Skin, Flange, and Blade Pressures	84
8.4.3	Fill Times	85
9	Stepped Panel Simulation	87
9.1	Experiment	87
9.1.1	Preform and Tooling	87
9.1.2	Procedure	89
9.2	Simulation Model	91
9.2.1	Model Geometry	93
9.2.2	Boundary Conditions	96
9.3	Results	106
9.4	Discussion	106
9.4.1	Temperatures	106
9.4.2	Fill Times	114
9.5	Conclusions	114
10	Two Stiffener Panel	115
10.1	Experiment	115
10.1.1	Preform and Tooling	115
10.1.2	Procedure	122
10.2	Simulation Model	122
10.2.1	Geometry and Mesh	122

10.2.2	Boundary Conditions	126
10.2.3	Materials	127
10.3	Results	131
10.4	Discussion	131
10.4.1	Temperatures	131
10.4.2	Fill Times	137
10.5	Conclusions	138
11	Conclusions and Future Work	139
11.1	Conclusions	139
11.2	Future Work	140
	Bibliography	141
A	Detailed Drawings of Tooling Components	144
A.1	Stepped Panel Tooling Schematics	144
A.2	Two Stringer Panel Tooling Schematics	147
B	Material Properties	153
B.1	Flow Properties	153
B.1.1	FVF	153
B.1.2	Permeability	154
B.2	Thermal Properties	155
B.3	Mechanical Properties	155

List of Figures

1.1	RFI setup.	2
4.1	3-D control volume.	20
4.2	A typical element and the vectors used to calculate the areas of the sub-volumes.	22
4.3	Exploded view of an element showing the eight sub-volumes and their associated vectors.	22
4.4	Actual and numerical flow front.	23
5.1	3DINFIL program flowchart.	29
5.2	Example of PATRAN post-processing capabilities.	32
6.1	In-plane permeability measurement fixture.	39
6.2	Through the thickness permeability measurement fixture.	40
7.1	Mesh refinement model.	44
7.2	Dimensions of the two stiffener preform.	46
7.3	Autoclave temperature cycle.	46
7.4	Mesh for mesh refinement case A.	50
7.5	Mesh for mesh refinement case B.	50

7.6	Mesh for mesh refinement case C.	51
7.7	Mesh for mesh refinement case D.	51
7.8	Mesh for mesh refinement case E.	52
7.9	Temperature measurement points in the mesh refinement model.	55
7.10	Thermal comparison between the different meshes at point 1.	56
7.11	Thermal comparison between the different meshes at point 2.	57
7.12	Thermal comparison between the different meshes at point 3.	58
7.13	Thermal comparison between the different meshes at point 4.	59
7.14	Thermal comparison between the different meshes at point 5.	60
7.15	Thermal comparison between the different meshes at point 6.	61
8.1	Flow verification preform dimensions.	67
8.2	Flow verification preform dimensions.	68
8.3	Pressure transducer locations.	69
8.4	Quarter symmetry finite element mesh.	71
8.5	Flow materials in the flow verification model.	72
8.6	Case A flow front progression.	75
8.7	Case B flow front progression.	76
8.8	Case C flow front progression.	76
8.9	Inlet pressures for different meshes.	77
8.10	Comparison between the measured and model predicted pressures at ports 1 & 4 and 2 & 3.	78
8.11	Comparison between the measured and model predicted pressures at ports 5 & 7 and 6.	79

8.12 Comparison between the measured and model predicted pressures at ports 8 & 9 and 12.	80
8.13 Comparison between the measured and model predicted pressures at ports 10 & 11.	81
8.14 Experimental and predicted infiltration times for the flow verification model.	82
8.15 Percent difference of wet out times for the flow verification model.	83
9.1 Dimensions of the stepped preform.	88
9.2 Tooling and layup of the stepped panel.	89
9.3 Locations of the thermocouples on the stepped preform.	90
9.4 Locations of the FDEMS on the stepped preform.	91
9.5 Locations of the pressure transducers on the stepped preform.	92
9.6 Initial one-element-thick finite element model.	94
9.7 Final three-dimensional finite element model.	95
9.8 Measured autoclave temperatures during the stepped panel run.	97
9.9 Applied temperature cycles for the initial model.	98
9.10 Applied temperature cycles to the top of the final stepped model.	98
9.11 Applied temperature cycles to the bottom of the final stepped model.	99
9.12 Temperature profiles at thermocouple location 1 for various convective coefficients.	100
9.13 Temperature profiles at thermocouple location 2 for various convective coefficients.	101
9.14 Temperature profiles at thermocouple location 4 for various convective coefficients.	102
9.15 Temperature profiles at thermocouple location 5 for various convective coefficients.	103

9.16	Temperature profiles at thermocouple location 6 for various convective coefficients.	104
9.17	Temperature profiles at thermocouple location 7 for various convective coefficients.	105
9.18	Comparison of thermal profiles at point 1.	107
9.19	Comparison of thermal profiles at point 2.	108
9.20	Comparison of thermal profiles at point 4.	109
9.21	Comparison of thermal profiles at point 5.	110
9.22	Comparison of thermal profiles at point 6.	111
9.23	Comparison of thermal profiles at point 7.	112
9.24	Comparison of predicted and measured infiltration times for the stepped panel.	113
10.1	Sketch of the two stiffener preform.	116
10.2	Tooling used to infiltrate the two stiffener panel.	117
10.3	Locations of the FDEM sensors on the two stiffener panel.	118
10.4	Locations of the pressure transducers on the two stiffener panel.	119
10.5	Locations of the thermocouples on the two stiffener panel.	120
10.6	Locations of the thermocouples mounted beneath the base plate and above the surface of the top tooling components.	121
10.7	Mesh used in the initial model of the two stiffener panel. The model is one element thick in the Z direction.	123
10.8	Mesh used in the final model of the two stiffener panel.	124
10.9	Sensor locations in the finite element model.	125
10.10	Measured autoclave temperatures used in the two stiffener model.	128
10.11	Convective boundary conditions on the initial model.	129

10.12	Convective boundary conditions on the final model.	130
10.13	Materials in the two stiffener panel.	130
10.14	Flow front progression in the initial model.	132
10.15	Flow front progression in the final model.	133
10.16	Measured and predicted temperatures at thermocouples 2 and 4.	134
10.17	Measured and predicted temperatures at thermocouple 5.	135
10.18	Predicted and measured infiltration times for the two stiffener panel. . . .	136
A.1	Baseplate.	145
A.2	Detailed drawings of the sensor tap geometry.	146
A.3	Baseplate for the two stiffener panel.	148
A.4	Middle tool for the two stiffener panel.	149
A.5	Sensor locations for the two stiffener panel.	150
A.6	End tool for the two stiffener panel.	151
A.7	Shim for the two stiffener panel.	152

List of Tables

3.1	Values used to calculate the Graetz and Peclet numbers.	14
6.1	3501-6 reduced catalyst high temperature cure kinetics model constants. . .	35
7.1	Permeabilities applied to the mesh refinement model.	47
7.2	Size and run time of the models.	48
7.3	Mesh parameters for case A.	64
7.4	Mesh parameters for case C.	64
8.1	Calculated fiber volume fractions of the T-section.	73
8.2	Three-dimensional flow model fiber volume fractions and permeabilities. . .	74
9.1	Size and Run Time of the Models.	96
10.1	Size and Run Time of the Models.	122
10.2	Correspondence between the locations in the finite element model and the physical sensors.	125
10.3	Permeabilities applied to the two stiffener model.	131

Chapter 1

Introduction

The resin transfer molding (RTM) process is being explored as a cost effective method for producing composite parts. RTM has several advantages over prepreg layup. First, a near net shape dry preform is used. This eliminates the labor required to hand place each layer of prepreg. Second, high dimensional accuracy of the finished part can be attained because matched metal tooling is used. Finally, complex shaped components can be readily fabricated. This allows for incorporation of many components into a single part and helps to reduce the cost and weight of the structure [1].

The RTM process begins with a dry fiber preform. The preform is placed into a matched metal mold and the mold is closed resulting in the compaction of the preform to the specified fiber volume fraction. A liquid thermosetting resin is then injected into the mold. The mold and resin can be preheated before injection, or the mold can be heated after injection to cure the resin. To aid filling of the mold, a vacuum may be applied to remove trapped air.

One of the requirements of the resin is that its viscosity must be low enough throughout the process to fully infiltrate the preform. Since many of the resins currently in use were initially

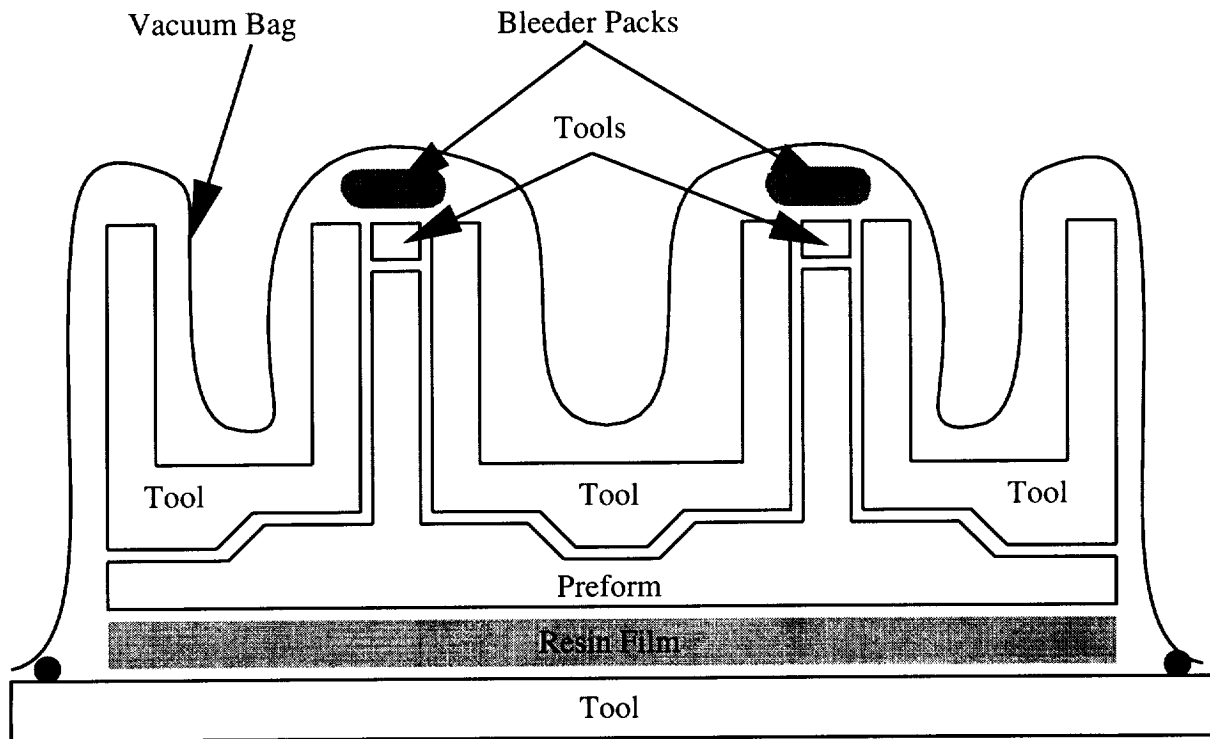


Figure 1.1: RFI setup.

designed for prepreg systems, their viscosity tends to be too high for traditional RTM. To compensate for this, a new process called resin film infusion (RFI) was developed [2]. Instead of injecting the resin into the mold, a sheet of neat resin is cast and placed directly under the preform. Tooling blocks are then placed around the preform, and the whole assembly is vacuum bagged and placed in an autoclave, similar to a prepreg setup. When the autoclave is heated and pressurized, the resin melts, flows into the preform, and is cured. A diagram of this assembly can be seen in Figure 1.1.

RFI has several advantages over RTM. First, the pressure required to compact the preform and drive the resin flow is provided by a single source, the autoclave pressure. Second, high performance resin systems with higher melt viscosities can be used. Finally, infiltration, consolidation, and curing is done in a single step.

Due to the complex nature of the process, optimization of the RFI process cannot be performed using conventional experimentation. The large number of variables makes this approach time and cost prohibitive.

The objective of this work was to develop and verify a comprehensive three-dimensional RTM/RFI simulation model. The model includes the effects of flow through a three-dimensional anisotropic preform, heat transfer through the preform and surrounding tooling, and cure kinetics of the resin. This model was used to confirm the validity of using measured one-dimensional permeabilities as principal permeabilities in a three-dimensional model. The model predictions were also compared to experimental data from both flat and T-stiffened panels. The model results were found to be in good agreement with temperature and flow front location measurements.

The program uses the finite element/control volume (FE/CV) method [3] to track the flow of the resin through the preform. A time dependent finite element scheme is used to calculate the temperatures. The computer models were created in the PATRAN software. Three-dimensional meshes were created and boundary conditions such as specified pressures, vent locations, and heat transfer coefficients were applied. Visualization of the results was also completed using PATRAN.

In Chapter 2 a review of the literature detailing the current state of modeling efforts is undertaken. The theory of the flow, heat transfer, and kinetics models used is discussed in Chapter 3. The finite element formulations used for the flow and heat transfer models are discussed in Chapter 4. The RTM/RFI simulation program is discussed in Chapter 5. Chapter 6 details the models used for the resin and fabric preform. Results from a thermal mesh refinement study are shown in Chapter 7. Comparisons between the model predictions and experimental results are shown in Chapters 8–10.

Chapter 2

Literature Review

Previous studies have dealt with the modeling issues involved with RTM simulation. These include models for the flow of the resin, the heat transfer, and the resin system used. A survey of the current research in these areas will be presented in this chapter.

2.1 Flow

Flow of resin through the preform can be modeled as flow through a porous media. Many studies use Darcy's law to describe the flow [3–7]. Modeling this flow is generally accomplished through one of four basic methods. These methods include analytical methods, finite element, finite difference, and boundary element.

2.1.1 Analytical Methods

Analytical solutions for isothermal filling of simply shaped two dimensional molds have been derived by Cai and Lawrie [8]. The mold is decomposed into simple geometric shapes

and these shapes are filled in succession. Within each section, one-dimensional flow is assumed. Their equations give fill times of each section, and the pressure at the boundaries between each section.

Boccard, Lee, and Springer [9] propose a graphical method for estimating fill times and vent location in thin molds with arbitrary impermeable inserts. The measured and calculated fill times generally agree within 10% and the predicted vent locations were close to the measured vent locations.

Neither of these methods provides the exact location of the flow front within the mold, only fill times are generated. Also, neither can be used if mold filling is non-isothermal and anisotropic. The methods listed in the next two sections can provide data in these situations.

2.1.2 Fixed Mesh Methods

The primary fixed mesh method used is the finite element/control volume (FE/CV) method. To use this method, the mold is first divided into finite elements. Around each nodal location, a control volume is constructed by subdividing the elements into smaller volumes. These control volumes are used to track the location of the flow front [1].

Many FE/CV implementations have been developed to model the resin flow in an RTM process. Fraccia, Castro, and Tucker [3] implemented a FE/CV technique to model the isothermal flow of resin in two-dimensional RTM molds. Predicted flow front locations were compared to measured flow fronts in a two-dimensional mold. Fairly close agreement was found. Several runs were also made with models of an automobile hood, and the effect of gate location and in-plane permeability variation on the flow front advancement was observed.

Voller and Peng [10] used a two-dimensional, isothermal volume of fluid approach. An iterative solver is used to determine the fill factors for each time step. An arbitrarily large time step can be used, and multiple volumes can be filled in each time step. Results were compared to analytical solutions and other numerical methods. Their method agrees with both.

Gauvin et al. [6] implemented the FE/CV technique to model isothermal flow in an RTM subway seat. Several 'short shots' were made where the mold was partly filled with resin and then allowed to cure. This was intended to show the actual location of the flow front in the mold. Comparison of the model to the 'short shots' showed discrepancies in the flow front locations. These were attributed to difficulty in predicting the permeability in the corners where the preform was bent. They also noted that small local variations in the permeability can have a large global effect.

A two-dimensional, isothermal, FE/CV model was tested by Calhoun et al. [11]. A picture frame with converging flow to a center vent was modeled. A constant viscosity resin and a constant velocity source were used. The simulation time matched the experimental fill time within 1%. The pressure data could only be matched through the use of various scaling factors. The discrepancy was attributed to difficulties in measuring the permeabilities.

Loos and MacRae [7] used a two-dimensional RFI simulation with heat transfer and a reactive resin to optimize the autoclave cycle for a T-stiffened panel. Both the preform and the surrounding tooling were modeled. The original cycle resulted in incomplete filling of the part. Using the model, a suitable cure cycle was found that resulted in complete infiltration of the part.

Lee, Young, and Lin [12] have a two-and-a-half-dimensional code where flow is modeled as two-dimensional and heat transfer is modeled as three-dimensional. A RTM automobile hood with multiple cut-outs was simulated. Pressure contours for two different inlet po-

sitions were shown. Flow front position was also used to predict where weld lines would form in the molded part.

Young [13] developed a three-dimensional non-isothermal model of the RTM process. Formulation for a wedge element is given. Simulation results are given for flow and cure in a cube and a T-section.

Loos et al. [14] have developed a three-dimensional non-isothermal model of the RFI process. A model of a T-stiffened panel with a variable thickness skin was compared to experimental results. The model included both the preform and the tooling components. Flow front location and degree of cure were measured using frequency dependent electromagnetic sensors (FDEMS). Temperatures were measured using thermocouples. Close agreement was found for the temperature, viscosity, and degree of cure. Wet out occurred simultaneously for all FDEMS sensors on the surface of the skin, while the simulation predicted sequential wet out. Discrepancies between the predicted and measured flow front was attributed to premature wet-out of the FDEMS sensors due to resin flowing between the preform and tool.

2.1.3 Moving Mesh Methods

Another method of tracking the flow is to have the numerical grid deform and move with the flow front. One moving mesh method is the boundary element method. Yoo and Lee [15] use the boundary element method to simulate a two-dimensional mold filling process. An automatic meshing scheme was employed to track the flow front where the nodes on the flow front move to track the shape of the front. When the nodes move, nodes that are close to the mold boundary may move outside the mold wall. This will result in some mass loss from the system as the fluid that has moved outside the wall is neglected. Viscosity of the

resin was isothermal and varied as a function of time only. Filling of a center-gated square mold and an ‘L’ shaped mold were simulated. A small mass loss of 3–4% was reported in both cases. An advantage of this method is the accuracy of the flow front position since it is determined exactly. Disadvantages of this method include difficulty with multiple gates and weld lines [15].

Another moving mesh method is the body fitted coordinate method. This is a finite difference method where a curvilinear coordinate system is fit onto the physical domain. An irregular mesh in the physical domain is converted into a regular mesh in the transformed domain. Friedrichs and Güçeri [5] used a two/three-dimensional hybrid code to model the flow in a T-stiffened panel. The three-dimensional formulation is only used near where the base of the T joins the skin. The two-dimensional code is used where out of plane flows can be neglected, e.g. flow in the skin and stiffener away from the T joint. Results presented include the computational meshes used at various times in the simulation, velocity distributions, and tracer particle paths.

2.2 Heat Transfer

The energy balance in a single phase material is well understood, but the balance equations for multi-phase systems are less readily available [16]. Two approaches are taken in the literature. The first uses a single lumped temperature field for both the resin and preform. In the second approach, separate governing equations are written for the resin and preform. The two governing equations are coupled together through a heat exchange term of the form [17]

$$q = h_f (T_r - T_f) \quad (2.1)$$

where q is the rate of heat exchange between the fiber and resin, h_f is the heat transfer coefficient between the fiber and resin, and T_f and T_r are the temperatures of the fiber and resin, respectively. If the flow rates are fast, or the thermal gradients are large, the two phase model is necessary to account for the finite heat transfer rate between the fiber and resin. For slow flows, the resin and fiber temperatures will have time to equilibrate, and only a single temperature model is necessary.

Lin, Lee, and Liou [18] performed non-isothermal molding experiments on a center gated disc. For flow speeds of up to 12 cm/s they found better correlations with the two phase model.

Loos et al. [14] state that in their RFI process model, the temperatures calculated for the resin and fiber were almost identical, and a lumped model should be used. The reason given was that the flow rates are very slow.

Chapter 3

Theory

The RFI and RTM processes consist of three concurrent phenomena: flow of the resin through the preform, heat transfer through the tools and the preform, and curing of the resin. Each of these is developed as a separate model in this chapter.

3.1 Flow Model

In any model of the RFI or RTM processes, one of the most important aspects is tracking the flow of the resin through the preform. The three-dimensional flow model was developed to calculate the pressure and velocity fields in the fluid and track the flow front position. This formulation is patterned after Davé [4]. The assumptions made in the formulation of the model include:

1. The preform is a heterogeneous, porous, anisotropic medium.
2. The flow is quasi-steady state.
3. Capillary and inertial effects are neglected (low Reynolds number flow).

4. The fluid is assumed to be Newtonian (its viscosity is independent of shear rate), and incompressible.
5. The fluid does not leak from the mold cavity.

The continuity equation for the fluid can be written as:

$$\frac{\partial v_i}{\partial x_i} = 0 \quad (3.1)$$

where v_i is the interstitial velocity vector.

As the fluid flows through the pores of the preform, the interstitial velocity of the resin can be written as:

$$v_i = \frac{q_i}{\phi} \quad (3.2)$$

where q_i is the superficial velocity vector and ϕ is the porosity of the solid. The porosity was assumed to be constant in this investigation.

Using the assumptions that the preform is a porous medium and that the flow is quasi-steady state, the momentum equation can be replaced by Darcy's law:

$$q_i = -\frac{S_{ij}}{\mu} \frac{\partial P}{\partial x_j} \quad (3.3)$$

where μ is the fluid viscosity, S_{ij} is the permeability tensor of the preform, and P is the fluid pressure.

Noting that the resin is incompressible and substituting (3.3) into (3.1) gives the governing differential equation of the flow:

$$\frac{\partial}{\partial x_i} \left(\frac{S_{ij}}{\mu} \frac{\partial P}{\partial x_j} \right) = 0 \quad (3.4)$$

This second order partial differential equation can be solved when the boundary conditions are prescribed. Two common boundary conditions for the inlet to the mold are either a prescribed pressure condition:

$$P_{inlet} = P_{inlet}(t) \quad (3.5)$$

or a prescribed flow rate condition:

$$Q_n(t) = n_i \frac{S_{ij}}{\mu} \frac{\partial P}{\partial x_j} \quad (3.6)$$

where Q_n is the volumetric flow rate and n_i is the normal vector to the inlet. The boundary condition along the flow front is taken to be one of zero pressure:

$$P_{flowfront} = 0 \quad (3.7)$$

Since the resin cannot through the the mold wall, the final boundary condition necessary to solve Equation (3.4) is that the velocity normal to the wall at the boundary of the mold must be zero:

$$\bar{v} \cdot \bar{n} = 0 \quad (3.8)$$

where \bar{n} is the vector normal to the mold wall.

3.2 Heat Transfer Model

In the RFI process, the heating rates and flow rates are small compared to the RTM or SRIM processes. This allows a number of simplifying assumptions to be made in the thermal analysis. First, the bagged preform and tooling assembly are heated in the autoclave at a low heating rate, usually no greater than 5°C/min. During infiltration, the temperature difference between the resin and the preform is small, thus the volumetric heat transfer

between the resin and the preform can be neglected. Second, since the flow velocities of the resin are small, heat transfer due to convection can be ignored. This can be expressed mathematically with the Graetz and Peclet numbers listed by Tucker [16]. The Graetz number can be interpreted as the flow direction convection divided by the transverse conduction. The Graetz number is given by Equation (3.9):

$$Gz = \frac{qh^2}{\alpha_t L} \quad (3.9)$$

where q is the superficial resin speed, h is half of the mold thickness, L is the characteristic flow length, and α_t is the total thermal diffusivity defined as $(k_{zz}/(\rho c_p))$, with k_{zz} representing the total effective conductivity in the thickness direction and ρ and c_p are the density and specific heat of the resin, respectively.

The Peclet number can be interpreted as the ratio of dispersion to conduction, and is given by Equation (3.10).

$$Pe = \frac{qd_p}{\alpha_t} \quad (3.10)$$

where d_p is the diameter of a single fiber.

Using data from the two stiffener panel modeled in Chapter 10, the Graetz and Peclet numbers were calculated. Table 3.1 lists the values used in the calculations. Since the Graetz and Peclet numbers are <1 , dispersion and convection can be neglected, and the entire model can be described by one temperature field.

The heat transfer in the RFI process model is based on the three-dimensional transient heat conduction equation, including a term for heat generation:

$$\rho c_p \frac{\partial T}{\partial t} - \frac{\partial}{\partial x_i} \left(k_{ij} \frac{\partial T}{\partial x_j} \right) - \rho \dot{H} = 0 \quad (3.11)$$

where ρ is the density, c_p is the specific heat, k_{ij} is the thermal conductivity tensor for an anisotropic material, and \dot{H} is the heat generation due to exothermic chemical reactions.

Table 3.1: Values used to calculate the Graetz and Peclet numbers.

Variable	Value	Units
k_{zz}	0.51	W/(mK)
$2h$	0.01753	m
L	0.8255	m
d_p	8×10^{-6}	m
q	2.58×10^{-5}	m/s
ρC_p	2.504×10^6	J/(m ³ °C)
Gz	0.28	
Pe	0.009	

In order to solve Equation (3.11), the initial temperature distribution must be given:

$$T(\bar{x}, 0) = T_{init}(\bar{x}) \quad (3.12)$$

where \bar{x} is a position vector.

Boundary conditions for the solution of Equation (3.11) include:

$$\text{Specified Temperatures:} \quad T(\bar{x}, t) = T_{spec}(\bar{x}, t) \quad (3.13)$$

$$\text{Convection:} \quad \left(k_{ij} \frac{\partial T}{\partial x_j} \right) n_i = h(T_\infty - T) \quad (3.14)$$

$$\text{Specified Flux:} \quad \left(k_{ij} \frac{\partial T}{\partial x_j} \right) n_i = \hat{q} \quad (3.15)$$

$$\text{Insulated:} \quad \left(k_{ij} \frac{\partial T}{\partial x_j} \right) n_i = 0 \quad (3.16)$$

where h is the convection coefficient and \hat{q} is the specified flux.

3.3 Resin Model

The RFI process uses thermosetting polymeric resins. As the process progresses, the resin begins to cure, change viscosity, and produce heat through exothermic chemical reactions.

A model is necessary to predict the degree of cure and the heat liberated from the curing resin.

3.3.1 Cure Kinetics Sub-Model

In order to model the cure of the resin, a relationship must be found that gives the cure as a function of time. If the assumption is made that the rate of heat generation during cure is proportional to the rate of the cure reaction, then the degree of cure of the resin can be defined as:

$$\alpha(t) = \frac{H(t)}{H_R} \quad (3.17)$$

where $H(t)$ is the heat evolved from the beginning of the reaction to some intermediate time, t , and H_R is the total heat of reaction during cure. To find an expression for the rate of heat generation, we differentiate and rearrange Equation (3.17) to give:

$$\dot{H} = \frac{d\alpha}{dt} H_R \quad (3.18)$$

where $d\alpha/dt$ is defined as the reaction or cure rate. For a thermosetting resin, the cure rate depends on the temperature and degree of cure. A typical expression for the cure rate is given as follows:

$$\frac{d\alpha}{dt} = f(T, \alpha)(1 - \alpha)^n \quad (3.19)$$

where $f(T, \alpha)$ is a function that depends on the reaction type. The function is usually of the form:

$$f(T, \alpha) = k_1 + k_2 \alpha^m \quad (3.20)$$

where k_1 and k_2 are the rate constants. The temperature dependence of the rate constants is given by an Arrhenius-type expression:

$$k_i = A_i \exp \left[\frac{-E_i}{RT} \right] \quad (3.21)$$

where A_i is the Arrhenius pre-exponential factor, E_i is the Arrhenius activation energy, R is the gas constant, and T is the absolute temperature. Values for these constants can be found using a procedure similar to the one in Chen and Macosko [19].

If diffusion of chemical species and convection of the fluid is neglected, the degree of cure at each point inside the material can be determined by integrating the expression for the cure rate with respect to time in the following manner:

$$\alpha = \int_0^t \left(\frac{d\alpha}{dt} \right) dt \quad (3.22)$$

3.3.2 Viscosity Sub-Model

To accurately predict the resin infiltration into the preform, the viscosity of the resin must be known as a function of both position and time. Resin viscosity is a complex function of shear rate, temperature, and degree of cure and no analytical models exist to adequately describe this relation. However, a reasonable approach is to assume that the resin is a Newtonian fluid, and to measure the viscosity at low shear rates. The measured viscosities can then be fit to a mathematical expression relating temperature and time to viscosity, and the resulting formula can be used in the numerical calculations. The formula given by Castro and Macosko [20] is used:

$$\mu(T, \alpha) = \mu_0(T) \left[\frac{\alpha_g}{\alpha_g - \alpha} \right]^{A(T)+B(T)\alpha} \quad (3.23)$$

where μ is the viscosity, μ_0 is the viscosity at zero cure, T is the temperature, α_g is the degree of cure at gel, α is the degree of cure, and A and B are parameters which depend on temperature.

Chapter 4

Finite Element Formulation

Using the governing equations derived in Chapter 3, a finite element formulation is derived for the flow and heat transfer models.

4.1 Galerkin Approximation

4.1.1 Flow Model

In Chapter 3, the governing equation for the flow model was found to be

$$\frac{\partial}{\partial x_i} \left(\frac{S_{ij}}{\mu} \frac{\partial P}{\partial x_j} \right) = 0 \quad (3.4)$$

Using the procedure outlined by Reddy [21] the finite element formulation of Equation (3.4) was found to be:

$$[K_{ij}^e] \{P_j^e\} = \{F_i^e\} \quad (4.1)$$

where

$$K_{ij}^e = \int_{\Omega_e} \frac{S_{\alpha\beta}}{\mu} \frac{\partial \Psi_i}{\partial x_\alpha} \frac{\partial \Psi_j}{\partial x_\beta} d\Omega \quad (4.2)$$

$$F_i^e = \int_{\Omega_e} f \Psi_i d\Omega + \int_{\Gamma_e} Q_n \Psi_i d\Gamma \quad (4.3)$$

Here Ω_e is the domain of an element, Γ_e is the surface of an element, P_j^e is the pressure at each node, f is a volumetric source term, Q_n is a specified fluid flux through the face of the element, and Ψ_i is a linear interpolation function.

4.1.2 Thermal Model

The governing equation for the transient heat transfer was found in Chapter 3 to be:

$$\rho c_p \frac{\partial T}{\partial t} - \frac{\partial}{\partial x_i} \left(k_{ij} \frac{\partial T}{\partial x_j} \right) - \rho \dot{H} = 0 \quad (3.11)$$

Using the procedure outlined in Reddy [21] the finite element formulation was found to be:

$$[M_{ij}^e] \{ \dot{T}_j^e \} + [K_{ij}^e] \{ T_j \} = \{ F_i^e \} \quad (4.4)$$

where

$$M_{ij}^e = \int_{\Omega_e} \rho c_p \Psi_i \Psi_j d\Omega \quad (4.5)$$

$$K_{ij}^e = \int_{\Omega_e} k_{\alpha\gamma} \frac{\partial \Psi_i}{\partial x_\alpha} \frac{\partial \Psi_j}{\partial x_\gamma} d\Omega + \int_{\Gamma_1} h \Psi_i \Psi_j d\Gamma \quad (4.6)$$

$$F_i^e = \int_{\Gamma_1} h T_\infty \Psi_i d\Gamma + \int_{\Gamma_2} \hat{q} \Psi_i d\Gamma + \int_{\Omega_e} \rho \dot{H} \Psi_i d\Omega \quad (4.7)$$

Here, h is the convection coefficient, \hat{q} is the specified flux through a face of the element, and $\rho \dot{H}$ is the volumetric heat generation due to exothermic chemical reactions.

To solve Equation (4.4), a weighted average of the time derivative of the temperature at two consecutive time steps is used [21]:

$$(1 - \theta) \dot{T}_s + \theta \dot{T}_{s+1} = \frac{T_{s+1} - T_s}{\Delta t_{s+1}} \quad (4.8)$$

A value of $\theta = 0.887$ was chosen because it gives good accuracy with reasonably sized time steps [22].

4.2 Finite Element/Control Volume Method

In order to solve Equations (4.1) and (4.4) the domain of interest needs to be discretized in both space and time. For the reasons stated in Chapter 2 a Finite Element/Control Volume (FE/CV) approach was chosen for this study.

4.2.1 Domain Discretization

In order to track the moving flow front in the flow model, a technique is used that is based on the assumption that each node in the mesh can be surrounded by a “control volume” that is composed of a collection of sub-volumes from surrounding elements. The size and shape of each control volume is determined by the number of nodes in each adjacent element. This study used a structured mesh of 8-noded “brick” elements.

The flow domain is first discretized using finite elements, and then each element is further divided into eight sub-volumes. Each sub-volume is associated with one of the nodes on the element. The control volume for a particular node is composed of all of the sub-volumes associated with that node. An example of a control volume composed of individual sub-volumes is shown in Figure 4.1.

The flow calculations require the volume of the control volumes and the areas of the internal faces of all sub-volumes. To find the areas, six vectors are constructed that start at the centroid of the element and end at the center of each face of the element. These vectors

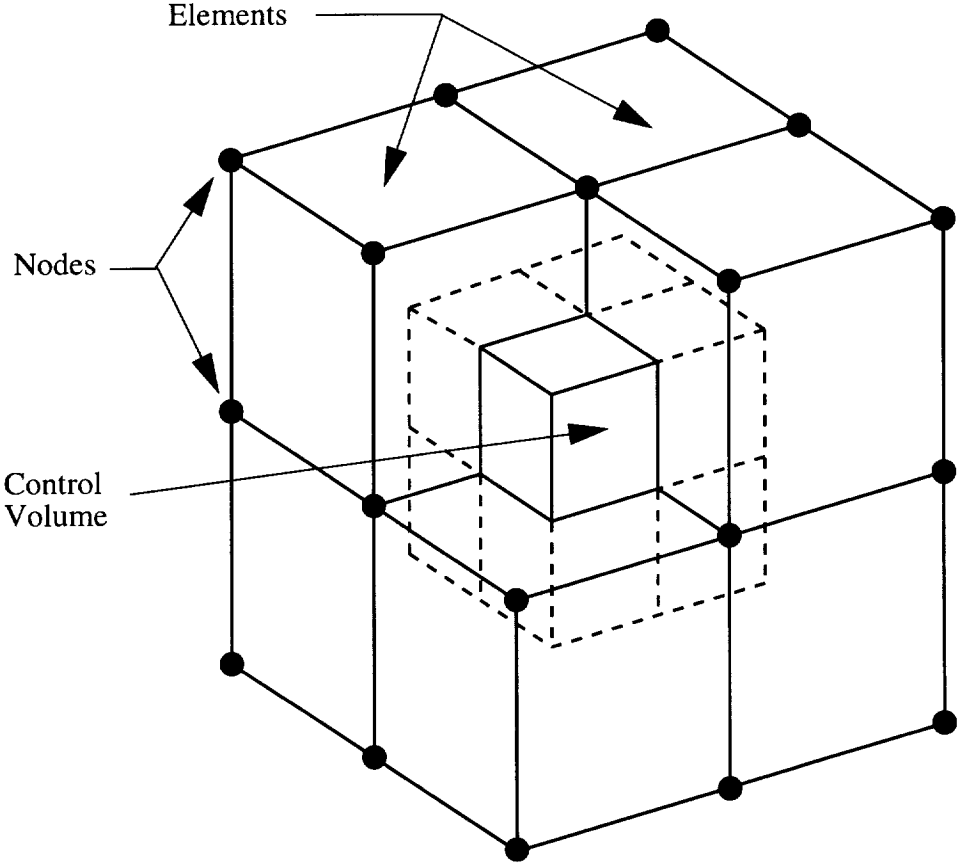


Figure 4.1: 3-D control volume.

and sub-volumes are shown in Figures 4.2 and 4.3, respectively. The area vector of each sub-volume is calculated by first using cross products to find the area of each internal face, then the total area vector is constructed by summing the individual area vectors. This procedure is summarized in Equations (4.9)–(4.16):

$$\bar{a}_{e1} = \bar{y}_2 \times \bar{z}_2 + \bar{z}_2 \times \bar{x}_2 + \bar{x}_2 \times \bar{y}_2 \quad (4.9)$$

$$\bar{a}_{e2} = \bar{z}_2 \times \bar{y}_2 + \bar{y}_2 \times \bar{x}_1 + \bar{x}_1 \times \bar{z}_2 \quad (4.10)$$

$$\bar{a}_{e3} = \bar{y}_1 \times \bar{z}_2 + \bar{z}_2 \times \bar{x}_1 + \bar{x}_1 \times \bar{y}_1 \quad (4.11)$$

$$\bar{a}_{e4} = \bar{z}_2 \times \bar{y}_1 + \bar{y}_1 \times \bar{x}_2 + \bar{x}_2 \times \bar{z}_2 \quad (4.12)$$

$$\bar{a}_{e5} = \bar{z}_1 \times \bar{y}_2 + \bar{y}_2 \times \bar{x}_2 + \bar{x}_2 \times \bar{z}_1 \quad (4.13)$$

$$\bar{a}_{e6} = \bar{y}_2 \times \bar{z}_1 + \bar{z}_1 \times \bar{x}_1 + \bar{x}_1 \times \bar{y}_2 \quad (4.14)$$

$$\bar{a}_{e7} = \bar{z}_1 \times \bar{y}_1 + \bar{y}_1 \times \bar{x}_1 + \bar{x}_1 \times \bar{z}_1 \quad (4.15)$$

$$\bar{a}_{e8} = \bar{y}_1 \times \bar{z}_1 + \bar{z}_1 \times \bar{x}_2 + \bar{x}_2 \times \bar{y}_1 \quad (4.16)$$

where \bar{a}_{en} are the area vectors for node ‘n’ on element ‘e’ and \bar{v}_i are the vectors shown in Figure 4.2.

4.2.2 Resin Front Tracking

The control volumes can be either empty, partially full, or completely full. The amount of fluid in each control volume is monitored by a quantity called the fill factor. It is a ratio of the volume of fluid in the control volume to the total volume of the control volume. The fill factor takes on values from 0 to 1 where 0 represents totally empty and 1 represents totally full. The control volume method tracks the flow front by determining which control volumes are partially full and connecting them to form the flow front. The numerical flow front is constructed of the nodes that have partially full control volumes as shown in Figure 4.4. The location of the fluid in the control volume is not known so the exact shape of the flow front is not known, and the resolution of the flow front is determined by the

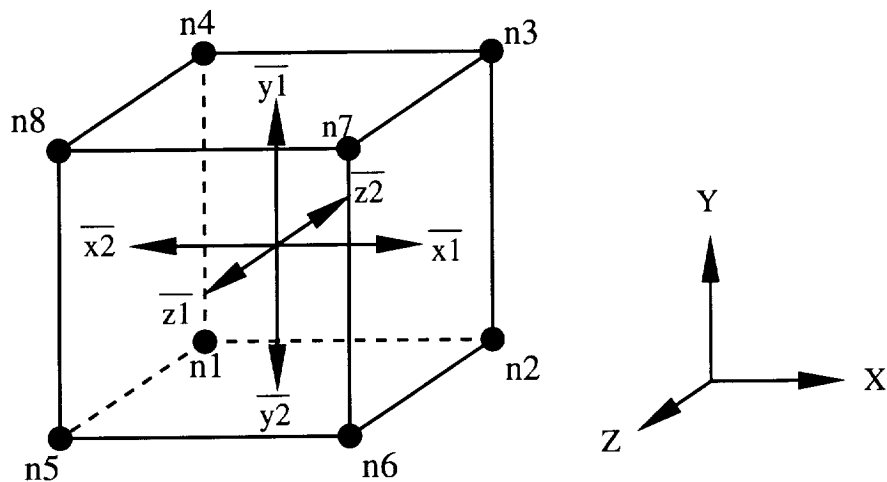


Figure 4.2: A typical element and the vectors used to calculate the areas of the sub-volumes.

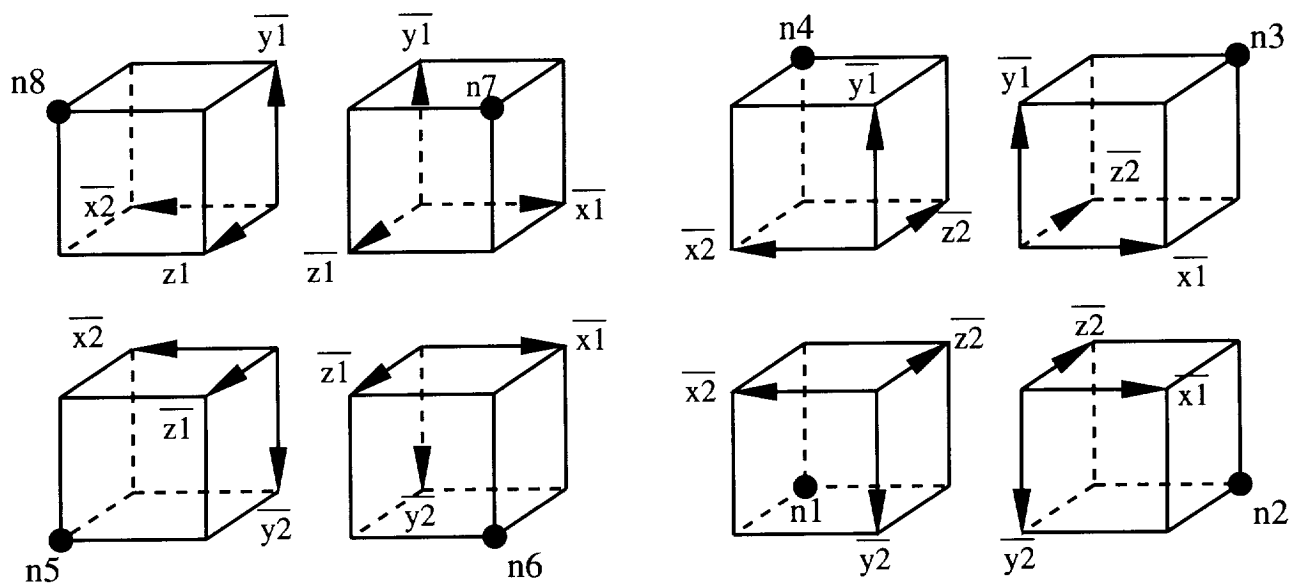


Figure 4.3: Exploded view of an element showing the eight sub-volumes and their associated vectors.

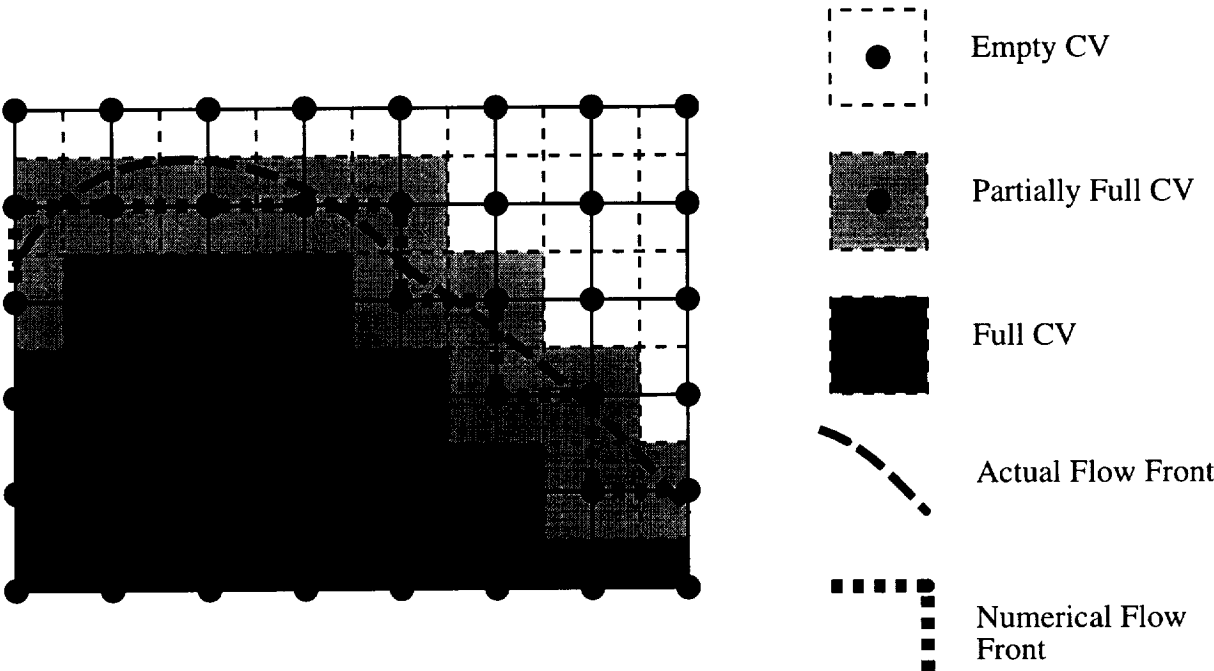


Figure 4.4: Actual and numerical flow front.

mesh density. A detailed discussion of flow front recovery can be found in [23].

4.2.3 Flow Rate Calculation

Once the domain has been discretized, the pressures in the preform must be calculated. The boundary conditions listed in Equations (3.5)–(3.8) must be applied. To approximate the zero pressure boundary condition at the actual flow front, the nodes on the numerical flow front have their pressures set to zero. Next, the other boundary conditions such as specified pressure and specified flow rate are applied, and then Equation (4.1) is solved to find the pressure distribution in the preform.

After the pressures have been calculated, the velocities are calculated at the centroid of

each element using Darcy's law:

$$v_i = -\frac{1}{\phi} \frac{S_{ij}}{\mu} \frac{\partial P}{\partial x_j} \quad (4.17)$$

It is assumed that the velocity of the fluid is constant throughout each element.

The flow into each nodal control volume from each element can be found with:

$$Q_{en} = \bar{v}_e \cdot \bar{a}_{en} \quad (4.18)$$

where Q_{en} is the volumetric flow rate into control volume (n) from element (e), \bar{v}_e is the fluid velocity in the element, and \bar{a}_{en} is the area vector for the sub-volume as calculated in Section 4.2.1.

4.2.4 Fill Factor Calculations

After the flow rates into each control volume have been calculated the fill factors can be updated. Given the current time step, the fill factors from the previous step, the calculated flow rate, and the volume of each CV, the new fill factors can be calculated with:

$$f_n^{i+1} = f_n^i + \frac{\Delta t \sum_e Q_{en}}{V_n} \quad (4.19)$$

where f_n is the fill factor, Δt is the time step, V_n is the volume of the control volume, and the superscripts indicate time level.

4.2.5 Time Step Calculation

The time step for the next iteration must be calculated before the solution can proceed. The optimal time step would be where the fluid just fills one control volume. If a larger

step were chosen, the flow front would over-run the control volume and a loss of mass from the system would result. The time to fill the partially full control volume 'n' is calculated with the following relation:

$$\Delta t_n = \frac{(1 - f_n)V_n}{\sum_e Q_{en}} \quad (4.20)$$

Once Δt_n has been calculated for all the partially full control volumes, the smallest Δt_n is chosen as the time step for the next iteration.

Chapter 5

Computer Program

Using the theory developed in Chapter 3 and the finite element formulations developed in Chapter 4, a computer program called 3DINFIL was written to simulate the RTM/RFI process. This chapter will discuss pre-processing, processing, and post-processing of a model.

5.1 Pre-processing

The computer program requires three input files. The first file contains the flow model, the second contains the thermal model, and the third contains the parameters necessary to run the simulation.

The finite element model is constructed using 8-noded hexahedral brick elements. PATRAN was used to create the model files. The PATRAN model consists of geometry, a finite element mesh, materials, and boundary conditions. First the geometry is constructed and meshed. Then material properties are defined and boundary conditions are applied. Finally the model is saved in PATRAN 2.4 neutral file format. The program requires that

the model files be in PATRAN neutral file format.

For the flow model, only the preform region and possibly any bleeder packs are considered. The material properties required are the three-dimensional permeability tensors of the preform and bleeder packs. Allowable boundary conditions include: specified pressure, vent locations, specified flow rates, and pressure cycle flags. Also, any initially filled nodes are specified. If multiple injection ports are used, different pressure cycles can be supplied for each injection port. Pressure cycle flags are used to determine which cycle is applied to the element.

The second model is the heat transfer model. This model includes the preform and any tooling that surrounds it. The three-dimensional thermal conductivity tensors of each material must be specified. A temperature distribution is input as the only initial condition. The boundary conditions include either convective coefficients or specified temperatures, and temperature cycle flags. The code will accept multiple temperature cycles, and the cycle flags specify which cycle is applied to which element. Only one type of thermal boundary condition is allowed in each model. The model must have either convective type boundary conditions or specified temperature boundary conditions.

Both the flow and heat transfer models must use the same mesh in the preform region. When building these two models care must be taken to ensure a one-to-one correspondence between the nodes and elements in the flow model and the nodes and elements in the preform region of the heat transfer model.

The third file that must be created is the `3dinit.inp` file. This file contains time limit and iteration limit specifications, the initial viscosity, and the pressure and temperature cycles.

5.2 Processor

The processor is composed of the three sub-models: the flow model, the heat transfer model, and the resin model. All three models are coupled and non-linear. The flow model needs the viscosity from the resin model, the resin model needs the temperatures from the heat transfer model, and the heat transfer model uses the heat generation from the resin model. Instead of trying to directly solve this system, the sub-models are solved sequentially. In addition, each sub-model is solved in a piecewise linear fashion. This not only reduces the coding and solution effort, it allows the code to be in a ‘modular’ form, with each sub-model in its own module. This way each module can be turned on and off individually depending on the particular analysis being performed.

The program is divided into six sections:

1. Initialization
2. Flow Calculations
3. Update Variables
4. Thermal Calculations
5. Termination Conditions
6. Final Output and Exit

Each section performs its calculations and passes necessary information on to the other sections. A flow chart of the program is shown in Figure 5.1.

The initialization section begins by reading the three files created during pre-processing: the flow model, thermal model, and processing cycle. After the finite element information has been read from the model files, the code calculates the control volumes as discussed in Section 4.2.1. Also included in this section of the code is initialization of variables, including

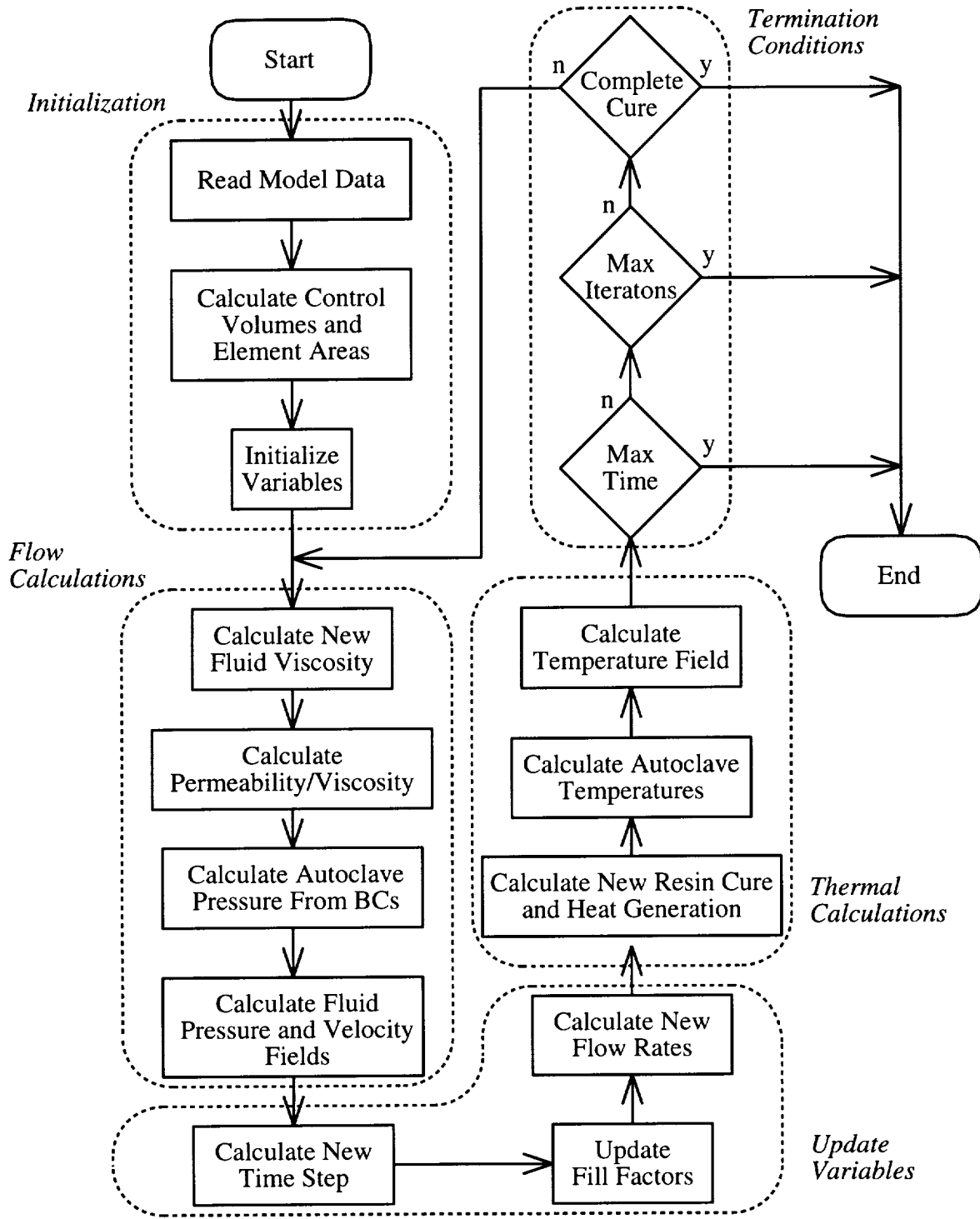


Figure 5.1: 3DINFIL program flowchart.

assigning an initial degree of cure to each node, assigning thermal material properties to all elements, and assigning permeabilities and porosities to the preform elements.

Once the initialization section is complete, the code begins the main iteration loop. The first section in this loop contains the flow calculations. The purpose of this section is to calculate the pressure field in the preform using the viscosity, permeability, and applied pressure. The viscosity at each node and in each element is calculated using the current temperature and degree of cure. All references to permeability in Equation (4.2) have the permeability divided by the viscosity, so this quantity is calculated and recorded for each element that has fluid in it. Next, the autoclave pressure is calculated from the profile given in the `3dinit.inp` file and this pressure is applied to the preform where the pressure cycle flags were applied. Finally, the boundary conditions are applied, and the pressure field is calculated using Equation (4.1).

To save storage space, the stiffness matrix [K_{ij} in Equation (4.1)] is stored in a sparse storage format. The code currently uses the NASA Vector Sparse Solver (VSS) to solve the equations [24].

Once the pressure field has been calculated, the pertinent model variables must be updated for the next iteration. The flow rates are found and the fill factors are updated. Next, a new time step is calculated for the next iteration.

In the thermal calculation section, the code calls the cure subroutine to calculate the degree of cure of the resin, and the rate of heat generation. The code then calculates the current autoclave temperatures, based on the thermal cycle profiles input in the `3dinit.inp` file. Finally, the boundary conditions are applied and the temperature field is calculated. Since the equation used to solve for the temperature field, Equation (4.8), contains the time step, the mass matrix (M_{ij}) and the thermal stiffness matrix (K_{ij}) must be recalculated each time step.

Similar to the flow computations, the stiffness matrix is stored using a sparse storage format, and the solution is found with the NASA VSS solver.

Finally, the code checks to see if any program termination conditions have been met. Conditions that will cause the code to end calculations are reaching the maximum simulation time, maximum iterations, or complete cure of the resin. If any of these conditions are met, the code exits, otherwise another iteration begins.

While the code is running, results are written to disk. This allows the user to check the progress of the solution, and prevents complete loss of information in the event of a computer crash. After the calculations are complete, the program writes a PATRAN session file that the user can run to automatically load the results into PATRAN.

5.3 Post-processing

PATRAN was used to post-process the results from the simulation runs. An example of the PATRAN output is shown in Figure 5.3.

5.4 Capabilities and Limitations

Since the program was written in standard Fortran 77, it has proven to be easily portable to different computers and operating systems. Currently, the code has been successfully ported to Silicon Graphics, HP, and Cray computers.

The code has been written in a modular form. As new resin systems are characterized, they can be easily added to the model. Experience has shown that a significant amount of the run time is spent in the solver subroutines. As faster or machine specific solvers

MSC/PATRAN Version 6.0 05-Sep-97 17:29:04
FRINGE: t-sec/verify/case3, 3dflowptnod: Flow Front Position -PATRAN 2.5

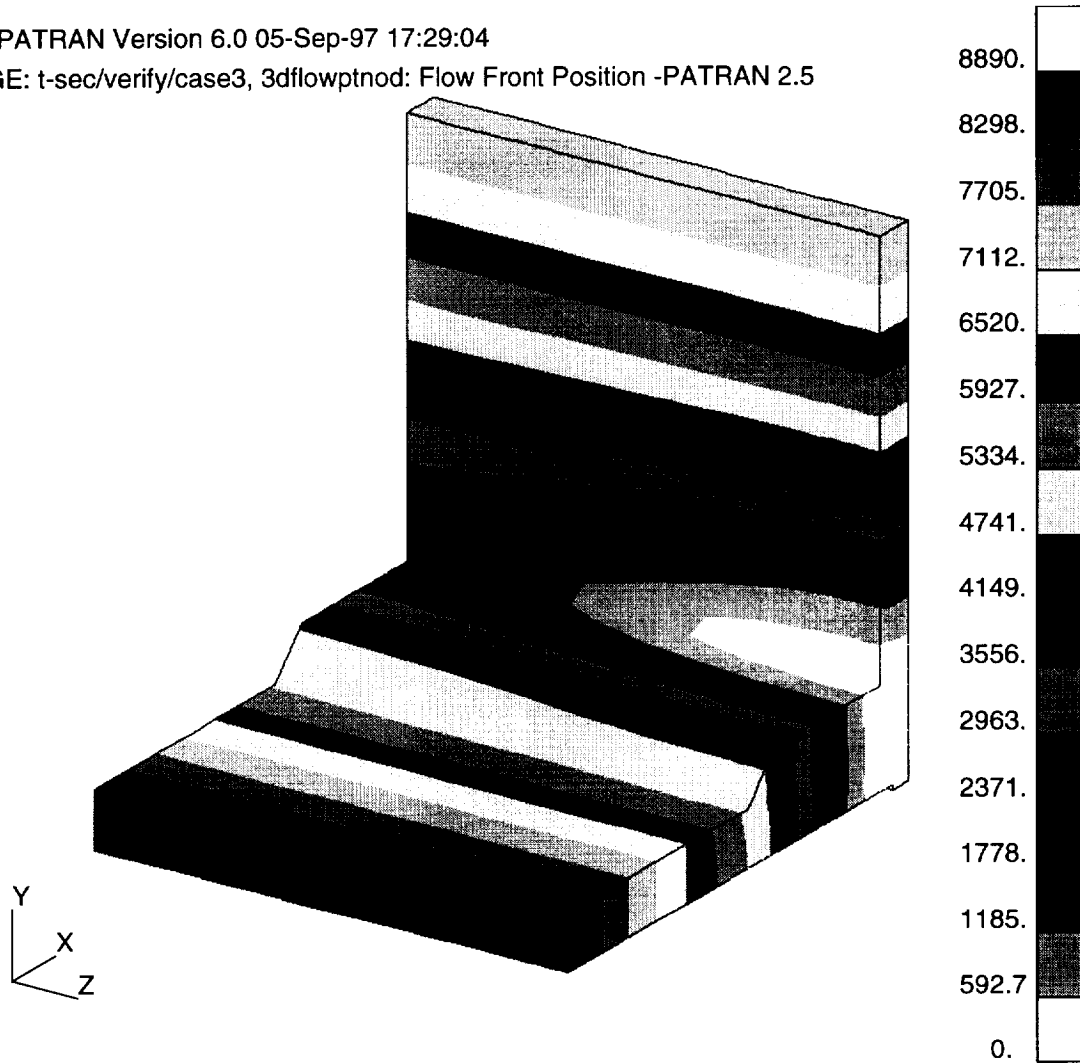


Figure 5.2: Example of PATRAN post-processing capabilities. This figure shows the flow front progression in a center port injected, T-stiffened model. The color bands represent the flow front location at different times. The units are in seconds.

become available, the solver can easily be replaced by changing a few lines of code.

As with any simulation program, without correct inputs, correct results cannot be expected. The many variables that are required by this simulation model must be accurately specified before this simulation model can be used in a predictive capacity. Some of these variables include material models such as the kinetics and viscosity models, and the permeability and compaction models. Other variables include the material properties such as conductivity and heat capacity. Another set of variables include accurate specification of the boundary conditions including pressure and thermal cycles. The following chapters will show how the code was verified and list the constants used.

Chapter 6

Material Characterization

The computer program described in Chapter 5 cannot accurately model the RTM/RFI process without accurate inputs. This chapter discusses how the 3501-6 reduced catalyst resin and the carbon-fiber textile preforms were characterized.

6.1 3501-6 Reduced Catalyst Resin Model

The resin studied here is the Hercules 3501-6 resin system. It is a high performance epoxy based system widely used in the aerospace industry. In the current study, only half of the recommended amount of catalyst was added. This was done to increase its processing “window” where the viscosity of the resin is low enough to allow infiltration of the preform.

6.1.1 Cure Kinetics Sub-Model

Isothermal and dynamic differential scanning calorimetry (DSC) were used to measure the cure reaction kinetics of the reduced catalyst resin. Isothermal measurements were made

Table 6.1: 3501-6 reduced catalyst high temperature cure kinetics model constants.

	Value	Units
A_1	2.516×10^8	sec^{-1}
A_2	40.35097	sec^{-1}
A_3	8.7355×10^7	sec^{-1}
E_1/R	10.90214	Kelvin
E_2/R	5.28071	Kelvin
E_3/R	11.2061	Kelvin
n_1	0.8817	T in Kelvin
n_2	$(0.029598T) - 3.28439$	
m	0.96398	
C_1	0.05	
C_2	0.95	
H_R	430.0	kJ/kg
ρ	1260	kg/m^3

between 110 and 165°C. The complex curing reaction for this resin was resolved into two independent n th order reactions, and the data were fit to a two part mathematical model:

$$\frac{d\alpha}{dt} = C_1 k_1 (1 - \alpha)^{n_1} + C_2 (k_2 + k_3 \alpha^m) (1 - \alpha)^{n_2} \quad (6.1)$$

$$\rho \dot{H} = \frac{d\alpha}{dt} \rho H_R \quad (6.2)$$

where

$$k_i = A_i \exp \left[\frac{-E_i}{RT} \right] \quad (6.3)$$

The experimentally determined values for all the constants are listed in Table 6.1.

6.1.2 Viscosity Sub-Model

The viscosity-time characteristics of the reduced catalyst resin were measured at elevated temperatures using a Bohlin rheometer. Viscosity measurements were made using 25 mm

diameter parallel plates. An appropriate quantity of resin was used in order to maintain a plate gap of 1–2 mm. The cure reaction kinetics model was used to convert the isothermal viscosity-time curves to viscosity-conversion curves. For temperatures above 90°C the resin viscosity was found to fit the following equation from Chapter 3:

$$\mu(T, \alpha) = \mu_0(T) \left[\frac{1}{1 - \alpha} \right]^{A+B(T)\alpha} \quad (3.23)$$

where

$$\mu_0 = 7.875 \times 10^{-10} \exp \left[\frac{7765}{T} \right] \quad T \text{ in Kelvin}$$

$$A = 4.151$$

$$B = -17.831 + 0.147 T \quad T \text{ in } ^\circ\text{C}$$

where μ is the viscosity in Pa·s, and α is the degree of cure.

Since the heating rates used to heat the composite/tool assembly in the RFI process are slow, the resin flow and complete wet out often occurs before the autoclave reaches 90°C. These unique processing conditions required the development of a low temperature viscosity model. A Brookfield viscometer was used to perform isothermal viscosity measurements between 60 and 90°C. The cure of the resin was also measured by DSC at temperatures below 90°C, and it was found that the advancement of the resin was no more than 5–8% for times up to 8 hours. To fit the data, it was assumed that there is no significant cure below 90°C, and the viscosity in the low temperature region depends only on the temperature. The data were fit to an Arrhenius model:

$$\mu(T) = 4.0074 \times 10^{-16} \exp \left[\frac{12994.9}{T} \right] \quad (6.4)$$

where μ is the viscosity in Pa·s and T is the temperature in Kelvin.

6.2 Textile Preform Model

Two general types of textile preforms were characterized. The first is a multiaxial warp knit fabric that contains seven layers of unidirectional carbon fibers. The seven layers are knitted together with polyester thread. The knitted unit is referred to as a “stack”. The carbon fibers are arranged so that each stack has quasi-isotropic mechanical properties. Two different types of carbon fibers were used in this type of preform: AS4 and Tenax. Details about the warp knit fabric can be found in [25–27]. The second type of fabric is a triaxial braided carbon fiber preform. The tows are braided around a cylindrical mandrel to form a tube. The tubes were fabricated with AS4 6k carbon fiber bias yarns at a braid angle of 60° and with IM7 36k carbon fiber axial yarns. Approximately 44% of the fibers were in the axial direction and 56% of the fibers were in the off-axis directions. The tube is flattened to form an individual layer.

To form a preform, the stacks or tubes of material are cut to the desired dimensions and stacked together. The material is then stitched through the thickness using a modified lock stitch and Kevlar thread. The stitch rows on all material tested were 0.2 inches apart and the stitch step was 1/8 inch.

The computer model requires the permeability and the fiber volume fraction of these textile preforms as input. This section describes the methods used to find models that can predict the permeability and fiber volume fraction given the pressure applied to the preform. The types of preforms tested were 8 stack warp knit, and 4 and 14 tube braid.

6.2.1 Permeability

There are two common methods for measuring the permeability of fabrics and preforms. The two methods are steady-state and advancing front measurement. The materials used in this study were characterized using steady state measurements. Steady-state permeability is measured after the preform has been saturated, and is carried out under constant flow rate injection. The pressure differential across the preform is measured and the permeability is calculated from Darcy's Law. The permeability is measured as a function of fiber volume fraction. Both in-plane and through-the-thickness permeabilities were measured. Flow rate, mold height and pressure data were gathered using a National Instruments data acquisition system controlled by LabVIEW software. A complete description of the system can be found in Fingerson [28].

Figure 6.1 is a picture of the in-plane permeability fixture. Fingerson, Loos, and Dexter [28] contains detailed drawings of the permeability fixture. The mold cavity is 17.78 cm long by 15.32 cm wide. The preform is 15.2 cm long by 15.32 cm wide. The extra cavity length forms an inlet manifold allowing even inlet pressure across the face of the preform.

Figure 6.2 is a sketch of the through-the-thickness permeability fixture set up. The fixture is described in Weideman [29] and Hammond et al. [30]. The fixture test section was designed to characterize 5.1 cm long by 5.1 cm wide fabric preform samples. The upper and lower surfaces of the mold cavity compress the preform and contain holes to allow for fluid flow through the thickness of the preform.

For each fixture, specimens were cut out of the preform with a band saw so that the specimen fit tightly in the mold. The fixture was then closed and the mold height and compaction pressure were measured. Fluid was pumped through the preform using a Parker Zenith precision Gear Metering Pump. The entire pump system communicates with the PC

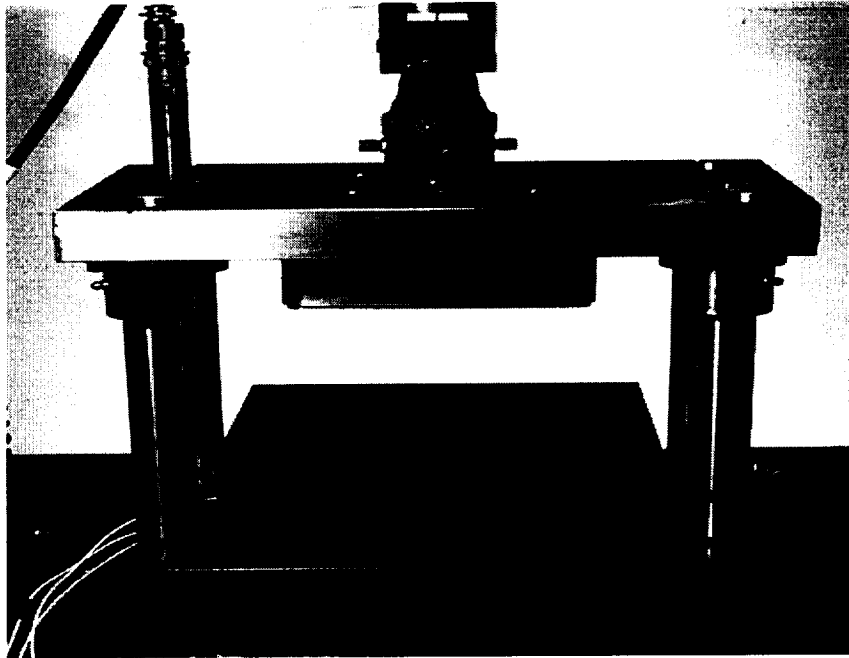


Figure 6.1: In-plane permeability measurement fixture.

running the LabVIEW data acquisition system. The flow rate was held constant until the inlet pressure reached steady state. The permeability and fiber volume fraction were then recorded directly from the LabVIEW software. The permeability was measured between 50 and 64 percent fiber volume fraction. The measured permeability constants can be found in Appendix B.

6.2.2 Compaction

Measuring the load required to reach a desired fiber volume fraction determined the compaction behavior of the preform. The in-plane permeability fixture with the O-ring removed was used to measure the compaction behavior. For compaction measurements the preform fit is not critical. Compaction pressure was applied at a 0.508 mm/min cross head rate until the first desired fiber volume fraction was reached. At that point, loading was stopped and

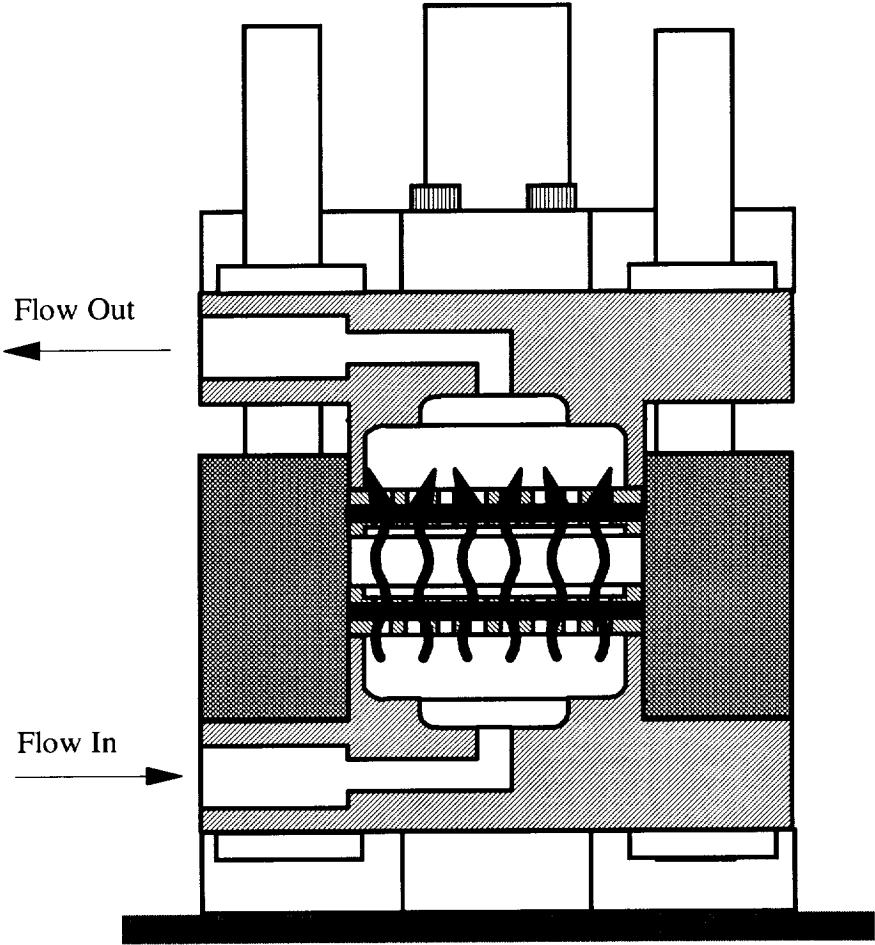


Figure 6.2: Through the thickness permeability measurement fixture.

the load level required to achieve equilibrium was recorded. Relaxation occurs in the pre-form as the fibers realign themselves under the applied load. Again compaction loads were recorded between 50–64% fiber volume fraction. The same data acquisition system used for the permeability test was in the compaction experiments. The measured compaction constants can be found in Appendix B.

Chapter 7

Mesh Refinement Study

There are many variables that can affect the accuracy of a finite element model. One class of variables is the user inputs to the model. Inaccurate material properties or inaccurate boundary condition application can result in meaningless results. Another user input that is important to the accuracy is the discretization of the physical problem. In many models, the solution may have high spatial gradients in some areas. The discretization must be fine enough to adequately capture these gradients. Different solutions exist to capture these gradients. One method is to increase the order of the element used. Instead of using a linear element, a quadratic, a cubic, or higher order element can be used. The other method is to decrease the size of the elements in the area. As the element order increases or the size of the elements decrease, the finite element solution will converge to the “true” solution of the problem [21].

The purpose of this study was to find the minimum recommended element sizes that result in a converged model for a typical RFI part. The results reported here are intended as a starting point when checking convergence of any model and are not intended as hard and fast rules. It must be stressed that failure to check each finite element model for convergence can result in inaccurate and flawed results.

7.1 Flow and Thermal Model Considerations

3DINFIL is composed of a flow model and a thermal model. Each model requires separate considerations when checking for convergence. This section will discuss issues that may arise in each model.

The flow model has two main variables that are of interest. The first is the fluid pressure, and the second is the flow front location. The fluid pressure accuracy is determined by the mesh resolution in the direction of the pressure gradients. Pressure gradients will typically be highest around sharp geometry transitions such as injection ports (in the case of RTM) or the blade/flange transition region. The resolution of the flow front location will be determined by the distance from one node to the next. Since the control volume method does not locate the flow front exactly, the uncertainty in the flow front locations is the length of the element.

In the thermal model, there is only one variable, the temperature. One area where high temperature gradients can form is where materials of different thermal conductivities are in contact with each other. Another area that will have high gradients will be the boundary of the model where the convective boundary conditions are applied.

7.2 Model Description

A two stiffener panel was chosen to be modeled in this study because it is typical of the stiffened wing skin parts to be modeled. The geometry is representative of a full scale RFI part, and the same materials are used in both the model and an actual part. Also, the two stringer panel incorporates the latest hogged-out tooling concept. A sketch of the model is shown in Figure 7.1.

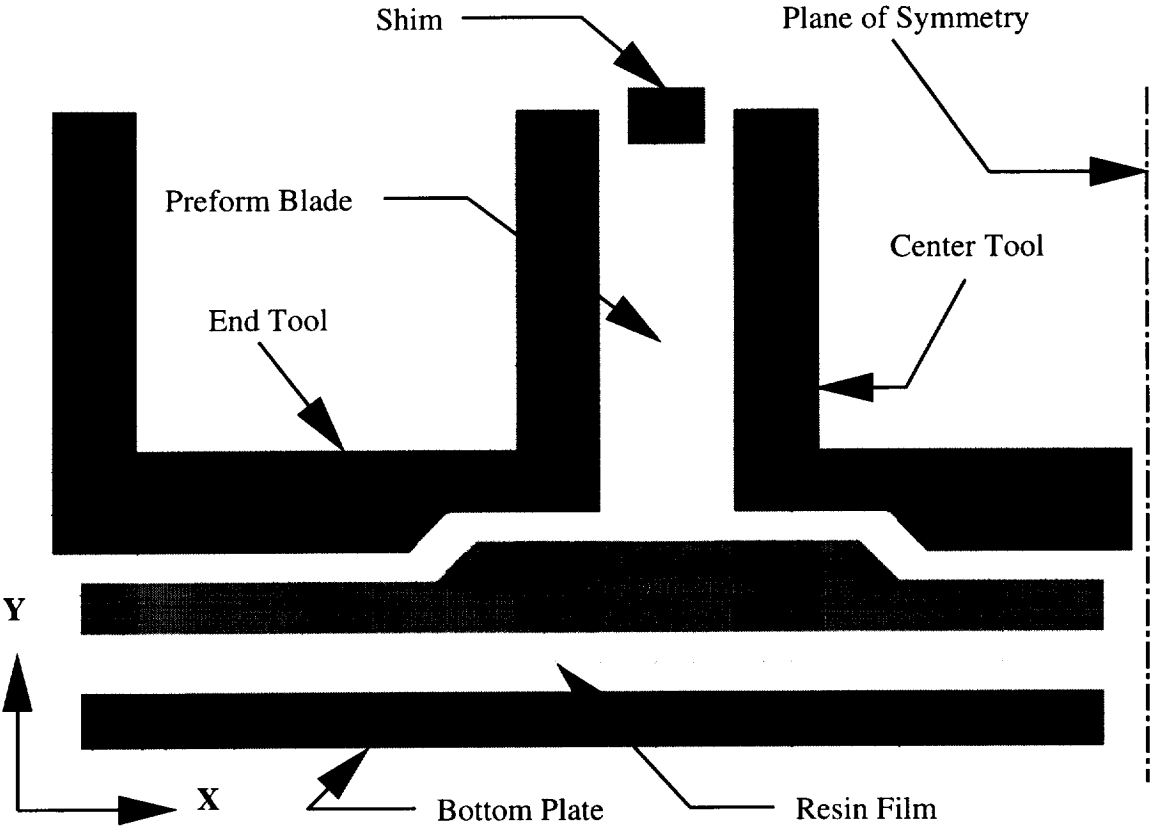


Figure 7.1: Mesh refinement model.

The finite element model used in the study was one element thick in the Z direction. This was chosen for two reasons. First the one element thick model will simulate a two-dimensional slice of the part. Since the two stringer panel was long compared to the thickness of the skin, this seems to be a valid assumption. Also, many parts can be initially modeled as two-dimensional. The second reason is that the mesh refinement is easier in the two-dimensional model than in a full three-dimensional model. In a model of a slice of the part, the temperature fields are easier to visualize. The run times are also much faster than a full three-dimensional model.

The results that are found for the one element thick model should be useful as a starting point for three-dimensional mesh refinement study.

7.2.1 Geometry

Approximate dimensions of the preform are shown in Figure 7.2. The dimensions of the tooling components can be found in Appendix A, Section A.2.

7.2.2 Boundary Conditions

The boundary condition on the flow model was the autoclave pressure. A pressure of 791 kPa (114.7 psi) was applied to the bottom surface of preform where the resin film is located.

The boundary conditions on the thermal model consisted of convective boundary conditions. The autoclave temperature is shown in Figure 7.3. Convective coefficients of $50 \text{ W}/(\text{m}^2 \cdot ^\circ\text{C})$ were applied to the outer surfaces of the model. No convection coefficients were applied to the front or back surfaces of the model, or to the plane of symmetry. These surfaces were taken to be thermally insulated.

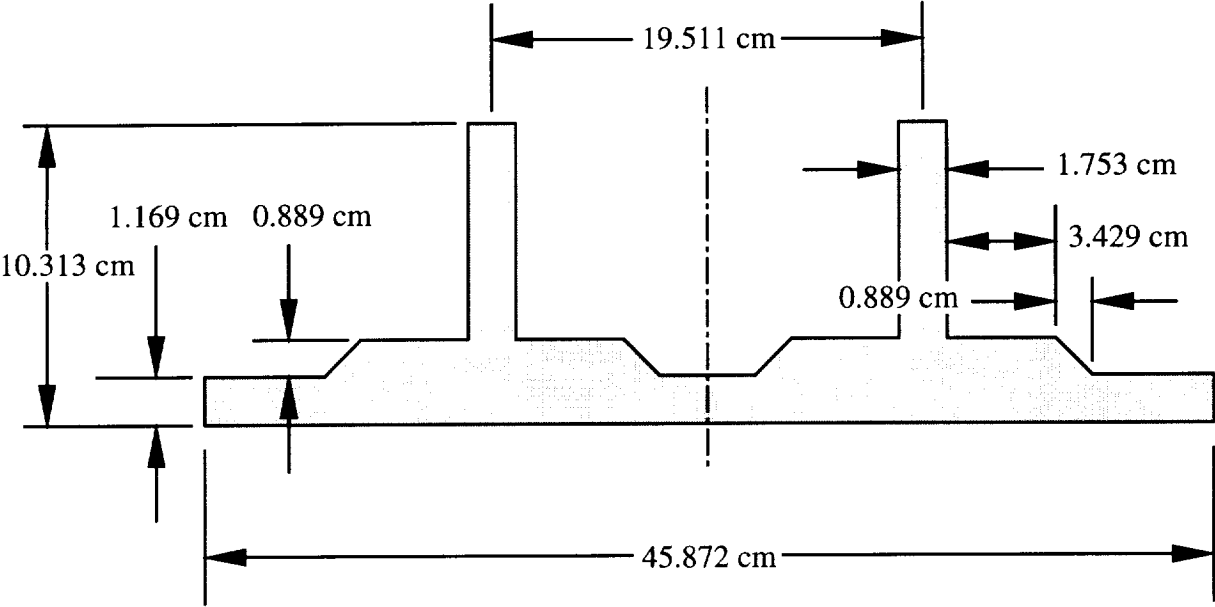


Figure 7.2: Dimensions of the two stiffener preform.

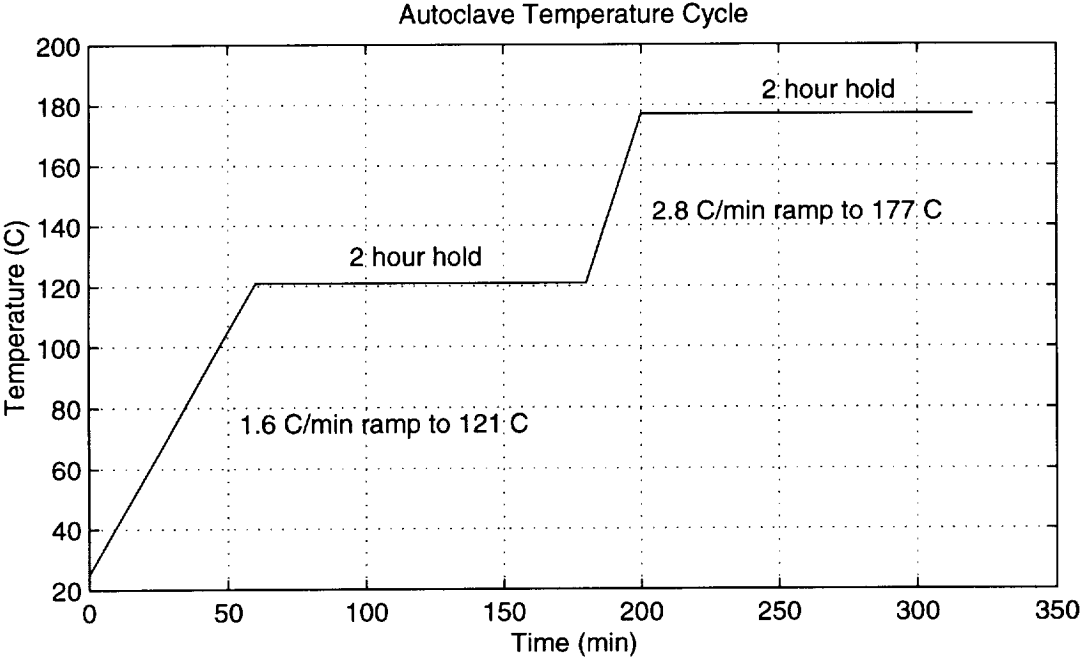


Figure 7.3: Autoclave temperature cycle.

Table 7.1: Permeabilities applied to the mesh refinement model.

Material	Permeability m^2
Skin: Warp Knit 57% FVF	
IPP (S_{zz})	1.031×10^{-11}
IPN (S_{xx})	1.047×10^{-12}
TTT (S_{yy})	3.665×10^{-12}
Blade: 14 Tube Braid 57% FVF	
IPP (S_{zz})	1.348×10^{-11}
IPN (S_{yy})	6.914×10^{-12}
TTT (S_{xx})	$7.417 \times 10^{-13*}$

* No 14 tube data available, computed using 4 tube braid TTT fit.

7.2.3 Materials

There were two flow materials used in the model, one for the blade and one for the skin and skin/flange regions. The preform fiber volume fraction was chosen to be 57%, and the permeabilities were calculated using the constants in Appendix B. The constants are given for permeabilities as in-plane, parallel to the stitching, (IPP); in-plane, normal to the stitching (IPN); and through-the-thickness (TTT). The materials were applied to the model as shown in Figure 7.1, and the permeability values are shown in Table 7.1

The thermal materials used were 6061-T6 aluminum and the carbon fiber preform. The material constants are listed in Appendix B. The aluminum is isotropic, so no orientation is necessary. The preform is thermally orthotropic, so the orientation of the conductivity tensor is necessary. For the skin, the in-plane value was used for k_{xx} and k_{zz} and the TTT value was used for k_{yy} . The blade used the in-plane value for k_{yy} and k_{zz} and the TTT value for k_{xx} .

Table 7.2: Size and run time of the models.

Case	Flow Model		Thermal Model		CPU Time (min)
	Nodes	Elements	Nodes	Elements	
A	708	302	1324	601	2.7
B	604	252	1168	521	2.2
C	1008	434	2122	970	4.6
D	1814	792	4270	1998	12.4
E	6166	2856	15902	7680	126.6

7.3 Procedure

In this study, a very fine mesh was used to find the “true” solution. The other, coarser, meshes were compared against this. In the real world this option is usually not available due to time and size limitations. The general procedure for finding a converged mesh is as follows:

1. Run the first coarse mesh.
2. Refine the mesh.
3. Compare the results from the refined mesh with the old mesh, and determine error between the two.
4. If the error is too high, repeat steps 2 and 3 until the error is acceptable.

7.3.1 Description of the Finite Element Meshes

The five meshes used are shown in Figures 7.4–7.8. The number of nodes and elements in each model is listed in Table 7.2.

Case A was based on a McDonnell Douglas Aircraft (MDA) mesh refinement study done to find the necessary mesh density for a converged flow model. Thermal convergence was not checked in the MDA study.

Case B was constructed to determine a lower limit on the number of elements that are necessary through the thickness of the stiffener. It was also constructed to have better element aspect ratios than Case A.

Case C refined Case A in the in-plane direction of the preform skin.

Case D refined Case C by a factor of 2 in all directions.

Case E refined Case D by a factor of 2 in all directions. Because of the mesh density used, this case was used as the 'true' solution of this finite element model. It will be shown that this is a valid assumption.

7.4 Thermal Error Calculations

All error estimates were calculated against the total temperature variation of the applied temperature cycle. The variation was $177^{\circ}\text{C} - 25^{\circ}\text{C} = 152^{\circ}\text{C}$, and Equation (7.1) was used to calculate the error.

$$100\% \times \frac{(\text{temp}) - (\text{temp in case E})}{177 - 25} \quad (7.1)$$

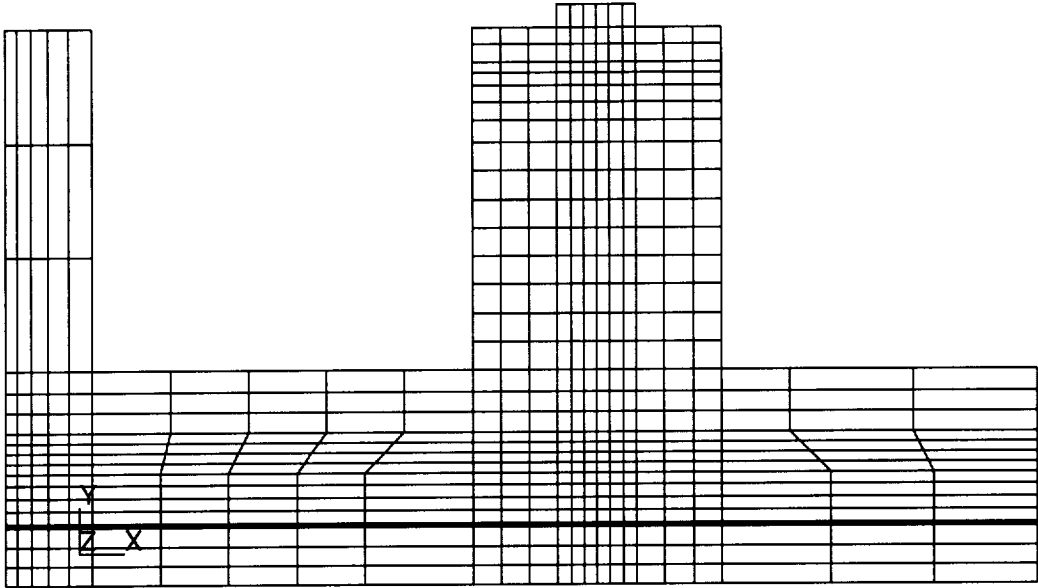


Figure 7.4: Mesh for mesh refinement case A.

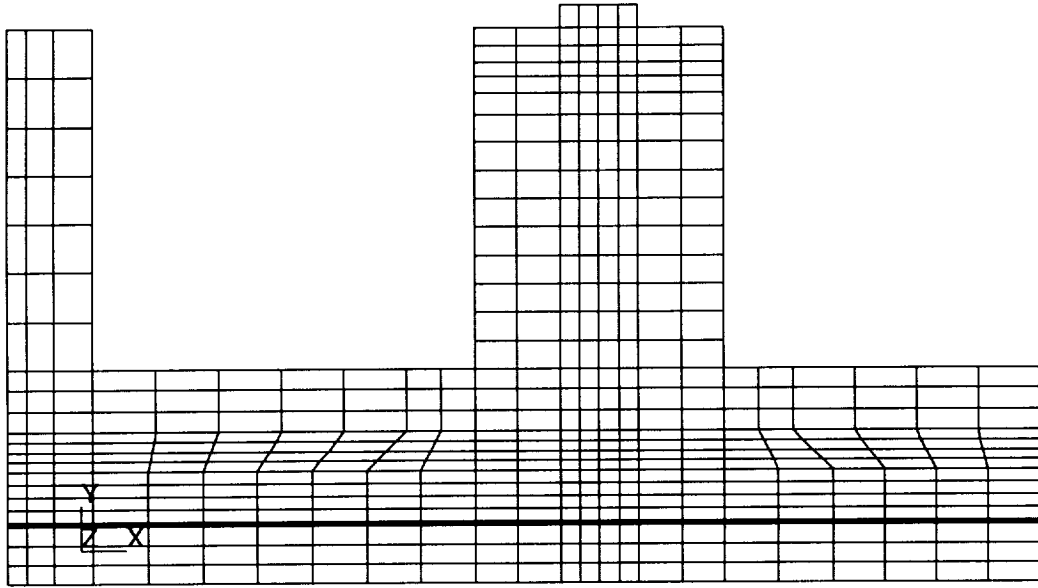


Figure 7.5: Mesh for mesh refinement case B.

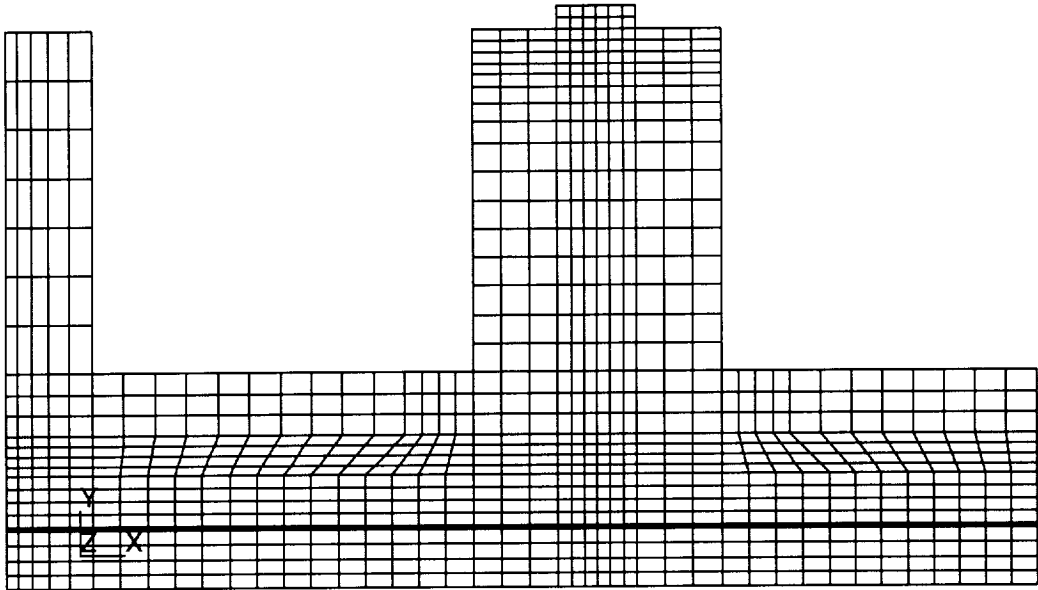


Figure 7.6: Mesh for mesh refinement case C.

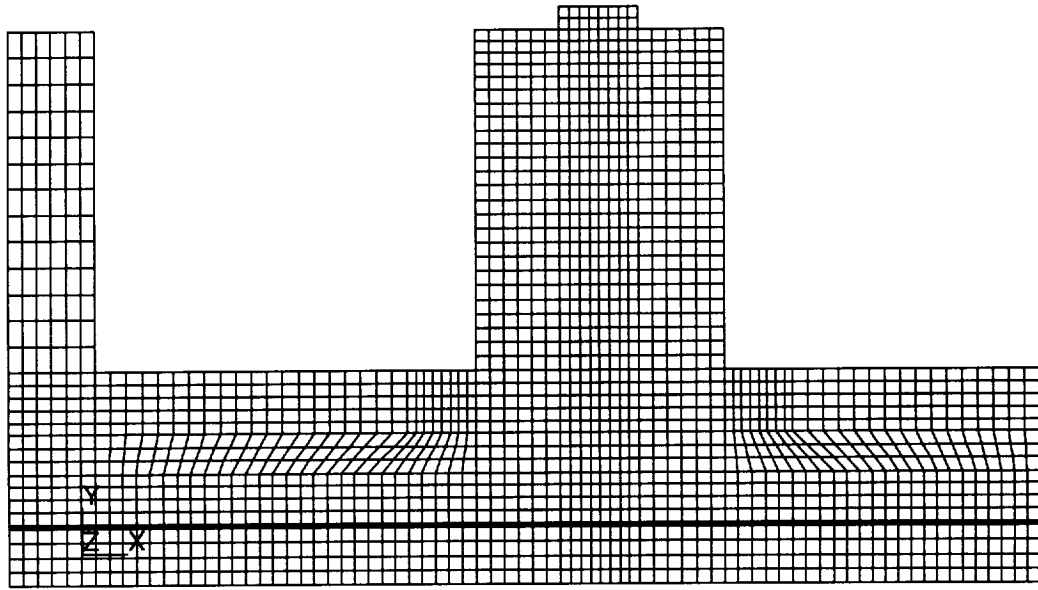


Figure 7.7: Mesh for mesh refinement case D.

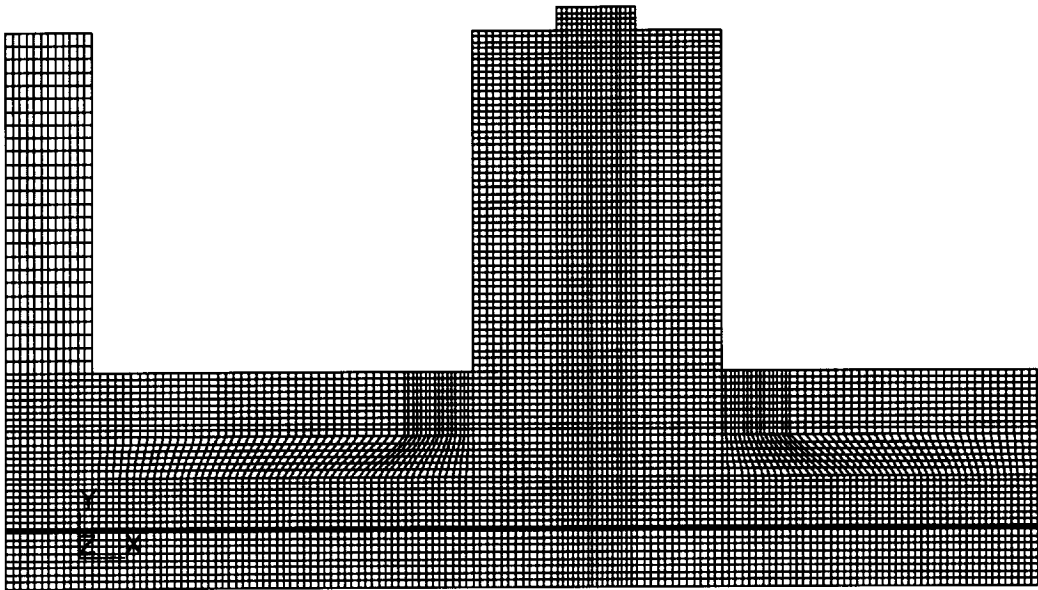


Figure 7.8: Mesh for mesh refinement case E.

7.5 Results

7.5.1 Flow Model Convergence

The variable used to determine convergence of the flow model was the total fill time of the model. The fill times for the six different meshes varied by less than 1%. Case E filled in 71 minutes and 39 seconds. This indicates that all of the meshes have converged for the flow model. Since the thermal model was run concurrently with the flow model, the temperatures must be looked at when determining the convergence of the flow model. It will be shown in the next section that the temperatures of the six meshes only differed by 2% when the model filled. This was because the resin had not begun to generate heat from curing yet. For times up to 71 minutes, the thermal model could be considered converged, so the thermal model had no effect on the convergence of the flow model. The conclusion of this is that the flow mesh used in either Case A or Case B was sufficient for convergence of the flow model.

7.5.2 Thermal Model Convergence

The flow model is easily checked for convergence by examining the fill time of the model. When checking for convergence in the thermal model, decisions must be made as to where to check for thermal convergence. One option is to check for convergence at the interface between the tool and preform. Another option is to check for thermal convergence in the interior of the preform itself. In an experimental situation the interface region can be easily instrumented when the preform and tooling are assembled. Instrumenting the interior of the preform is more difficult, since the thermocouples must be stitched into the preform itself. Because the finite element model calculates temperatures at all the node points both

on the surface and in the interior of the components, there is no restriction on which points can be checked. It will be seen that the most important points to check are the points in the interior of the preform. Due to the low thermal conductivity of the preform and the heat generated by the curing resin, the preform will experience the highest thermal gradients, and the center of the preform will experience the highest temperatures in the model.

The time history of the temperature was plotted for all six cases at six different points in the finite element model. The points are shown in Figure 7.9. Points 1–3 were at the interface between the preform and the tooling, and points 4–6 were at various locations in the interior of the preform. The temperatures and the error (as compared to case E) are shown in Figures 7.10–7.15.

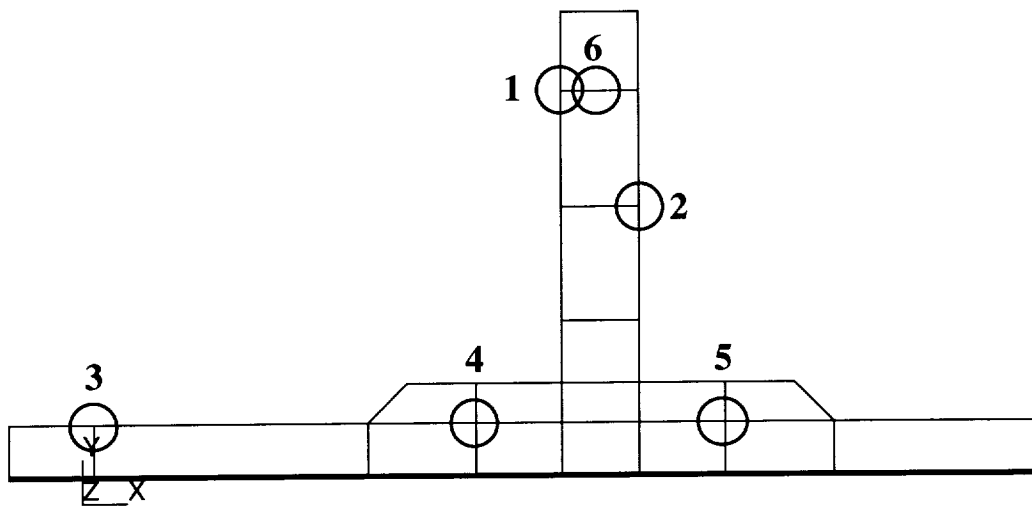


Figure 7.9: Temperature measurement points in the mesh refinement model.

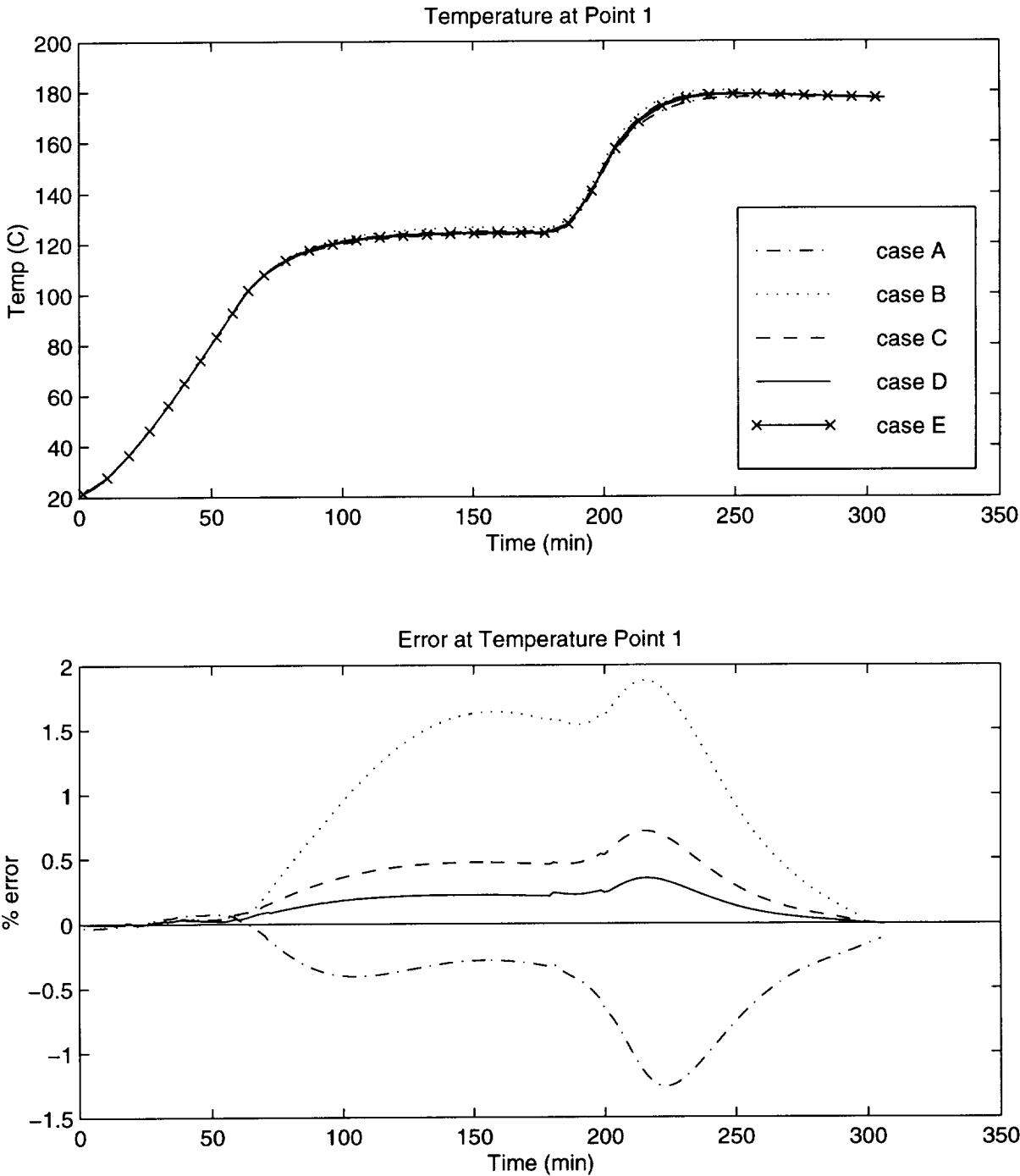


Figure 7.10: Thermal comparison between the different meshes at point 1. Temperature measurement points are shown in Figure 7.9.

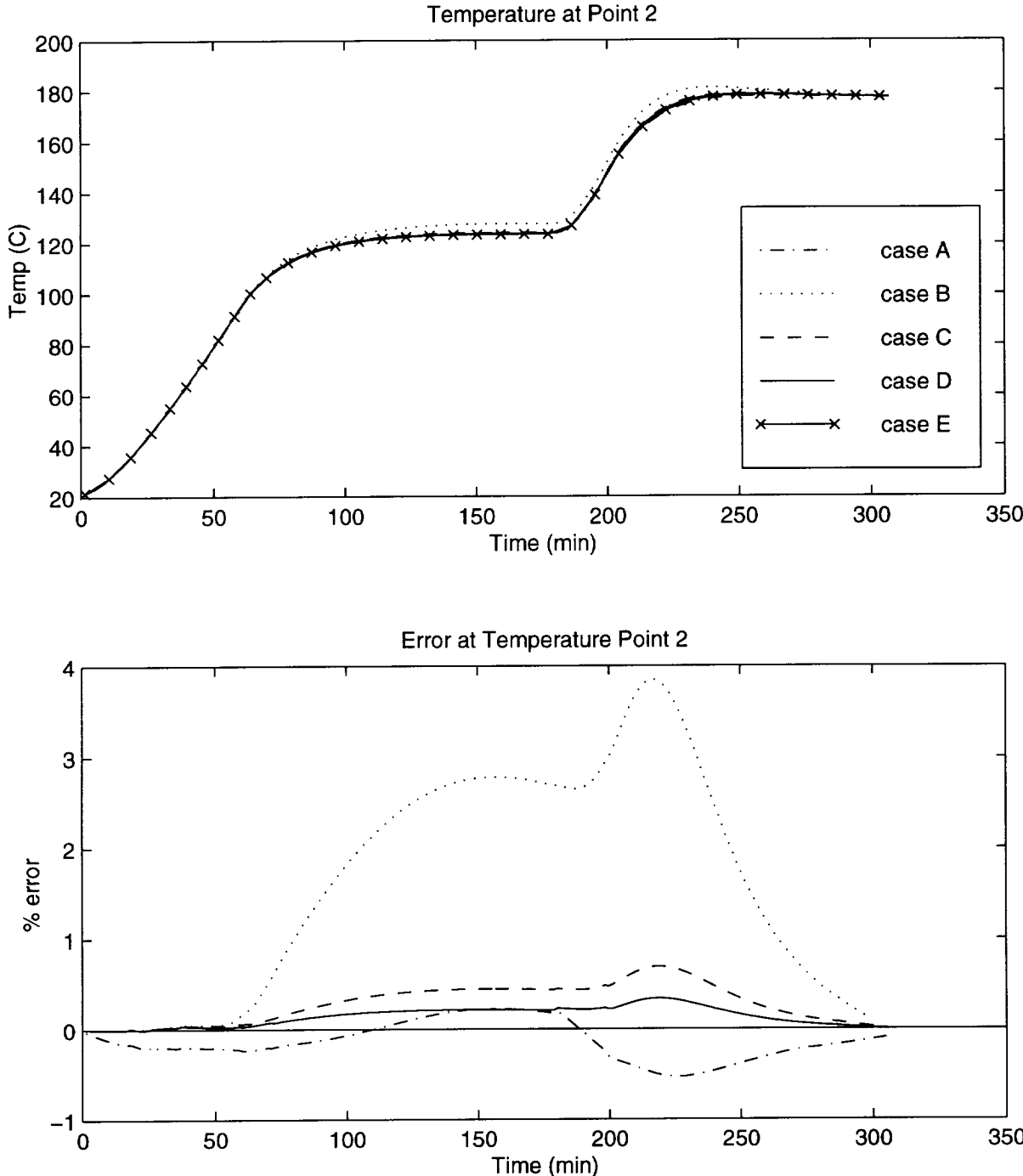


Figure 7.11: Thermal comparison between the different meshes at point 2. Temperature measurement points are shown in Figure 7.9.

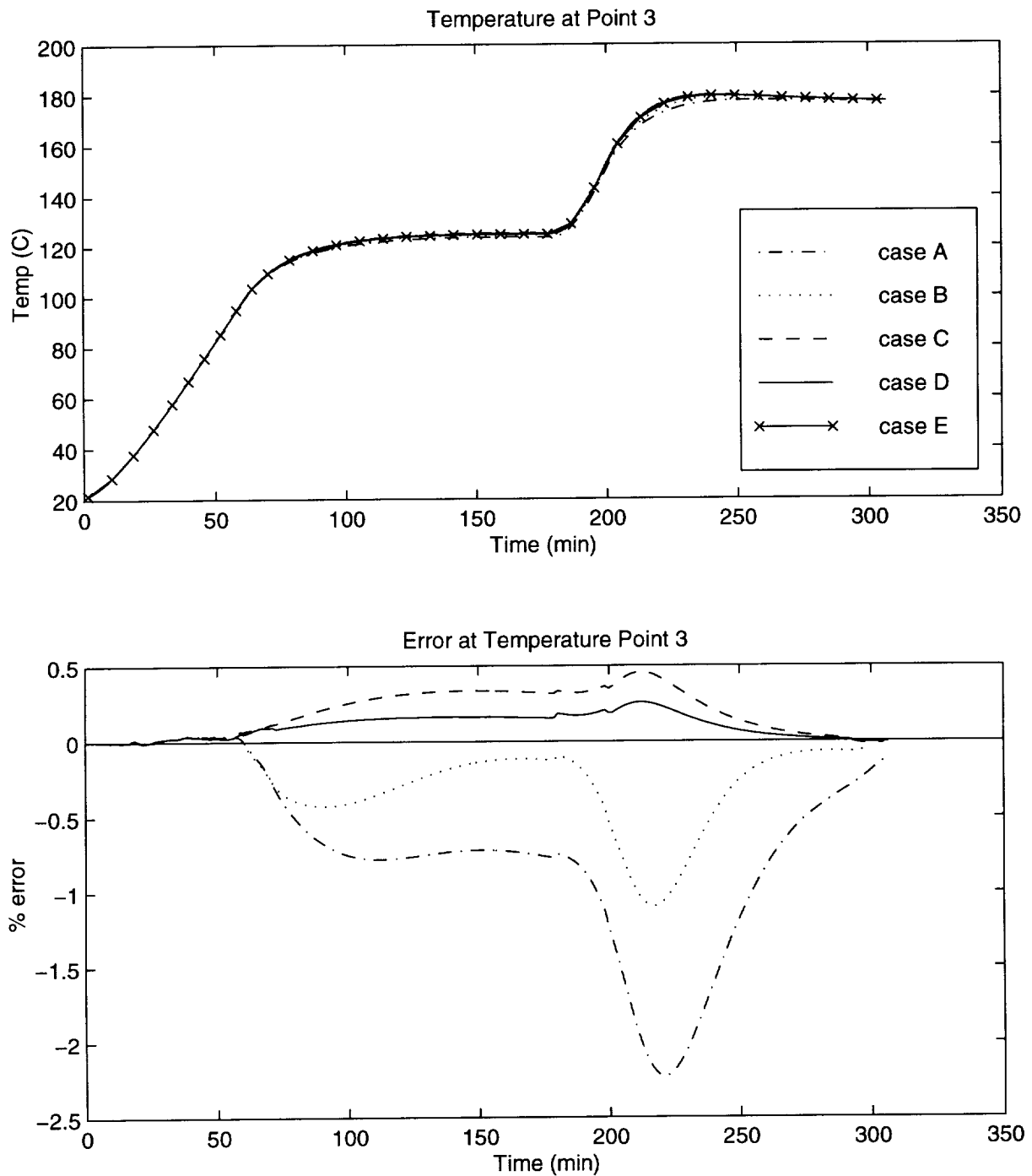


Figure 7.12: Thermal comparison between the different meshes at point 3. Temperature measurement points are shown in Figure 7.9.

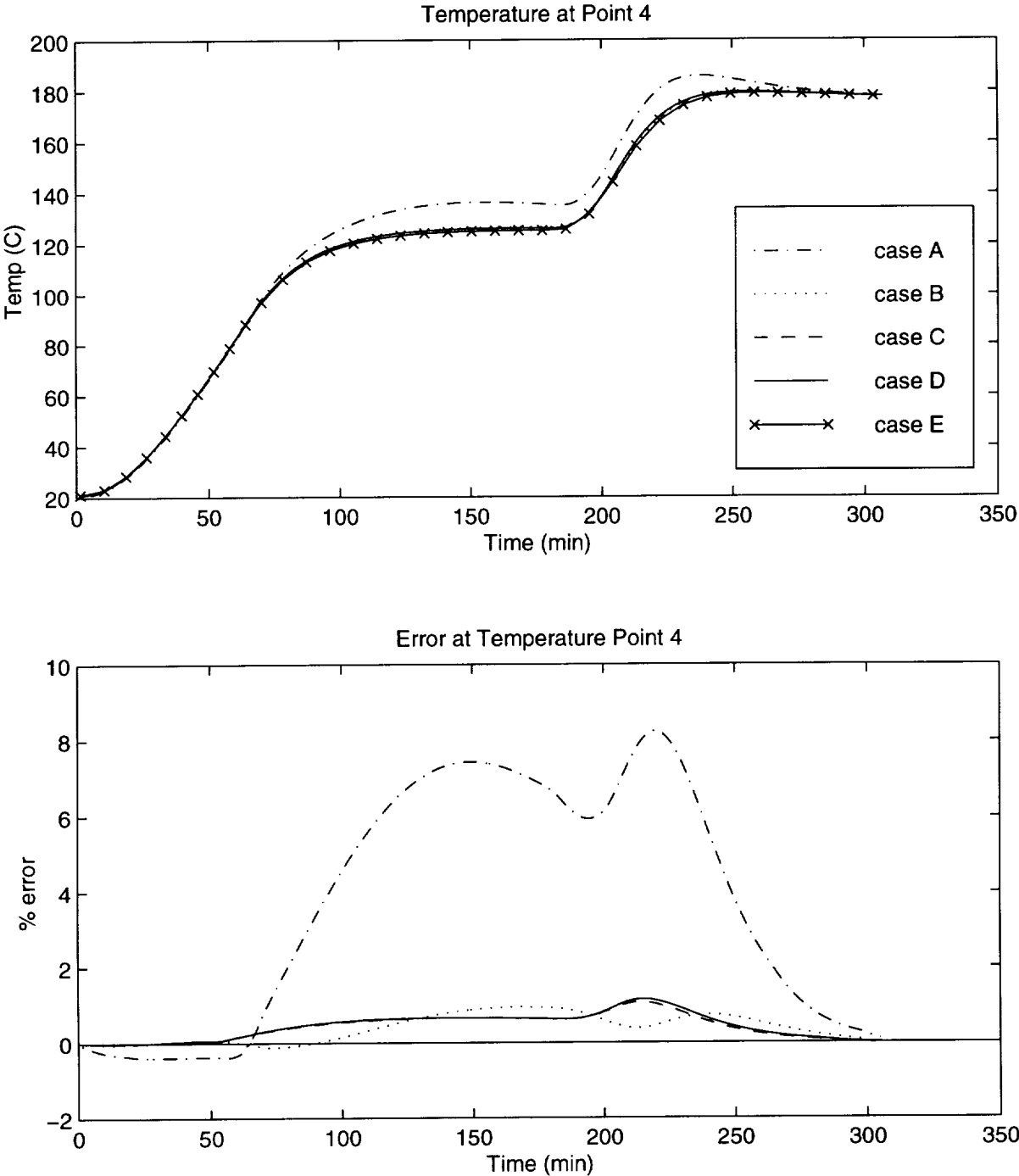


Figure 7.13: Thermal comparison between the different meshes at point 4. Temperature measurement points are shown in Figure 7.9.

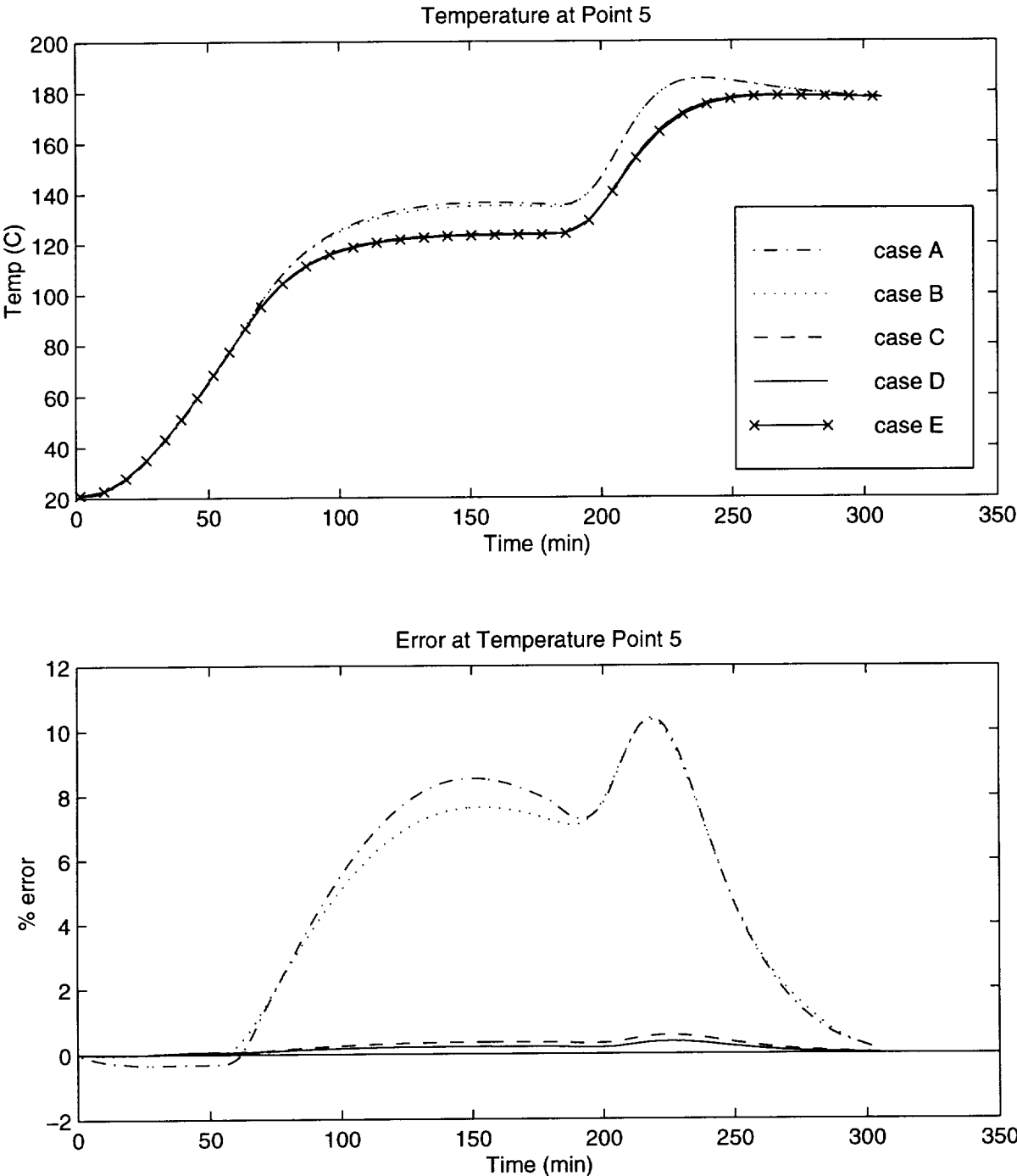


Figure 7.14: Thermal comparison between the different meshes at point 5. Temperature measurement points are shown in Figure 7.9.

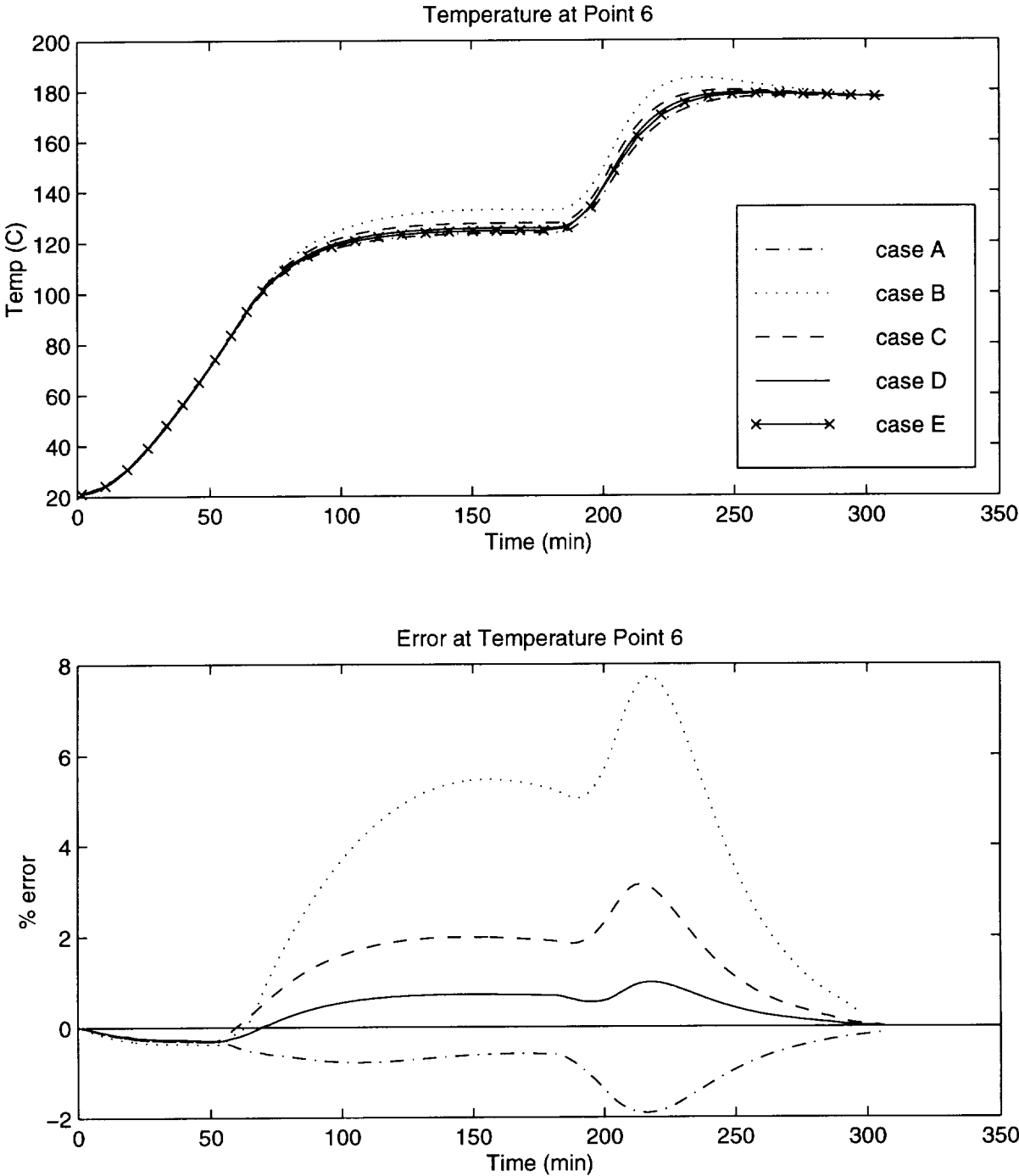


Figure 7.15: Thermal comparison between the different meshes at point 6. Temperature measurement points are shown in Figure 7.9.

7.6 Discussion

All six temperature plots have less than 0.5% error before 51 minutes. After 51 minutes, the solutions begin to diverge. At about 51 minutes, portions of the preform begin to reach temperatures of greater than 90°C and the resin begins to generate heat as it cures (see Chapter 6 for a description of the resin model). This heat generation is non-linear in nature, so a finer mesh must be used to capture the thermal gradients. Looking at Cases A and B shows that a thermal overshoot is a general trait of an unconverged model.

The results of the temperature points will now be discussed.

Points 1–3 were located at the interface between the tool and the preform. The maximum error in these points was 2%, 4%, and –2.5% respectively. This corresponds to a temperature deviation of –3–6.3°C. These points are not a good place to try to measure the convergence since they seem to be relatively insensitive to the mesh used. This is due to their contact with the aluminum tooling. The high conductivity of the aluminum keeps the temperature of the tools close to that of the autoclave.

Points 4–6 proved to be better suited to checking convergence of the model. These points deviated from the ‘true’ solution of Case E by up to 8%, 10%, and 8%, respectively. That translates to an error of 12–16°C. These points appear to be more sensitive to the choice of mesh than the points at the perform/tool interface.

Points 4 and 5 were located inside the preform, between the flange and the skin. In cases A and B, a significant temperature overshoot of 8–10% was seen. In case C, the error was less than 1%. Comparing the meshes in cases A, B, and C seems to indicate that the in-plane mesh size needs to be close to that found in case C.

Point 6 shows an 8% temperature overshoot in the coarse mesh of case B. The temperatures

in Cases A and C only show an error of 2%. This indicates that the mesh in the blade in case B is too coarse. Comparing case B to cases A and C indicates that there must be about six elements through the thickness of the blade and at least three elements through the tool.

Case D was run to guarantee that case C was converged for the temperatures. While there was the 'true' solution of case E to compare to for this study, in the real world one is usually not able to create a mesh that fine. Points 5 and 6 showed significant change between cases B and C, and there would be no way to tell if case C was converged without running a finer mesh similar to case D.

7.7 Conclusions

The findings above show that the flow and thermal models require different mesh sizes to converge. If the flow model fills before any significant heat has been generated by the curing resin, a mesh similar to case A should be sufficient for the flow model to converge. If the preform fills after the resin begins to cure, the model must be thermally converged to ensure that the fill times are correct. Case C had converged adequately. Tables 7.3 and 7.4 list the approximate element sizes used to create cases A and C.

Note that these sizes are only intended as a starting point for checking thermal convergence of a 3DINFIL model, as these sizes only apply to this model using the parameters listed above. A list of some of the variables that could affect the minimum necessary element sizes are model geometry, material properties, convective coefficients, and the temperature and pressure cycles.

Table 7.3: Mesh parameters for case A.

Material	Direction	Elem. Length	No. of Elem.
Preform Skin	in-plane	25 mm	10
	TTT	2-3 mm	4
Preform Flange	in-plane	25 mm	(set by tooling)
	TTT	2-3 mm	4
Preform Blade	in-plane	2 mm	16
	TTT	3 mm	6
Aluminum tooling	in-plane	25 mm	(set by preform)
	TTT	10 mm	2-4
	Other areas	10 mm	

Table 7.4: Mesh parameters for case C.

Material	Direction	Elem. Length	No. of Elem.
Preform Skin	in-plane	6 mm	38
	TTT	3 mm	4
Preform Flange	in-plane	6 mm	20
	TTT	2-3 mm	4
Preform Blade	in-plane	2 mm	16
	TTT	3 mm	6
Aluminum tooling	in-plane	6 mm	(set by preform)
	TTT	6 mm	3-6
	Other areas	10 mm	

7.8 Future Work

A full three-dimensional verification of these recommended element sizes should be conducted. The results presented here should be used as a starting point in that study. Another area that should be explored is where in the model the mesh refinement would do the most good. This study used a uniform mesh in each direction. Refining the model near the surface of the tools where the convective boundary condition is applied, or refining the mesh near the tool/preform interface may provide better results than the uniform meshing scheme currently used.

Chapter 8

Flow Model Verification

One of the most critical aspects of an RTM/RFI simulation program is accurate prediction of the flow through the preform. Before a simulation program can be used, it must be verified against experimental data. There are some questions that arise when verifying the program. First, how accurate are the inputs to the model? Since preform permeabilities are measured in a single direction at a time, how accurate is it to use these one-dimensional permeabilities in three-dimensional tensor form as an input to the model? Second, given accurate inputs, can the code adequately predict the three-dimensional flow pattern? To answer these questions, a model was constructed to simulate the flow in a “T-stiffened” section and the simulation results were compared against experimental results. This chapter will discuss the three-dimensional flow experiment and the finite element simulation model, and will compare the results obtained.

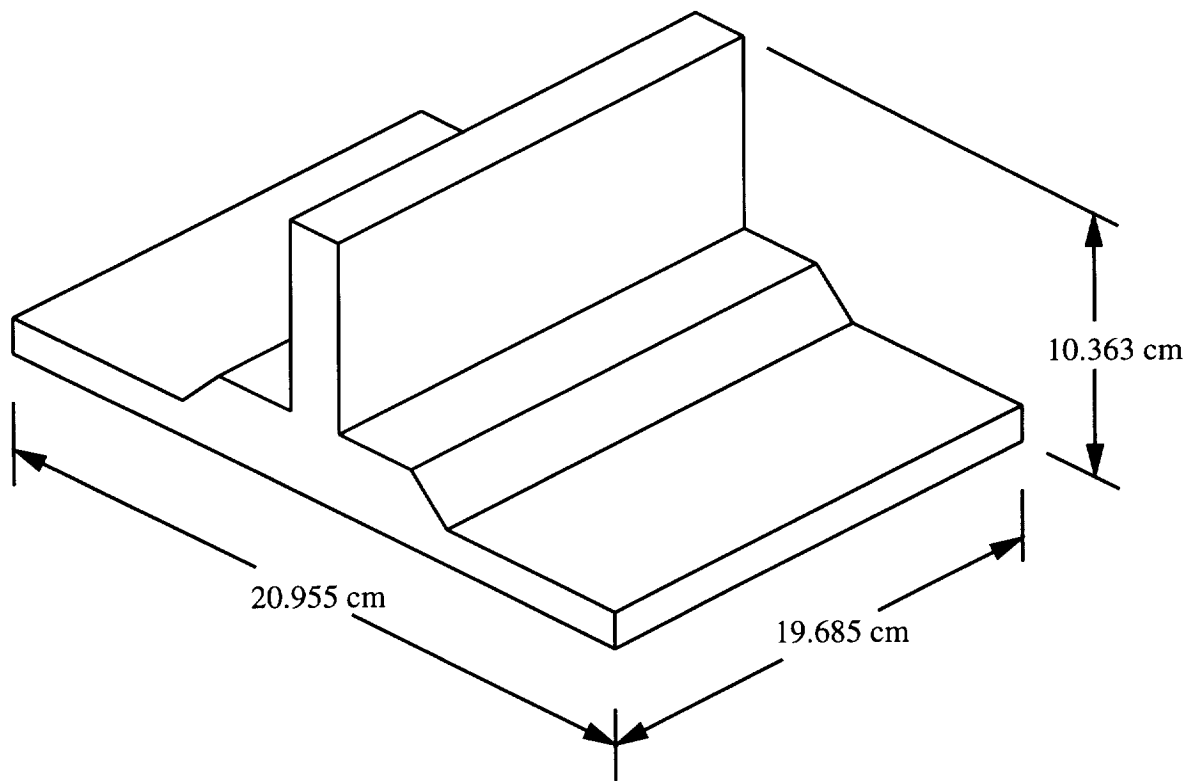


Figure 8.1: Flow verification preform dimensions.

8.1 Experiment

The preform used in this study was a section of T-stiffened skin. The blade was constructed of 14 tube braided material and the skin was made from eight stacks of the warp knit material. These materials are described in Chapter 6. The approximate dimensions of the preform used are shown in Figures 8.1 and 8.2.

A mold was constructed to facilitate the infiltration of the T-stiffened preform. The steel mold was designed with the following objectives:

- Achieve a three-dimensional flow pattern in the preform.

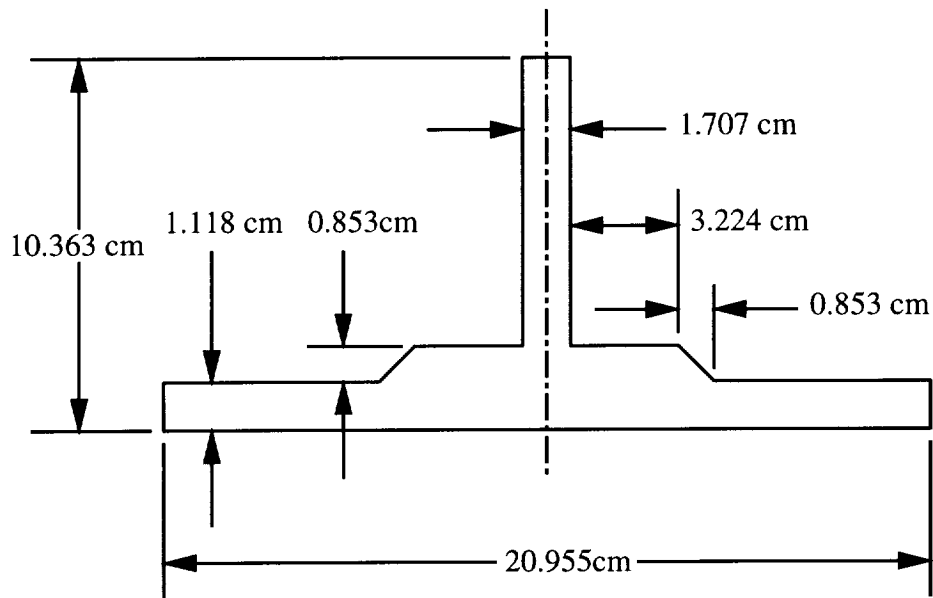


Figure 8.2: Flow verification preform dimensions.

- Compact the preform to 57% carbon fiber volume fraction.
- Provide a seal along the edges of the preform.
- Create boundary conditions that are easily modeled in the simulation code.
- Dimensionally stable during resin injection under elevated pressure.

The mold consists of four pieces, each constructed from steel. They are a base plate, a picture frame, and left and right mold plates. The interior dimensions of the mold are fixed to provide the correct compaction of the preform.

The mold has a single injection port located in the center of the base plate. The sides of the mold are closed and the top of the stiffener is open to the atmosphere. Mounted in the mold are 12 Entran EPX series pressure transducers. The locations of the transducers in the mold are shown in Figure 8.3. The transducers were used to measure the passage

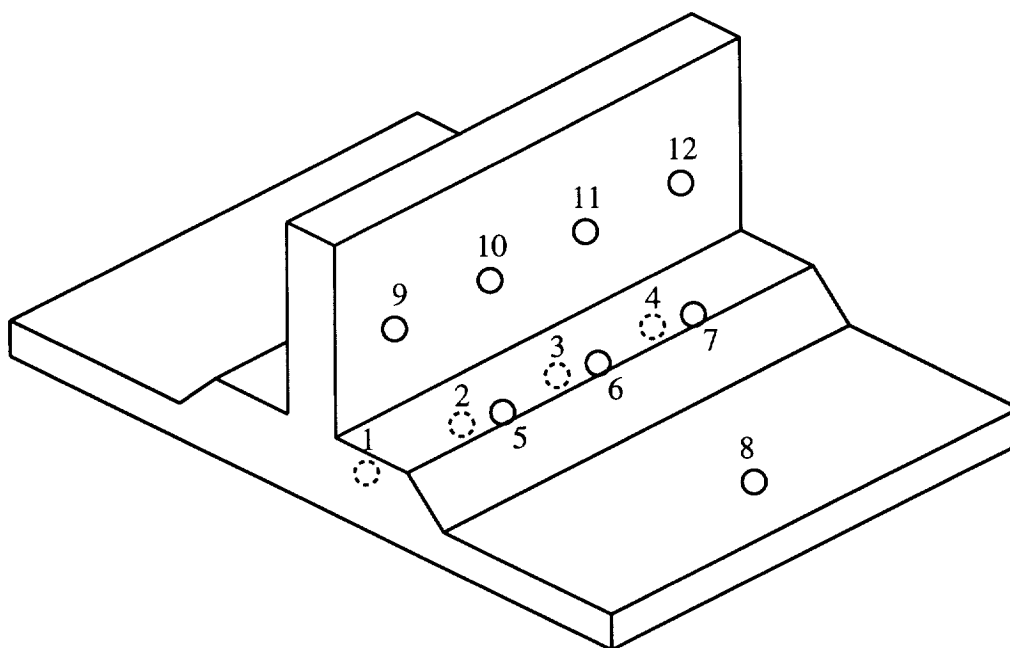


Figure 8.3: Pressure transducer locations.

of the flow front, and to measure the fluid pressure inside the mold. The diameter of the transducer is 3.5mm. The tip of the transducer was set back into the face of the mold so it would not interfere with the flow front. Transducers 1–4 are located in the base plate, along the center line. Transducers 5–7 are located on the top of the flange. Number 8 is located on the skin, and 9–12 are located on the blade.

The pressure data from the transducers were recorded using LabVIEW software running on a PC [28].

A Parker Hannifin Corp. Zenith constant flow rate pump was used to infiltrate the preform. A flow rate of 3 cc/min was used. The fluid used was corn oil and the viscosity of the oil was measured to be 0.054–0.057 Pa·s.

The mold was designed with the intent that it would provide an adequate seal around the edges of the preform; but an initial run showed that the oil tended to leak around the edges.

All subsequent runs had the edges of the preform coated with vacuum grease to prevent leakage.

8.2 Simulation Model

A three-dimensional finite element model of the preform was constructed. Three different models were run using the isothermal, constant viscosity, flow-only option of 3DINFIL. All three models used the same finite element mesh, but different numerical values for the permeabilities and fiber volume fractions were input into each model.

8.2.1 Geometry and Boundary Conditions

The preform has two lines of symmetry, so only one-quarter of the preform was modeled. A picture of the finite element mesh is shown in Figure 8.4. A total of 3496 elements and 4569 nodes were used to construct the model. The diameter of the inlet port was 1.111 cm. Since the model was constructed with hexahedral elements, the inlet port was modeled as a square having the same area as the circular inlet port.

There were two boundary conditions applied to the finite element model. The first is the constant flow rate condition. To simulate the experimental flow rate of 3 cc/min a constant flow rate of 0.75 cc/min was applied to the model. This flow rate is only one-fourth of the experimental value because of the symmetry in the model. The second boundary condition was the pressure sinks. These pressure sinks simulate the areas of the mold that were left open to the atmosphere. Sinks were applied to the top of the blade and the outside corner of the skin.

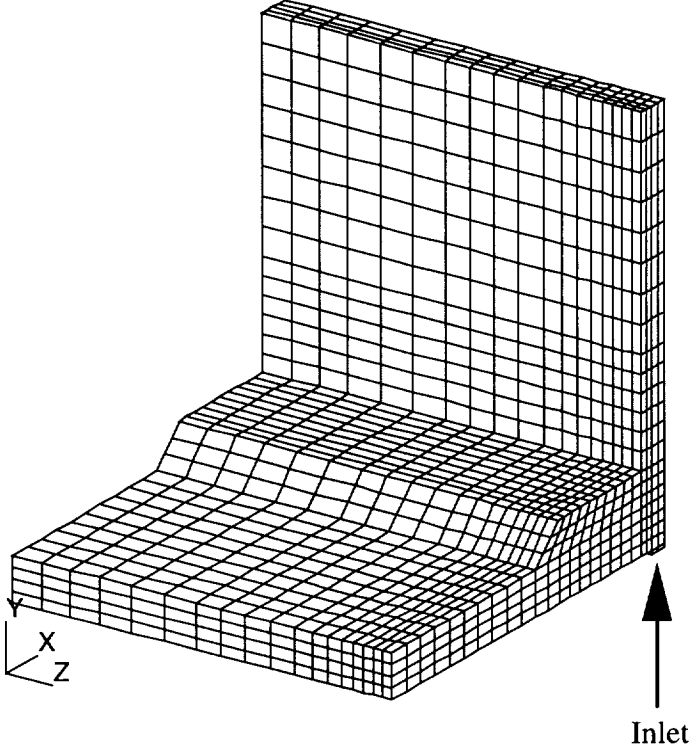


Figure 8.4: Quarter symmetry finite element mesh.

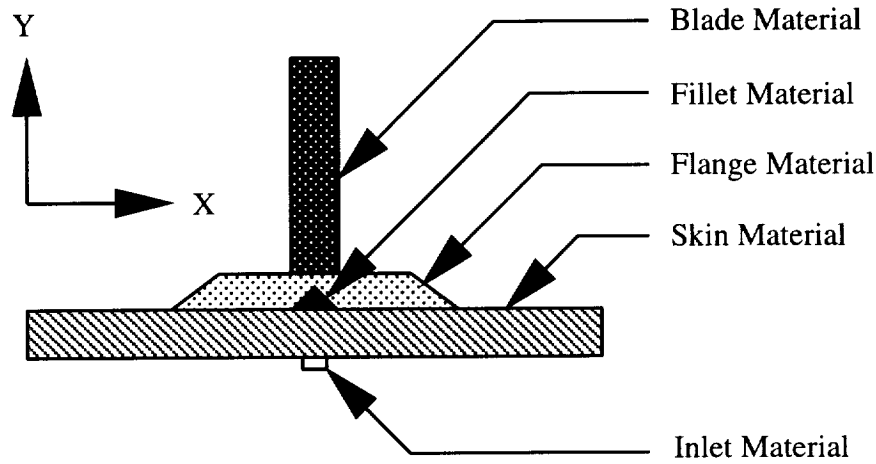


Figure 8.5: Flow materials in the flow verification model.

Other inputs to the model include the viscosity of the oil and the permeability of the preform. The viscosity used in the modeling was 0.055 Pa·s.

8.2.2 Permeability Calculation

The preform was divided into five regions and permeabilities were applied to each as shown in Figure 8.5.

The fiber volume fractions for the skin and blade were calculated as follows. First, the volume fractions were determined by using the areal weight of the preform A_w , the thickness of the closed mold t , and the density of carbon fiber ρ_f :

$$v_f = \frac{A_w}{t\rho_f} \quad (8.1)$$

The parameters and the computed values of the fiber volume fractions are shown in Table 8.1. Once the fiber volume fractions are known the permeabilities were computed using the fit constants in Appendix B.

Table 8.1: Calculated fiber volume fractions of the T-section.

	A_w (g/cm ²)	t (cm)	ρ_f (g/cm ³)	v_f
Skin	1.23	1.1176	1.8	0.61
Blade	1.80	1.7068	1.8	0.585

No compaction data were available for the region where the skin and flange are joined. For this region it was assumed that the skin fiber volume fraction was 61%, the same as for the rest of the skin. The flange fiber volume fraction was assumed to be 58.5%, the same as the blade fiber volume fraction. To test the sensitivity of the model to changes in the flange fiber volume fraction, the flange fiber volume fraction was run with both 58.5% and 61%. Very little difference in the fill times and pressures was observed.

To investigate the role that permeability played on the predicted pressures and fill times, three different models, designated as A, B, and C, were run. Table 8.2 summarizes the fiber volume fractions and permeabilities used in each finite element model. No data were available for the 14 tube braid, through-the-thickness permeability, so the permeability of the 4 tube braid at the same fiber volume fraction was used. The 4 elements at the inlet of the model were given a very high permeability of $1.0 \times 10^{-5} \text{ m}^2$ to minimize their effects on the inlet pressures.

8.2.3 Mesh Convergence

The mesh shown in Figure 8.4 was determined to be converged for both the flow times and the pressures at all 12 of the pressure taps.

The inlet area of the mesh was not converged. Three different local models of the inlet area were run. One had 2x2 elements covering the inlet, one had 4x4, and one had 8x8. This

Table 8.2: Three-dimensional flow model fiber volume fractions and permeabilities.

Model	Permeabilities in m^2			
	Skin	Blade	Flange	Fillet
A v_f	0.61	0.585	0.585	(Use flange perms)
IPP	3.72×10^{-12}	8.50×10^{-12}	1.36×10^{-11}	1.36×10^{-11}
IPN	1.60×10^{-12}	5.43×10^{-12}	4.88×10^{-12}	4.88×10^{-12}
TTT	6.41×10^{-13}	$6.01 \times 10^{-13*}$	6.01×10^{-13}	6.01×10^{-13}
B v_f	0.645	0.606	0.606	(Use flange perms)
IPP	1.90×10^{-12}	4.48×10^{-12}	7.77×10^{-12}	7.77×10^{-12}
IPN	8.00×10^{-13}	2.71×10^{-12}	2.79×10^{-12}	2.79×10^{-12}
TTT	4.13×10^{-13}	$4.44 \times 10^{-13*}$	4.44×10^{-13}	4.44×10^{-13}
C v_f	0.645	0.606	0.606	N/A
IPP	1.90×10^{-12}	4.48×10^{-12}	7.77×10^{-12}	1.0×10^{-10}
IPN	8.00×10^{-13}	2.71×10^{-12}	2.79×10^{-12}	1.0×10^{-10}
TTT	4.13×10^{-13}	$4.44 \times 10^{-13*}$	4.44×10^{-13}	1.0×10^{-10}

* No 14 tube TTT data available, computed using 4 tube TTT fit.

area of the model is difficult to model accurately for a number of reasons. First, 3DINFIL only uses brick type elements which are good for modeling angular geometry, while the inlet is round. Second, local models of the inlet area were very large and used up to 96 hours of CPU time on an SGI Origin machine. Even though the local models had not converged, the model was predicting pressures of at least three to five times greater than those measured in the experiment, and the pressure was rising with every mesh refinement. It was determined that the fixture was probably leaking at the inlet port between the mold surface and the bottom of the preform, so no further attempts to refine the inlet mesh were made.

It was also found that changing the mesh size near the inlet had no effect on the calculated pressures or fill times at other locations in the model. Because the experiment was conducted with a constant flow rate, the pressures near the inlet did not affect the rest of the model for the mesh shown in Figure 8.4.

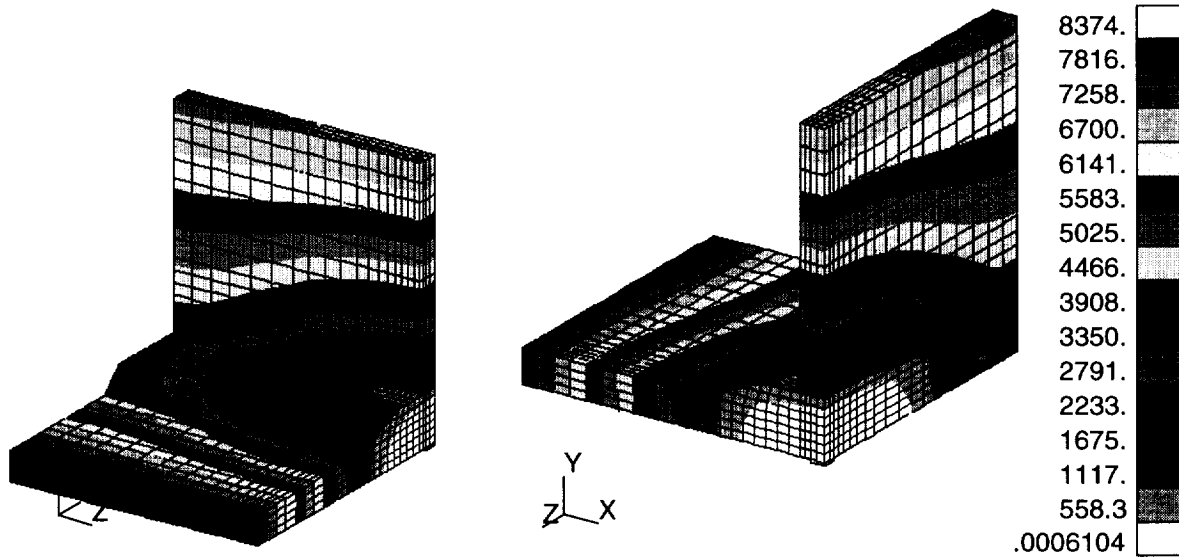


Figure 8.6: Case A flow front progression. The color bands represent the flow front location at different times. The units are in seconds.

8.3 Results

The predicted flow front locations for the three models are shown in Figures 8.6–8.8. Two experimental runs were performed at 3 cc/min. Shown in Figures 8.9–8.13 are comparisons between the measured pressures and the finite element model predicted pressures. Comparison of the predicted and measured infiltration times is shown in Figures 8.14 and 8.15.

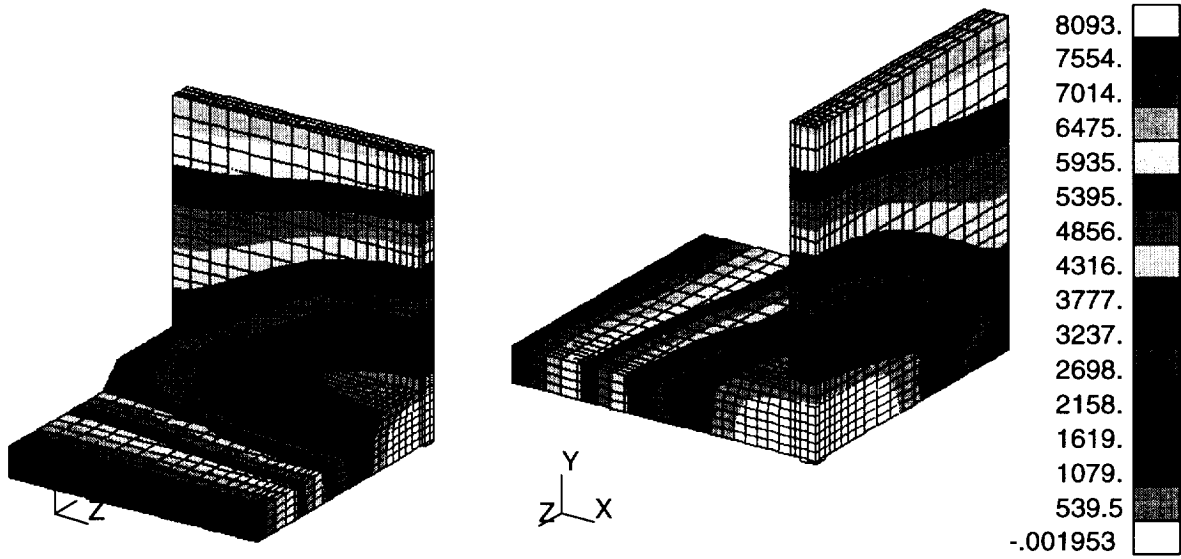


Figure 8.7: Case B flow front progression. The color bands represent the flow front location at different times. The units are in seconds.

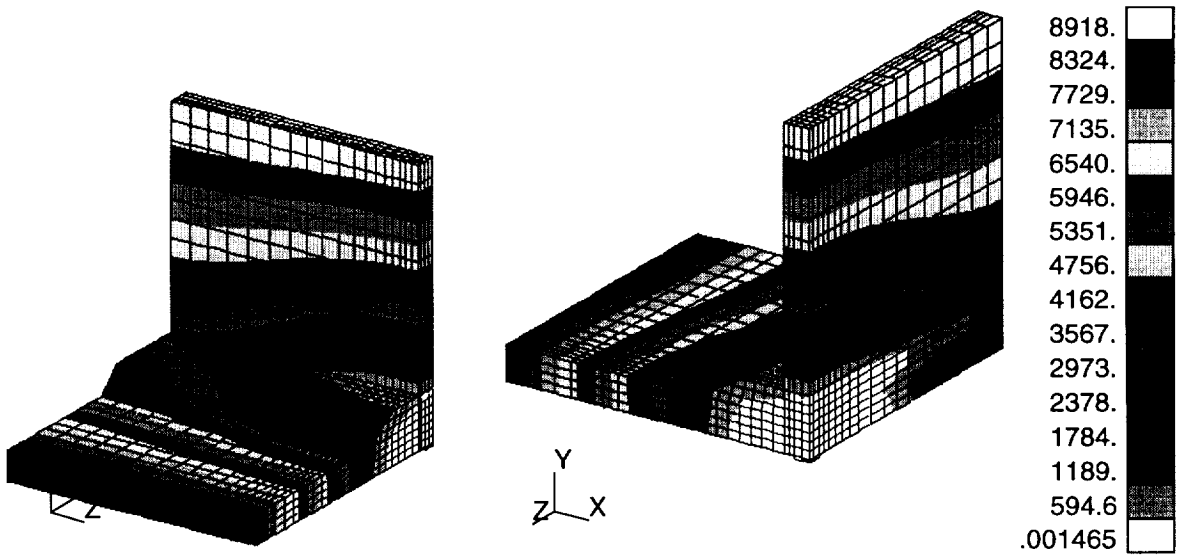


Figure 8.8: Case C flow front progression. The color bands represent the flow front location at different times. The units are in seconds.

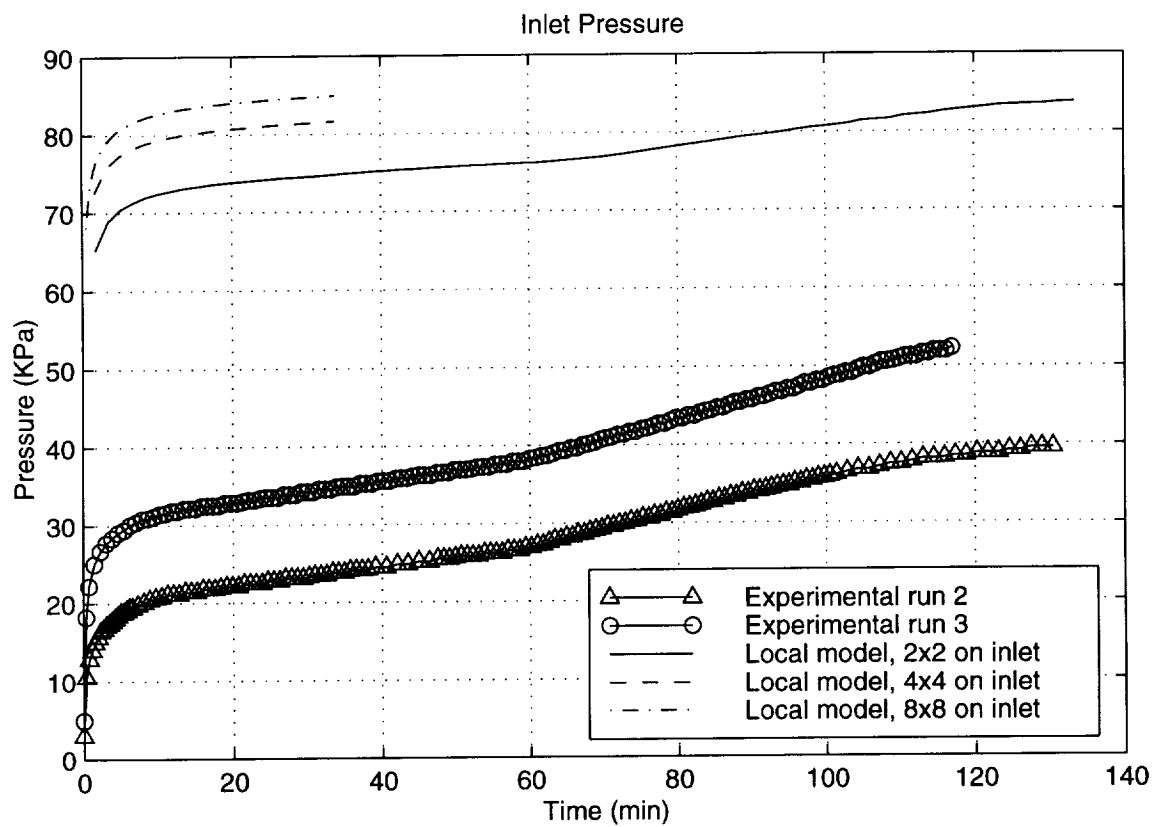


Figure 8.9: Inlet pressures for different meshes.

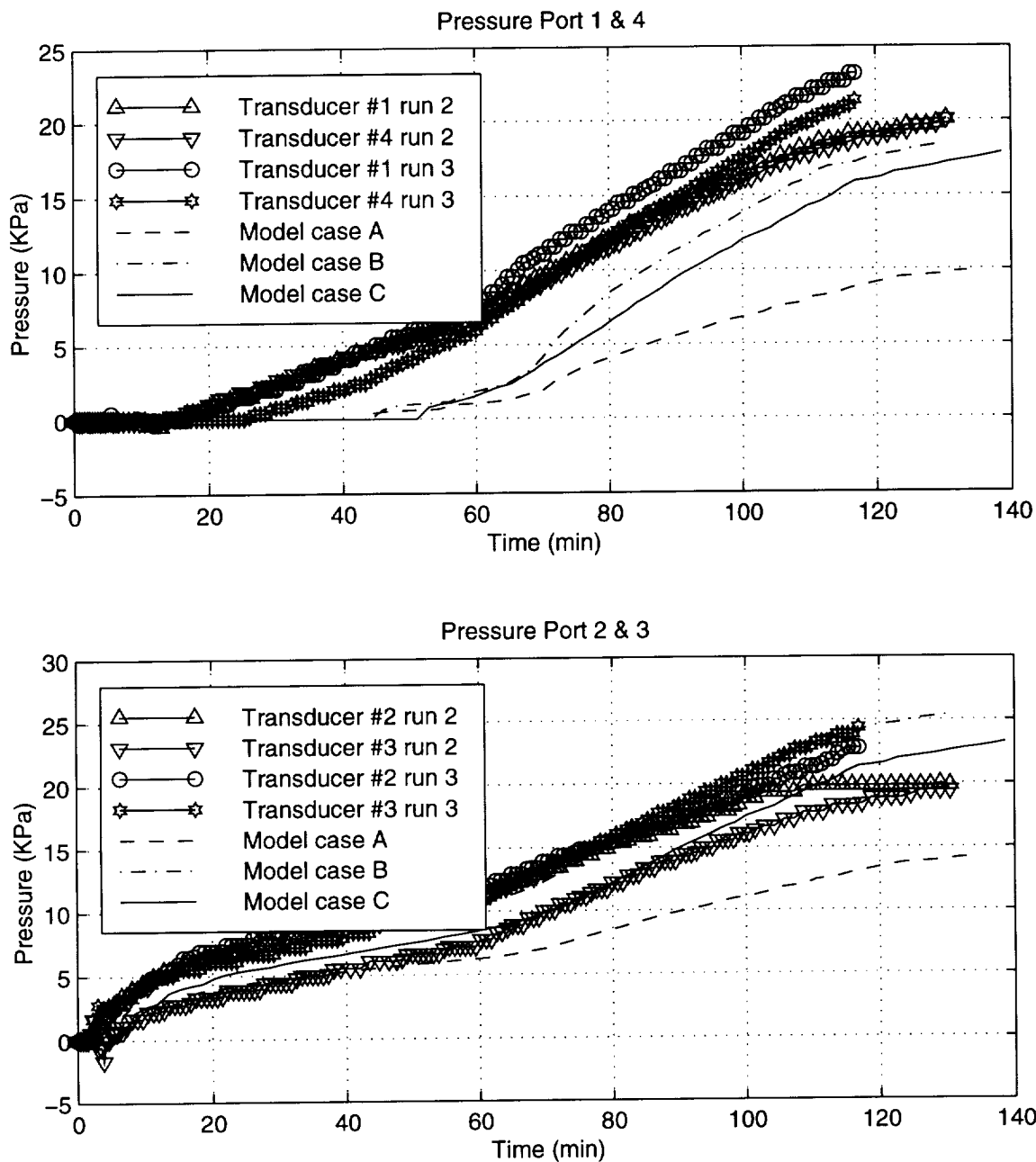


Figure 8.10: Comparison between the measured and model predicted pressures at ports 1 & 4 and 2 & 3. Pressure transducer locations are shown in Figure 8.3.

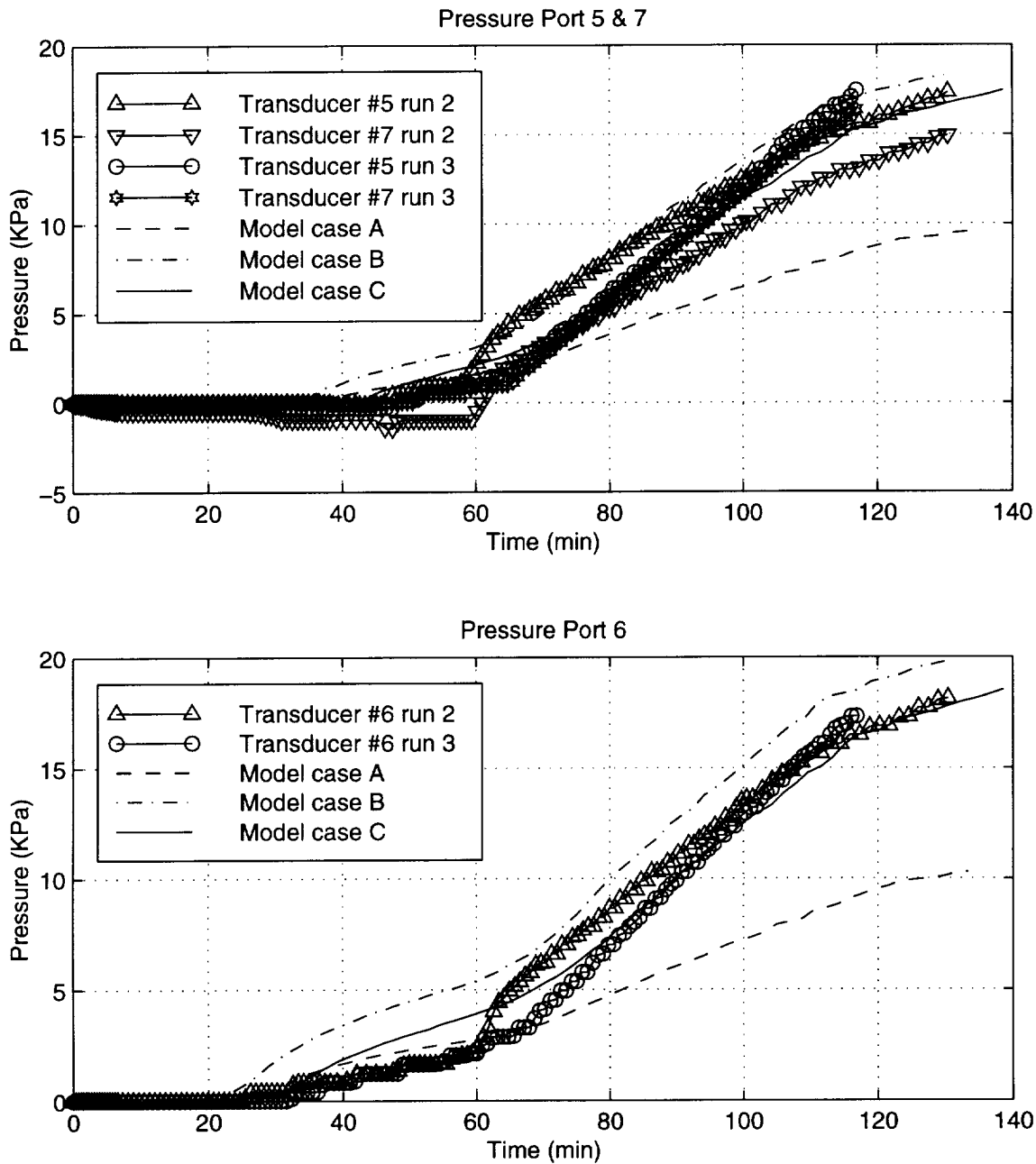


Figure 8.11: Comparison between the measured and model predicted pressures at ports 5 & 7 and 6. Pressure transducer locations are shown in Figure 8.3.

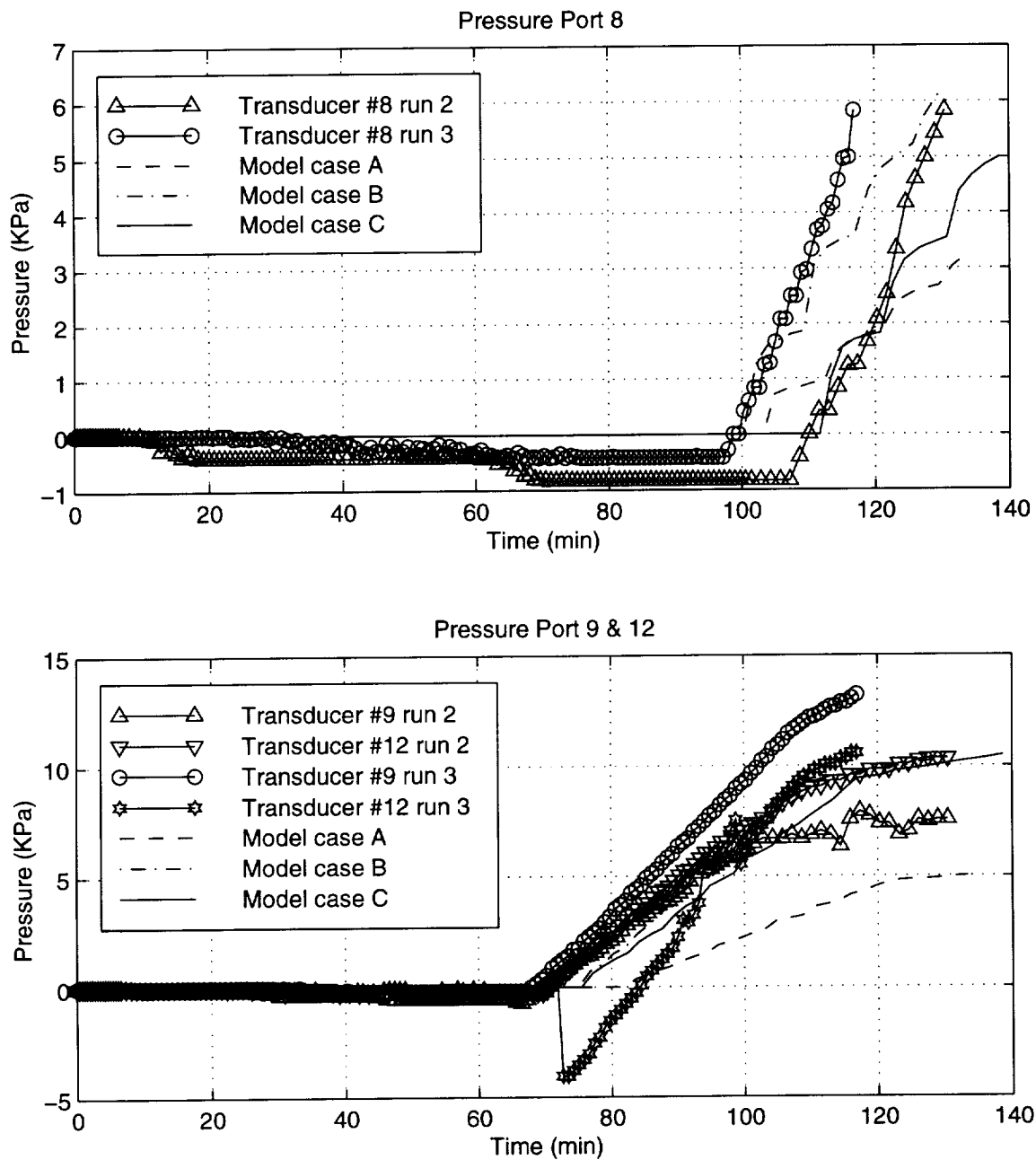


Figure 8.12: Comparison between the measured and model predicted pressures at ports 8 & 9 and 12. Pressure transducer locations are shown in Figure 8.3.

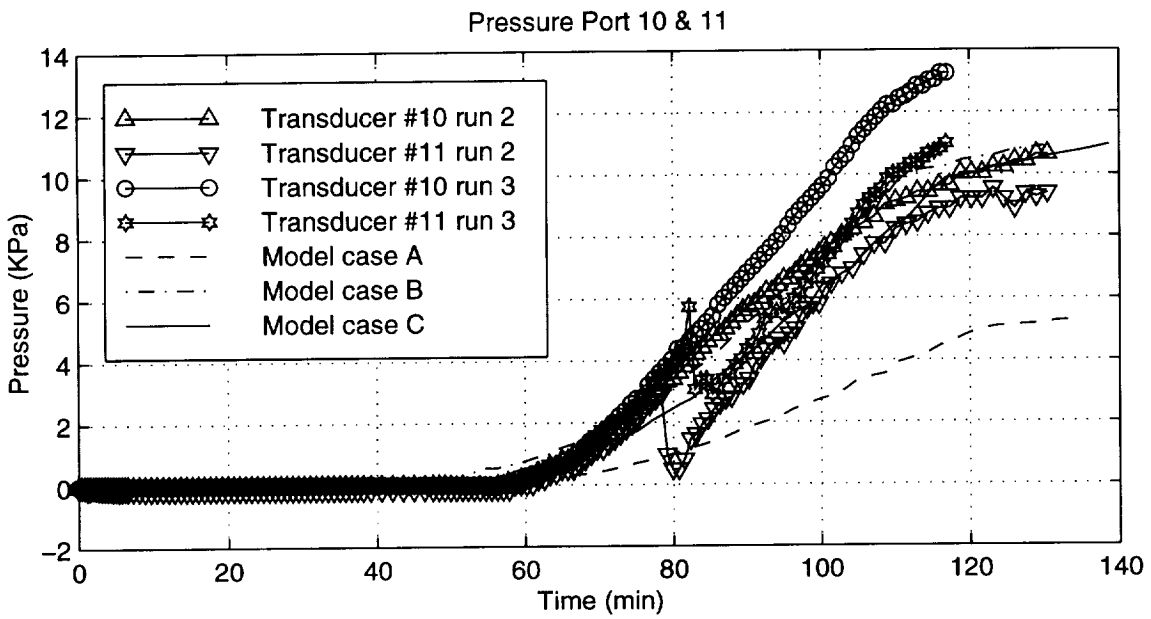


Figure 8.13: Comparison between the measured and model predicted pressures at ports 10 & 11. Pressure transducer locations are shown in Figure 8.3.

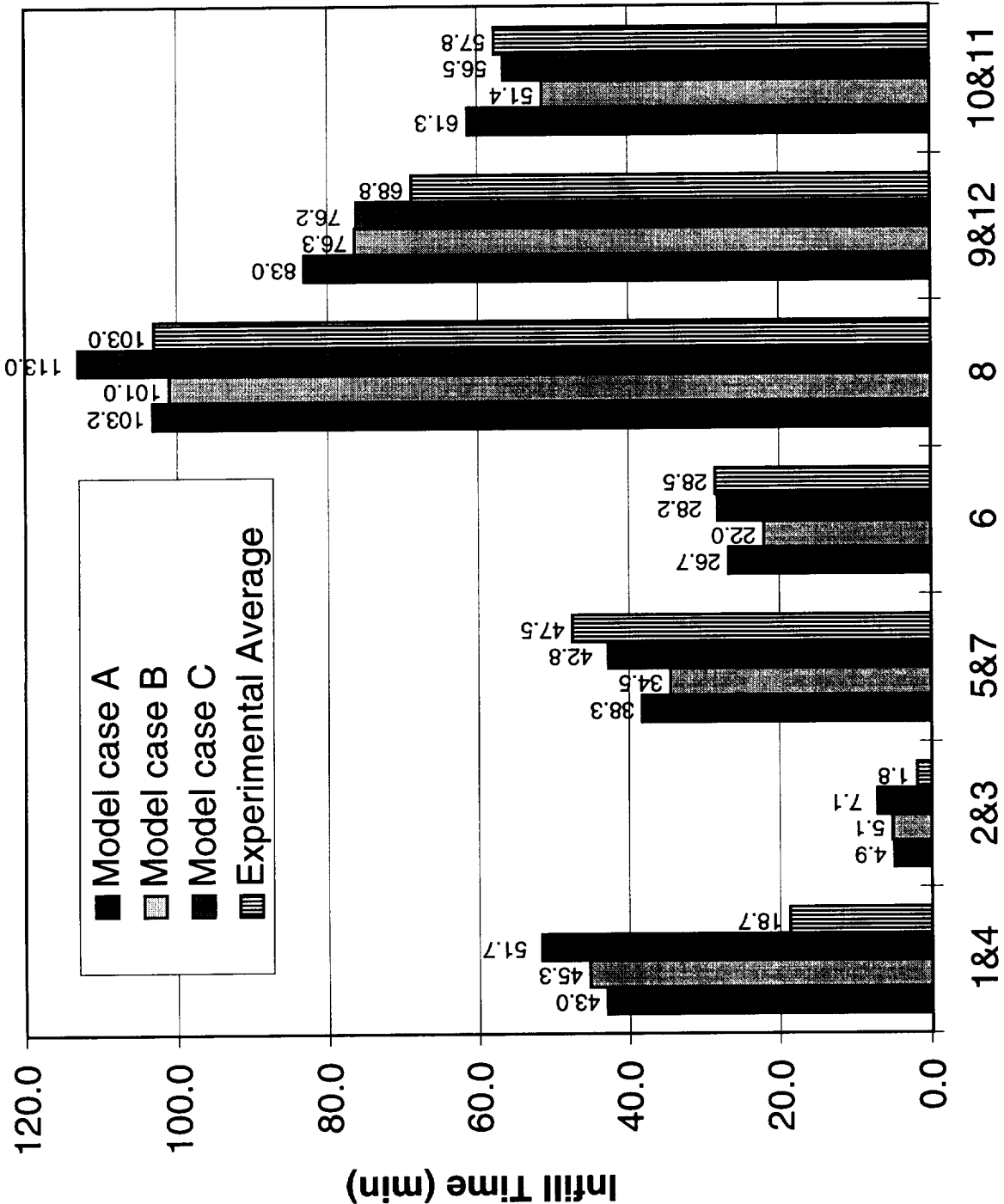


Figure 8.14: Experimental and predicted infiltration times for the flow verification model.

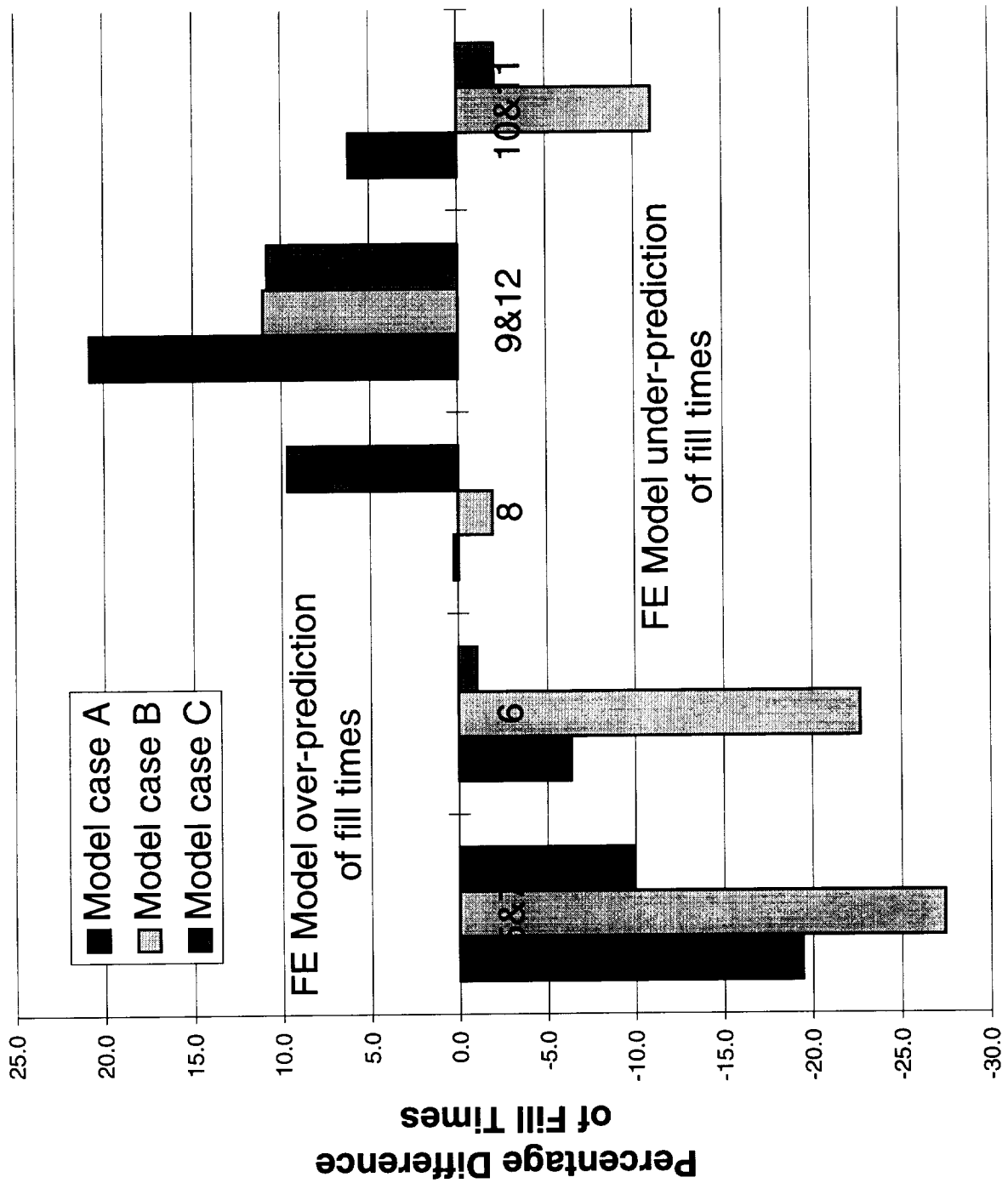


Figure 8.15: Percent difference of wet out times for the flow verification model.

8.4 Discussion

8.4.1 Inlet Pressure

The measured and model A predicted pressures for the inlet pressures are shown in Figure 8.9 on page 77. The 4x4 and 8x8 cases were local models of the inlet, so they were only valid for the first 34 minutes of the simulation. The model has obviously not converged, but it can be seen that the pressures are increasing with each mesh refinement. The predicted pressures are about three to four times higher than the measured pressures. The inlet is the only port in case A where the model overpredicted the pressures. At all of the other ports the model underpredicted the pressures. This suggests that the fluid may be compressing the preform near the inlet and leaking between the skin and the baseplate. The infiltration times shown in Figure 8.14 for ports 1&4 and 2&3 support the idea that there is a leak path near the inlet. All three simulation models overpredict the infiltration time of these ports.

The leak path probably exists because the area under the blade is not supported on both sides by the mold and no direct compaction of that area is available.

8.4.2 Skin, Flange, and Blade Pressures

The pressure curves predicted by case A show the same general shape as the experimental curves, but they seem to be too low by a factor of two. One input that may be causing this mismatch is incorrect permeabilities being used in the model. The permeabilities of the materials were calculated from only two or three samples, and all of these samples came from the same batch of materials. The preforms were constructed from a different batch, and the batch-to-batch variability of these materials is unknown. Another factor

that would affect the permeability is the actual areal weight of the preform. Again, there is no data on the batch-to-batch variability of this quantity.

To attempt to match the pressures, the in-plane permeabilities would have to be reduced by a factor of two. One method to vary the permeabilities would have been to individually vary each principal permeability and check its effect on the pressures. This did not seem appropriate because the three principal permeabilities are not independent of each other, but they all depend on the fiber volume fraction of the preform. Therefore, to affect this change in the permeabilities, it was decided to find a fiber volume fraction that would result in a reduction of the in-plane permeabilities by a factor of two. The fiber volume fractions found were 64.5% for the skin and 60.6% for the blade. The permeabilities calculated from these fiber volume fractions are listed in Table 8.2 on page 74. The model run designated as case B used these permeabilities.

On comparing the flow front shapes of case A (Figure 8.6) and case B (Figure 8.7), there is no significant change in the shape of the front. The calculated pressures from case B match the experimental curves well.

Details of case C will be discussed in the next section, but it should be noted that the predicted pressures of case C also match the experimental curves well.

8.4.3 Fill Times

Once the pressures had been matched, an effort was made to more precisely model the preform. In cases A and B, the unidirectional fibers in the fillet region were not taken into account, and the elements in those models were given the same permeability as the flange region. Case C attempted to model the fillet region more accurately. The fillet region was given a higher permeability of $1 \times 10^{-10} \text{ m}^2$. Inspecting the flow front shape of case C in

Figure 8.8 shows that the fluid tends to prefer to flow along the fillet region before it fills the rest of the preform. After the flow fills the area around the inlet, it becomes mostly planar as it flows up the blade and across the skin.

Figures 8.14 and 8.15 show graphs comparing the predicted and measured infiltration times. Model case C agrees with the experiment to within about $\pm 10\%$.

Chapter 9

Stepped Panel Simulation

A three-dimensional model was used to simulate the resin film infusion processing of a stepped textile preform.

9.1 Experiment

9.1.1 Preform and Tooling

The textile preform used in this experiment was constructed from stacks of the warp knit fabric described in Chapter 6. Figure 9.1 is a sketch of the preform. Each step is two stacks thick. The thinnest part of the preform is two stacks thick and the thickest is eight stacks. After stitching, eight stacks are approximately 1 cm thick. The preform weighed 1961 g ($1520 \text{ g/m}^2/\text{stack}$).

Figure 9.2 shows a sketch of the tooling used to process the panel. Both the base plate and the top plate were constructed from 6061-T6 aluminum. The base plate was approximately $1.27 \text{ cm} \times 76.2 \text{ cm} \times 152.4 \text{ cm}$. The top plate was 25.4 cm wide and 101.6 cm long and

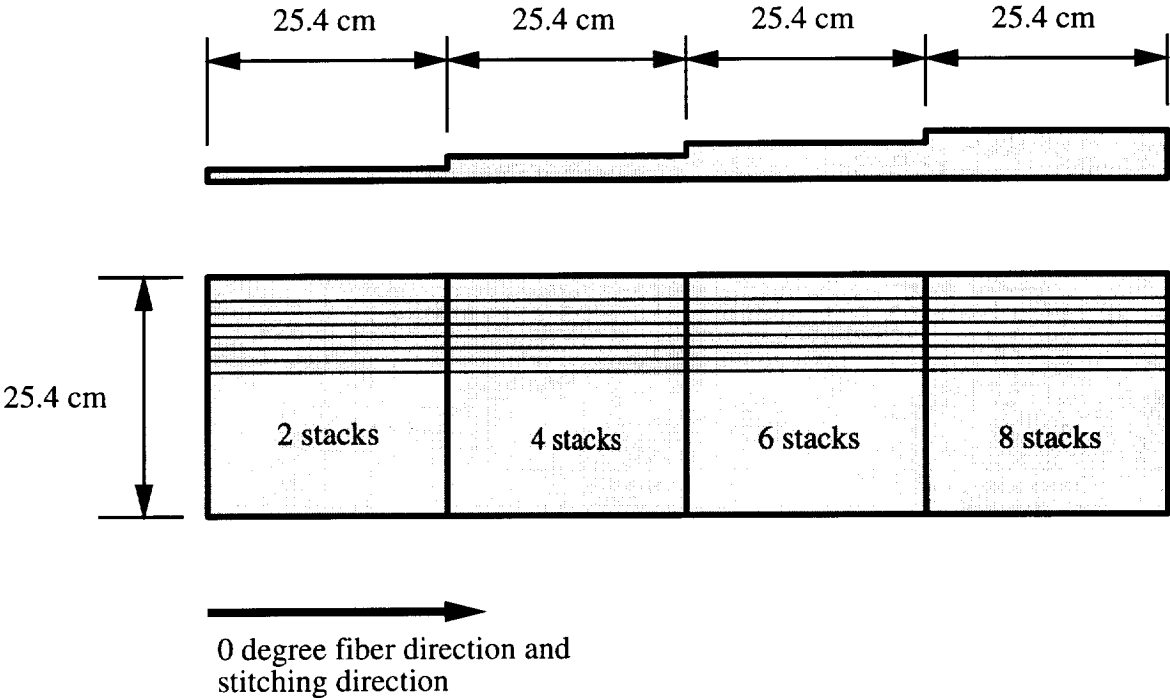


Figure 9.1: Dimensions of the stepped preform.

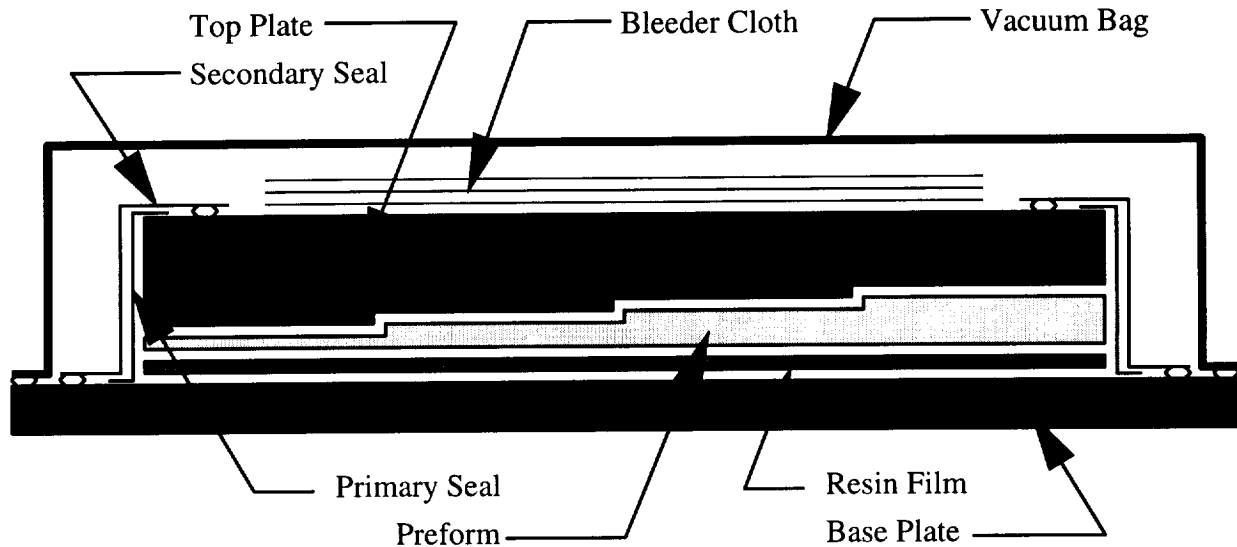


Figure 9.2: Tooling and layup of the stepped panel.

its thickness ranged from 1.590 cm to 2.413 cm. Detailed drawings of the top and bottom plates can be found in Appendix A.

9.1.2 Procedure

First, the top and bottom plates were instrumented with thermocouples, Dek Dyne frequency dependent electromagnetic sensors (FDEMS), and Entran pressure transducers, model EPX0-X03-150P with a 7.6 mm tip. The thermocouple, FDEMS, and transducer locations are shown in Figures 9.3–9.5, respectively. Thermocouples 1–4 were located between the preform and the top mold, 5–7 were located between the baseplate and the resin, and 8–12 were located in the autoclave air. Thermocouples 8–12 had their leads taped to the part, and the leads were bent so the head was about 5 centimeters away from the part. Thermocouple 3 failed during the experiment.

The pressure transducers were recessed into the tooling to minimize their effects on the

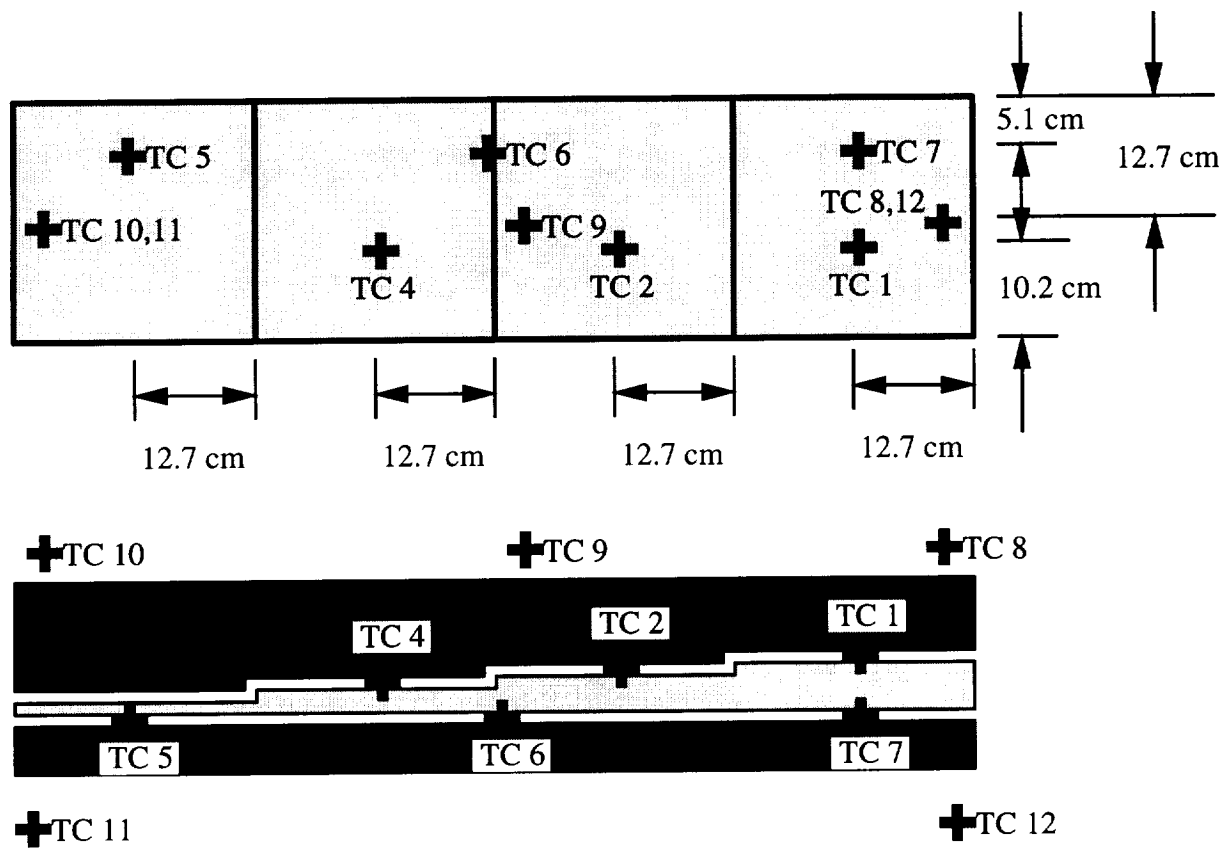


Figure 9.3: Locations of the thermocouples on the stepped preform.

flow front.

A FDEMS consists of a fine array of two interdigitated comb electrodes. These sensors can be used to monitor in situ the processing properties of thermoset resins. The FDEMS is able to monitor the progress of cure, viscosity, and buildup in modulus. The data obtained from the sensors in this experiment was used to detect the passage of the flow front. Details regarding the sensor measurements are described in [31].

This experiment used the reduced catalyst 3501-6 resin. The resin was degassed at 85°C for 25 minutes in a vacuum oven. The degassing process formed 25.4 cm × 25.4 cm resin tiles. Each tile was approximately 0.6 cm thick and the total resin weight was 1208 g. The

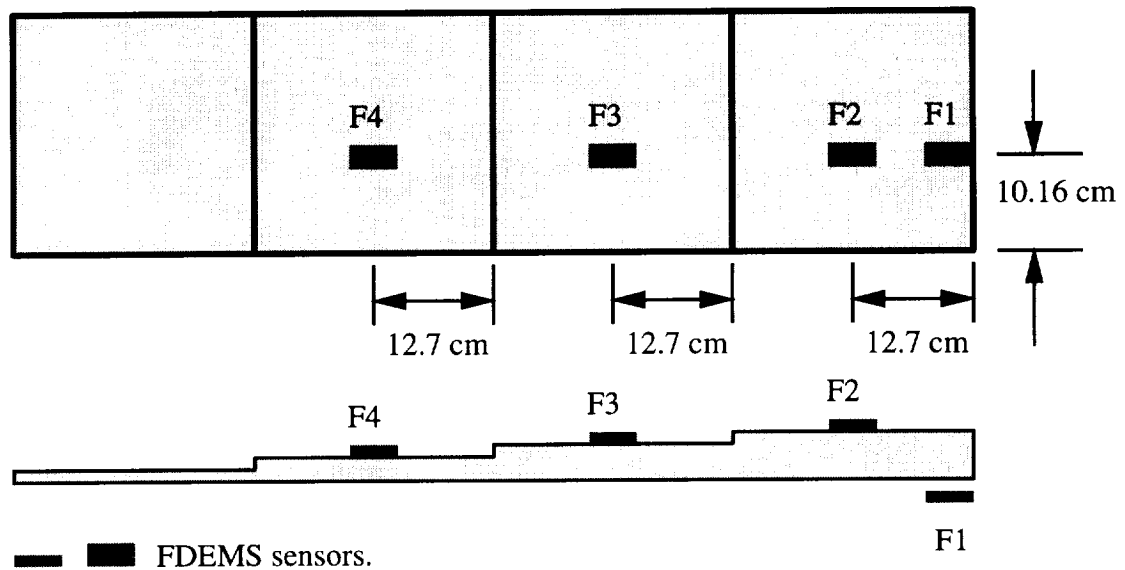


Figure 9.4: Locations of the FDEMS on the stepped preform.

resin sheets were placed on the baseplate, and the preform was placed on top of the resin sheets. Next, the top mold was placed over the preform. Two seals were used around the edges of the preform. The primary seal consisted of 5 cm flashing tape. The secondary seal was constructed from nylon bagging material. Finally, the bleeder, separator, and vacuum bag were laid into place.

The expected final fiber volume fraction was 54% after the excess resin was allowed to bleed through the FDEMS lead holes. The bleeder material consisted of 1.21 m² of 162 glass fabric.

9.2 Simulation Model

Two different models were built to simulate the RFI process in the stepped panel. The initial model was a one-element-thick slice of the RFI assembly. This model was constructed

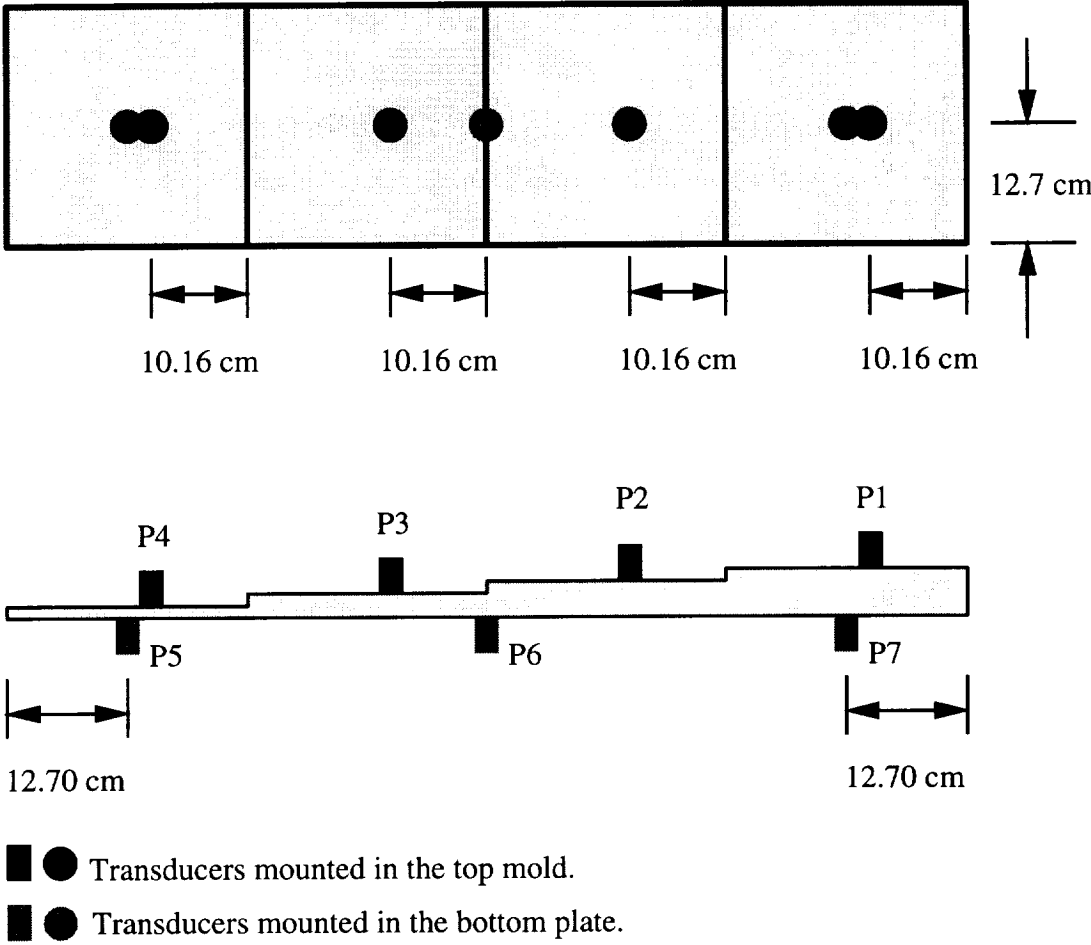


Figure 9.5: Locations of the pressure transducers on the stepped preform.

because it would run quickly and give initial estimates of the fill times, temperatures, heat transfer coefficients, and mesh requirements to model this experiment. The final model was a full three-dimensional model. From this model the full three-dimensional flow field was found, and the fill times were determined.

9.2.1 Model Geometry

The expected thickness of the preform was 1.37 mm per stack, or 2.74 mm per step. The actual top plate was machined to these step heights. To try and more accurately model the experiment, the thickness of each step of the preform was modeled using the cured thickness of the panel. The measured thicknesses of each step were: 2 stack, 3.18 mm; 4 stack, 5.89 mm; 6 stack, 8.38 mm; and 8 stack, 11.02 mm. Because the actual thickness of each step was not the same as the expected thickness, the model of the top plate had to be adjusted. The model of the top plate was dimensioned to fit against the top of the preform model by adjusting the step heights of the top plate model. The thin end of the top plate was modeled as 15.90 mm thick, while the thick end was modeled as 23.75 mm thick.

One reason the actual thicknesses of the steps were not the expected values was due to the presence of resin rich areas at the bottom of the cured panel. This resin did not fully infiltrate the preform, but “puddled” on the bottom of the panel. Another reason could have been that the preform did not compact uniformly, and the top plate compacted the 8 stack step more than the 2 stack step.

Figure 9.6 shows a sketch illustrating the mesh used for the initial model. This model is one element thick in the Z-direction. Each step has eight elements in the in-plane (X) direction, and 2 elements in the through-the-thickness (Y) direction. The top plate had 14 elements on the left most step, and drops off two elements per step to 8 elements on the

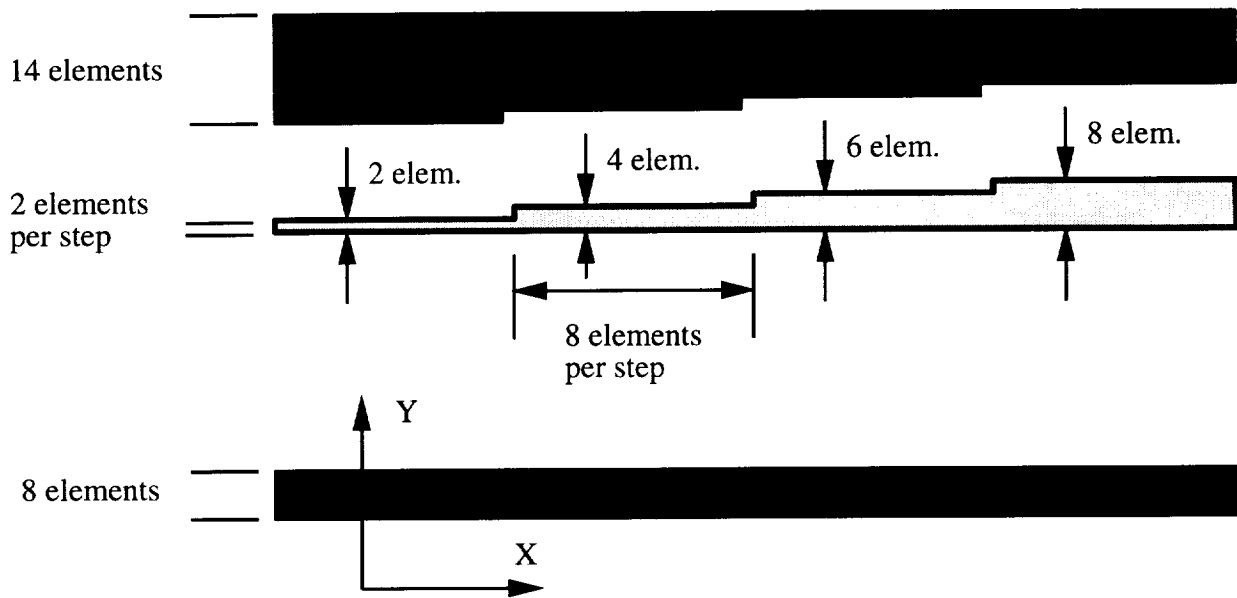


Figure 9.6: Initial one-element-thick finite element model.

right step. The baseplate had 8 elements through the thickness and 32 along its length.

A picture of the final model is shown in Figure 9.7. Only half of the actual preform/tooling assembly was modeled due to the plane of symmetry down the middle. The final model included the large baseplate used in processing. The baseplate extends approximately 25 cm to each side of the preform. The mesh for the final model is very similar to the initial model. In the final model, the elements are smaller near the edges of the preform that are in contact with the autoclave air. This was done because high thermal gradients had been observed in the initial model near these areas.

A summary of the finite element meshes and run times for each model is shown in Table 9.1. Both models were run on an SGI Origin system.

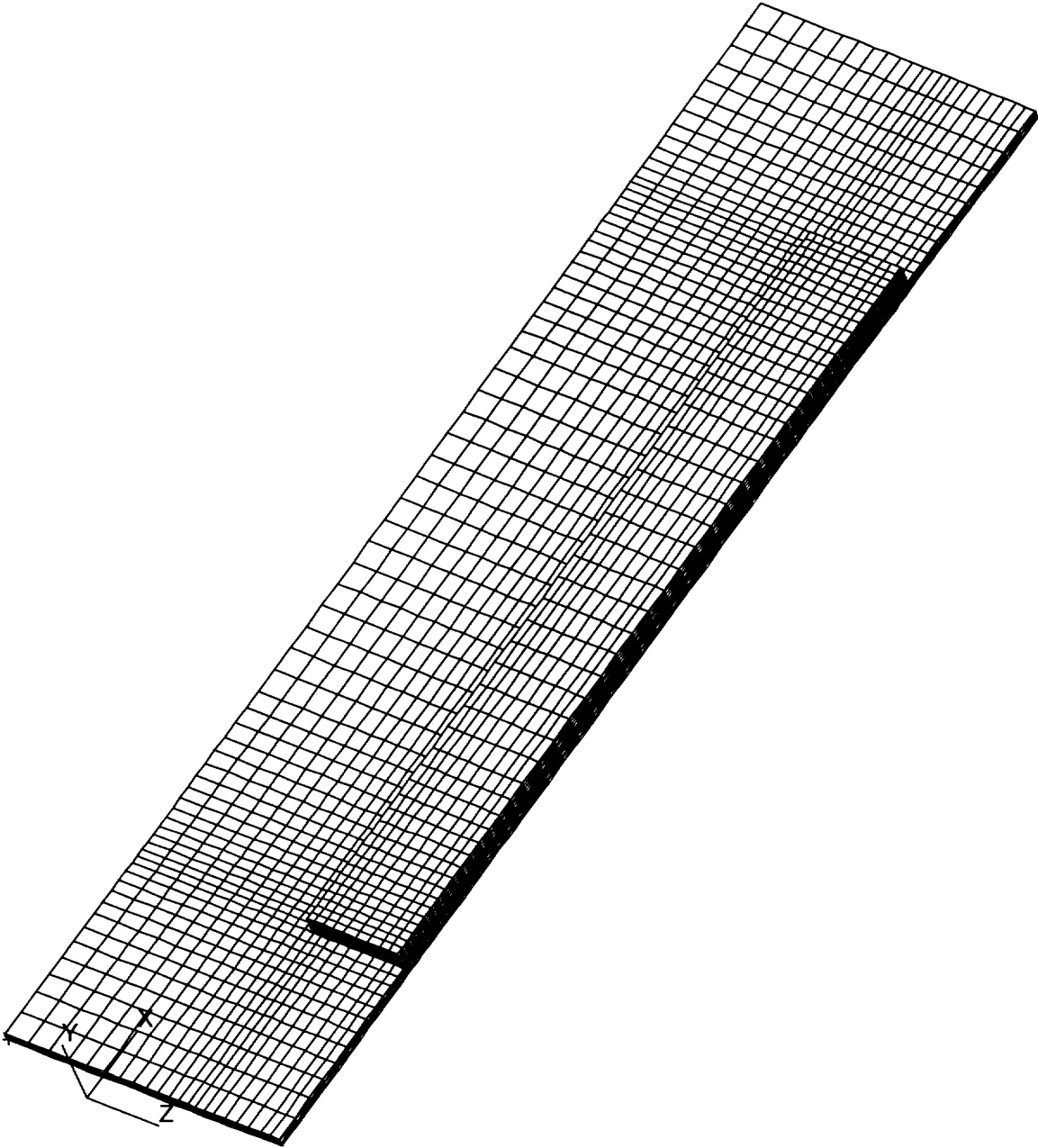


Figure 9.7: Final three-dimensional finite element model.

Table 9.1: Size and Run Time of the Models.

Model	Flow Model		Thermal Model		CPU Time (min)
	Nodes	Elements	Nodes	Elements	
Initial	534	224	1782	832	2.3
Final	3460	2592	14400	11664	396.3

9.2.2 Boundary Conditions

The only boundary condition on the flow model was the autoclave pressure. The pressure was ramped from 101 kPa to 791 kPa in 10 minutes, then held constant.

Actual thermocouple data were input for the temperature boundary conditions. The temperatures and where they were applied are shown in Figures 9.8–9.11. Thermocouples 8 and 9 were very similar, so one was chosen and applied over the area of both. The temperature profile of the bottom was assumed to be the same as the top, except different thermocouple data were used.

Another critical input to the simulation model is the convective coefficients. For the present experiment, the coefficients were not known. To attempt to model the process, the coefficients input to the model were varied until the experimental and simulated temperatures matched. The experimental thermal histories and predicted values for various convective coefficients are compared in Figures 9.12–9.17. The final values of the convective coefficients for the initial model were: bottom = 50 W/m²K, top = 40 W/m²K. A similar procedure was used for the final model. The coefficients for the final model were: bottom = 40 W/m²K, top = 35 W/m²K. The coefficients in the final model are lower because that model had convection on all sides of the preform, not just the top and bottom. The larger surface area provided for more heat transfer between the assembly and the air, hence a lower convective coefficient was required.

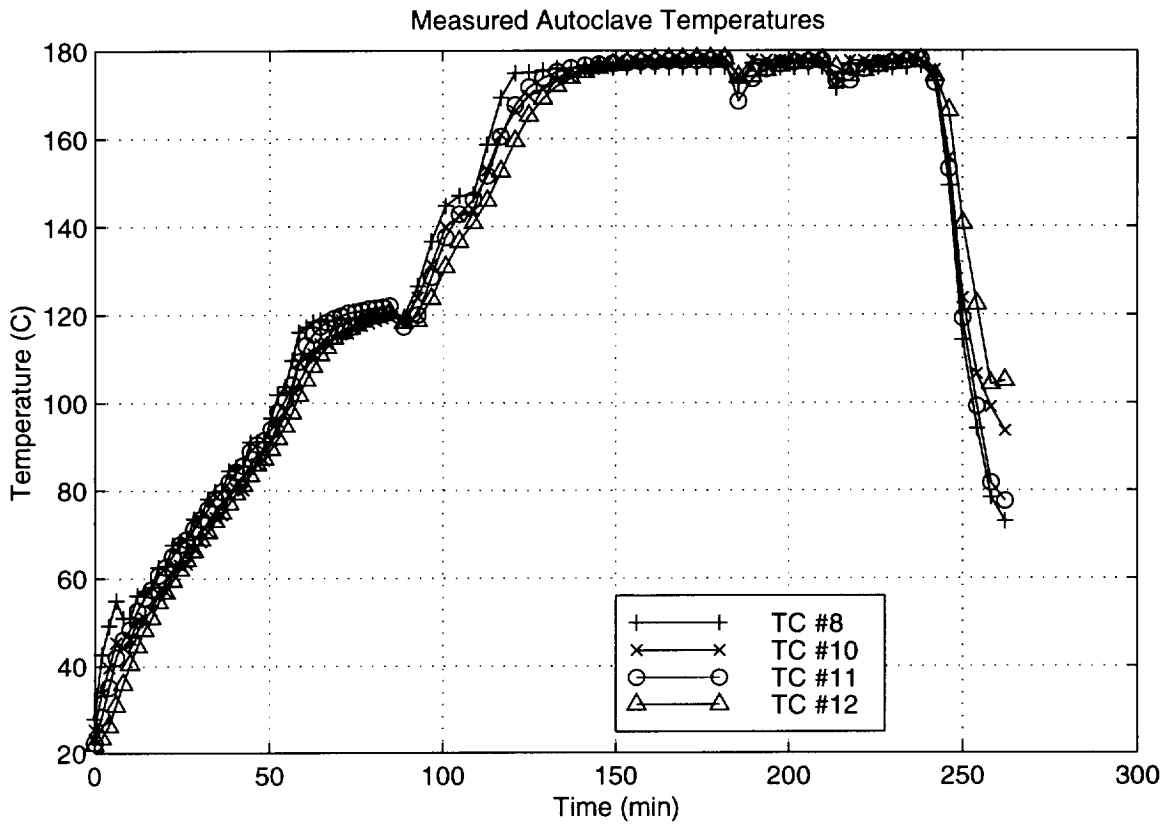


Figure 9.8: Measured autoclave temperatures during the stepped panel run.

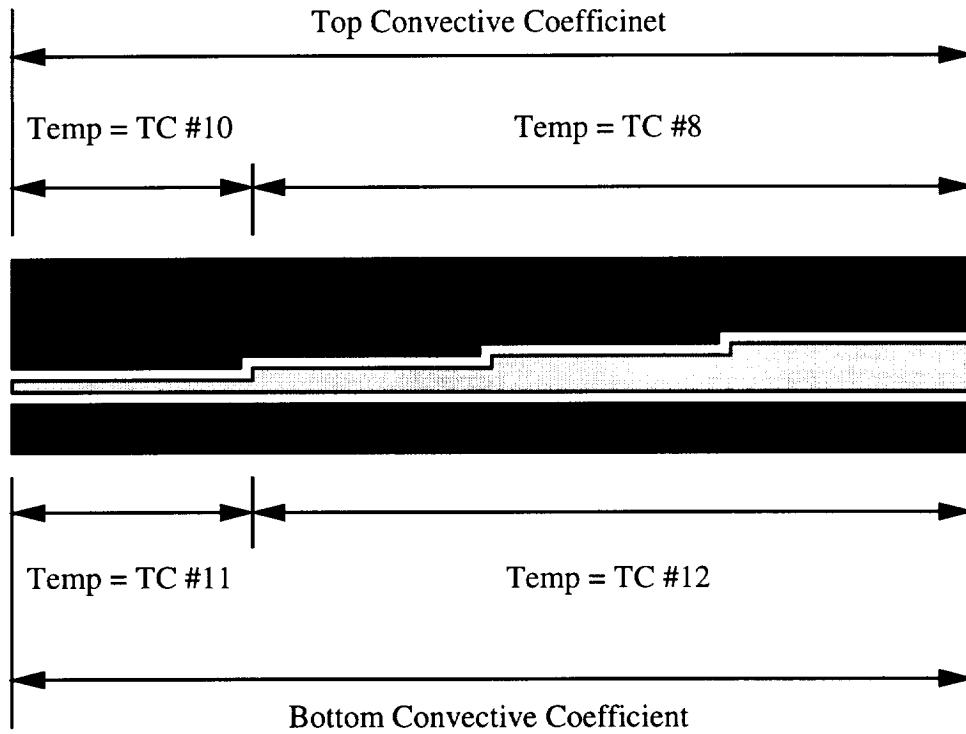


Figure 9.9: Applied temperature cycles for the initial model.

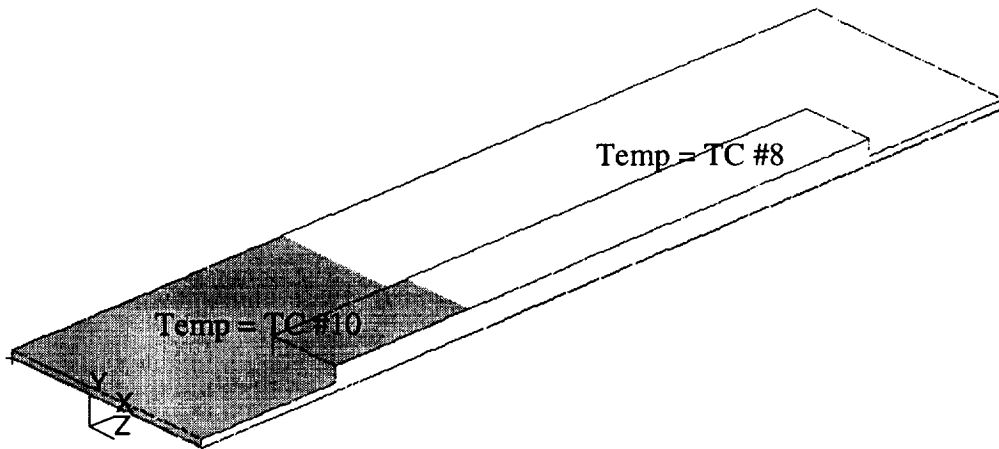


Figure 9.10: Applied temperature cycles to the top of the final stepped model.

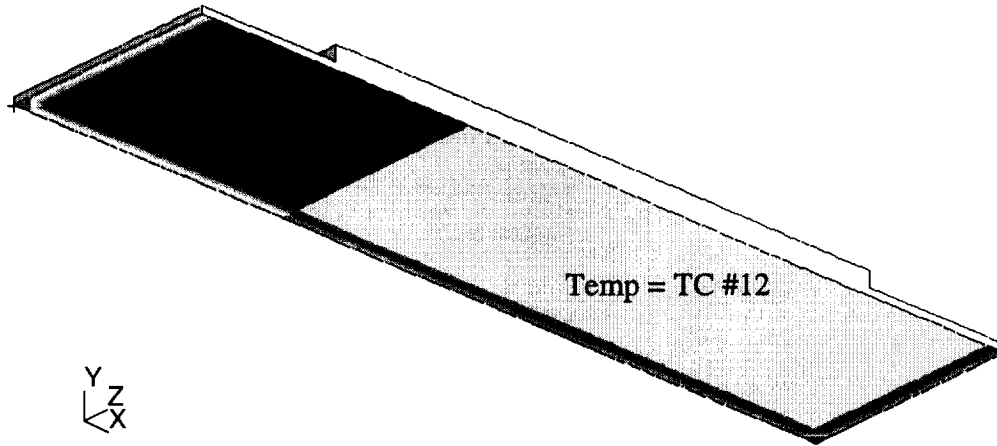


Figure 9.11: Applied temperature cycles to the bottom of the final stepped model.

All error estimates were calculated against the total temperature variation of the applied temperature cycle. The variation was $177^{\circ}\text{C} - 25^{\circ}\text{C} = 152^{\circ}\text{C}$, and Equation (9.1) was used to calculate the error.

$$100\% \times \frac{(\text{predicted temp}) - (\text{experimental temperature})}{177 - 25} \quad (9.1)$$

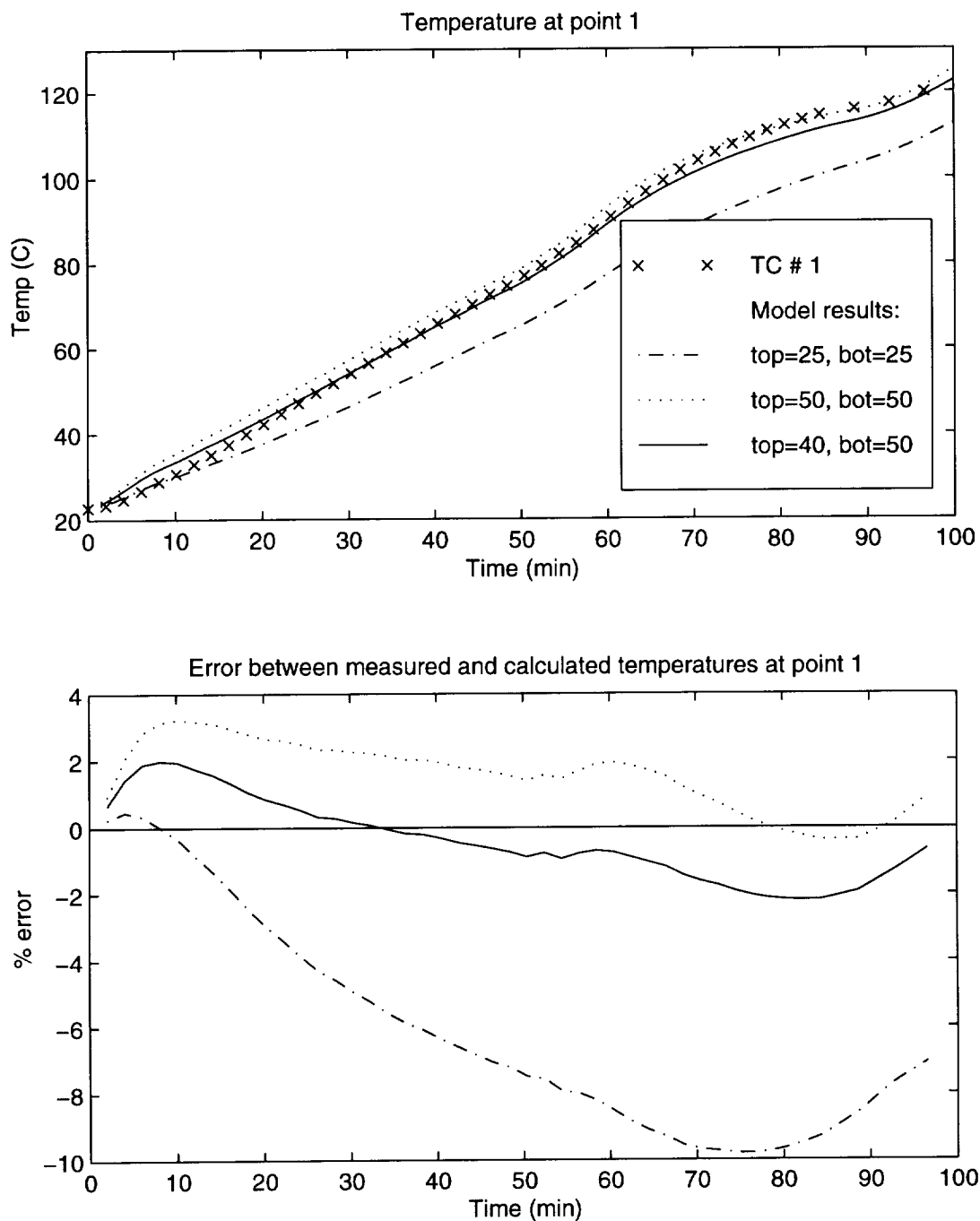


Figure 9.12: Temperature profiles at thermocouple location 1 for various convective coefficients. Thermocouple locations are shown in Figure 9.3.

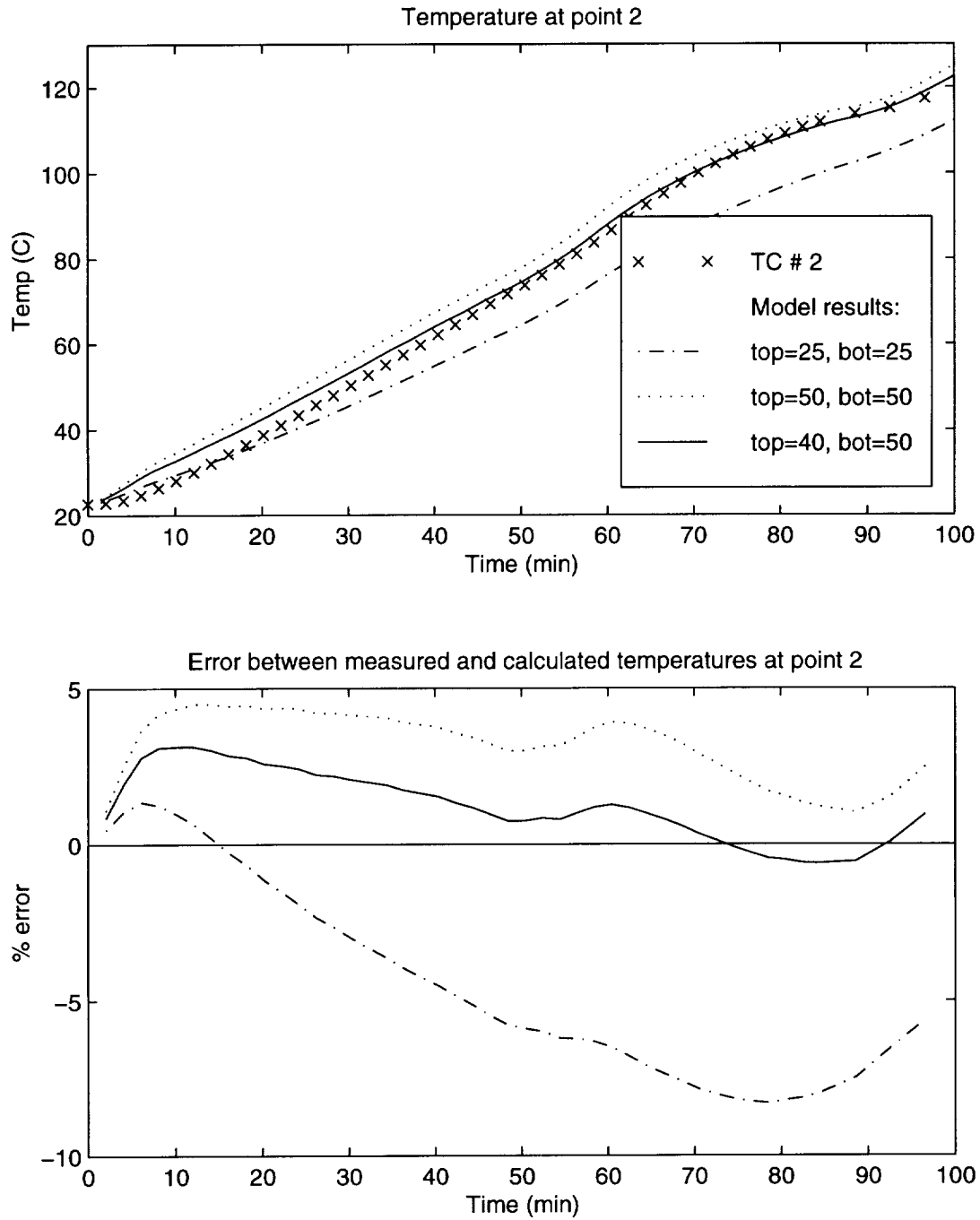


Figure 9.13: Temperature profiles at thermocouple location 2 for various convective coefficients. Thermocouple locations are shown in Figure 9.3.

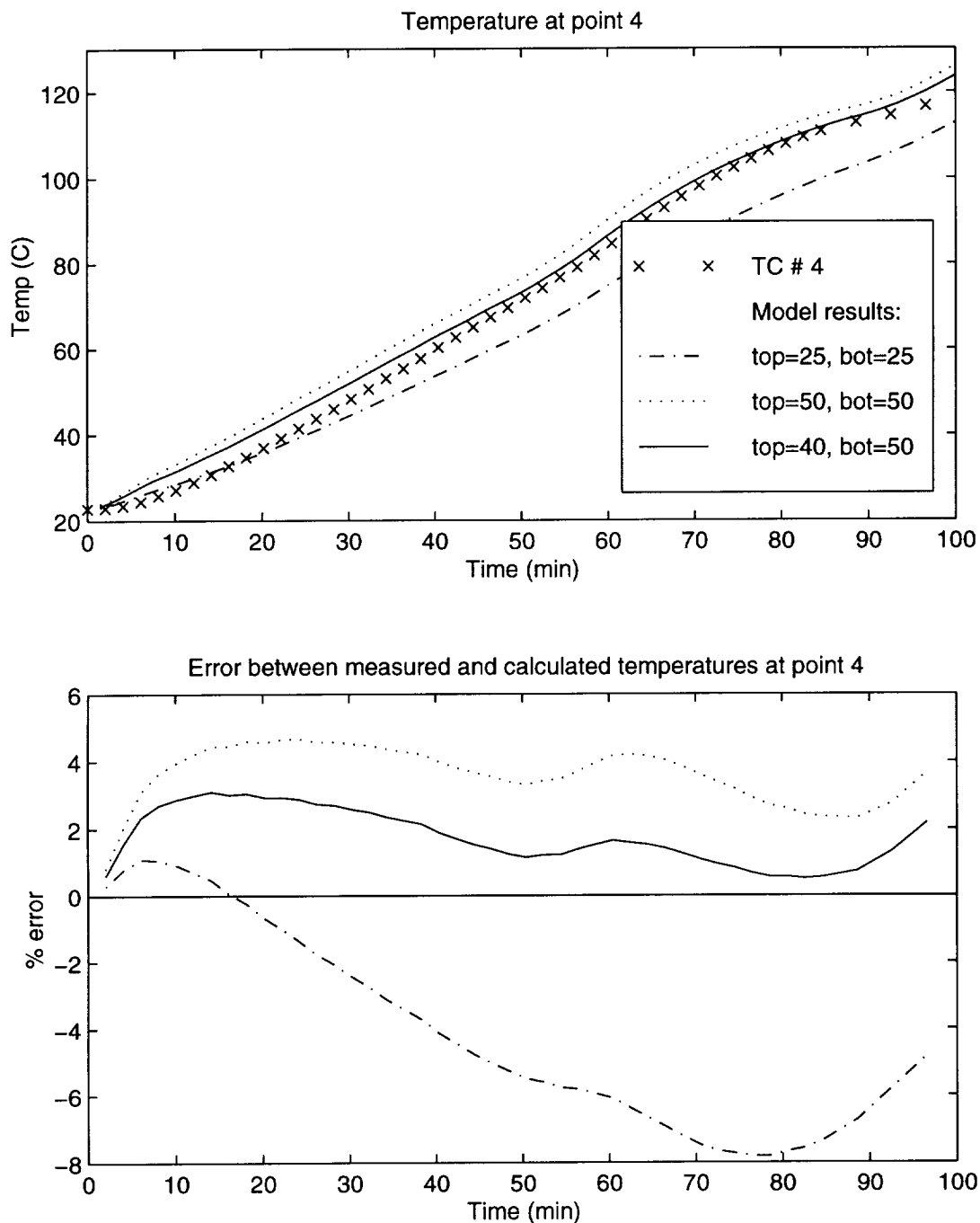


Figure 9.14: Temperature profiles at thermocouple location 4 for various convective coefficients. Thermocouple locations are shown in Figure 9.3.

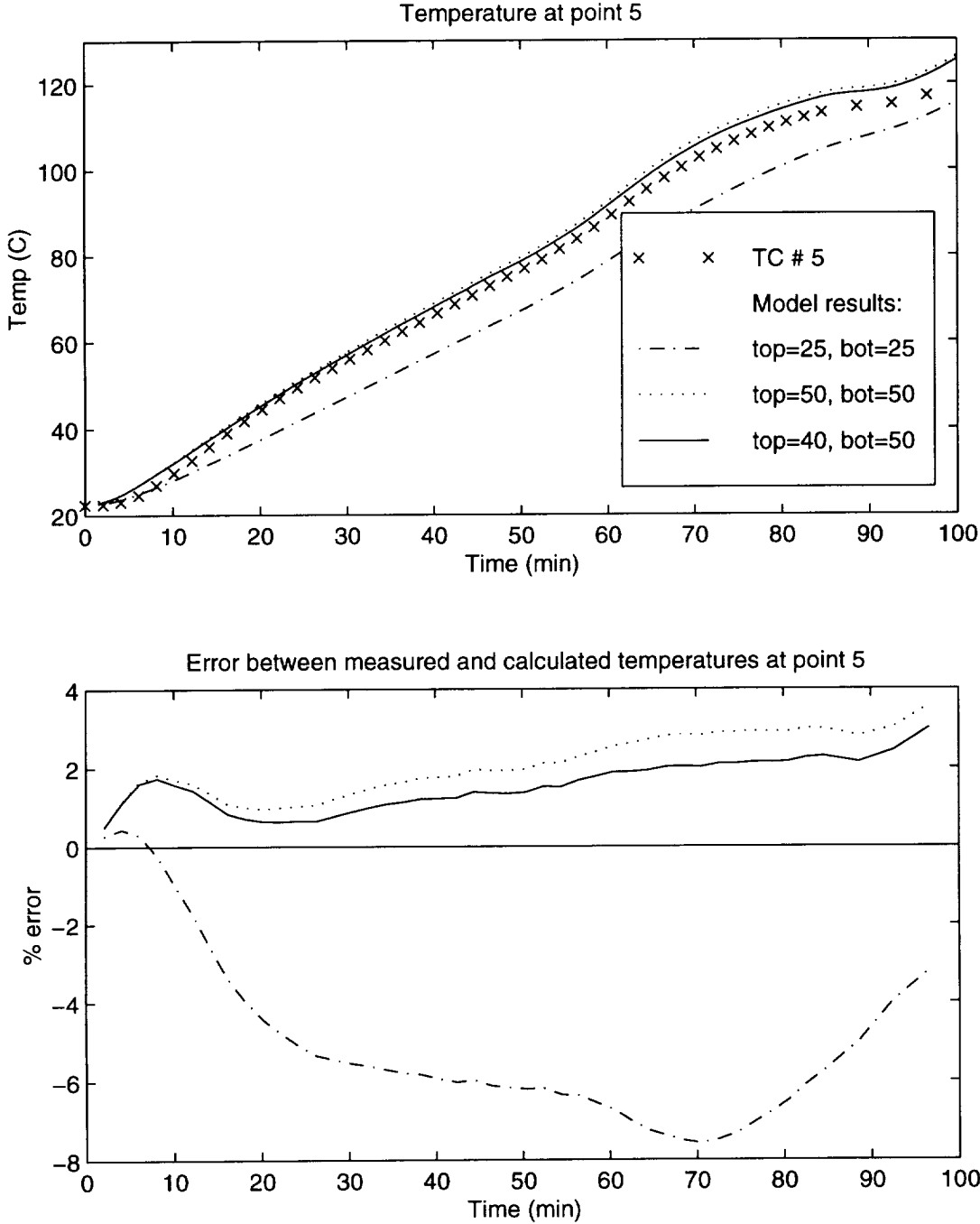


Figure 9.15: Temperature profiles at thermocouple location 5 for various convective coefficients. Thermocouple locations are shown in Figure 9.3.

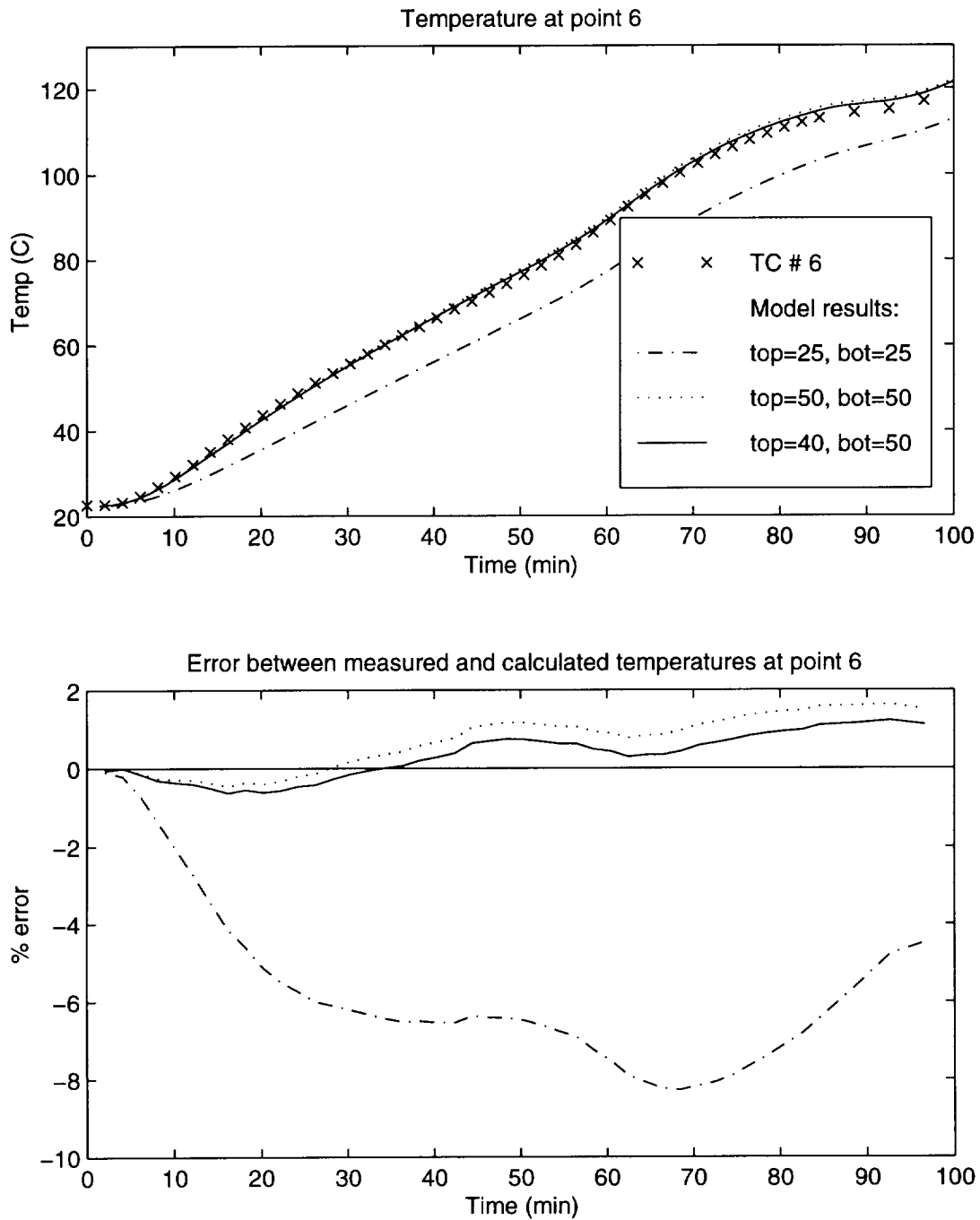


Figure 9.16: Temperature profiles at thermocouple location 6 for various convective coefficients. Thermocouple locations are shown in Figure 9.3.

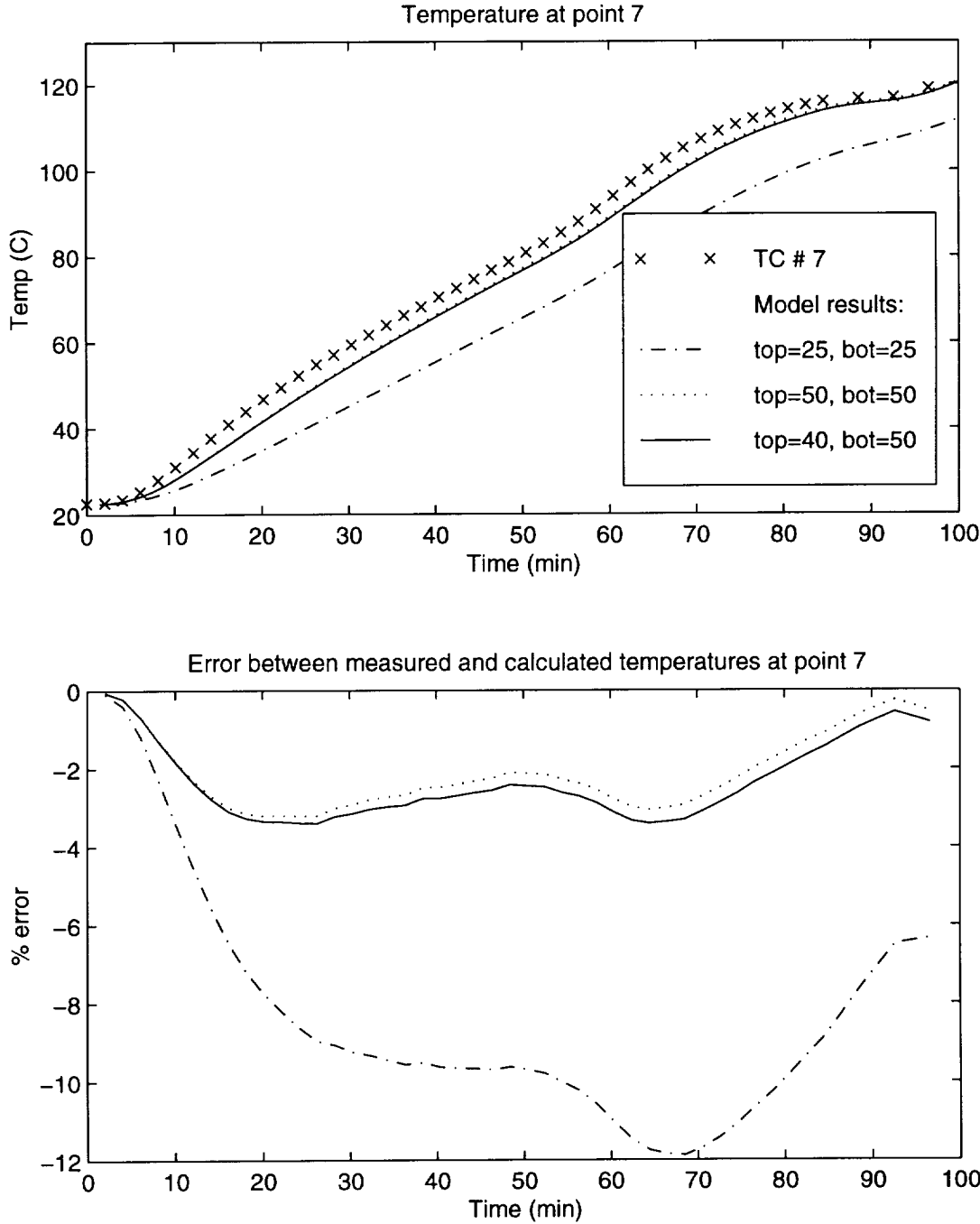


Figure 9.17: Temperature profiles at thermocouple location 7 for various convective coefficients. Thermocouple locations are shown in Figure 9.3.

9.3 Results

Figures 9.18–9.23 show the predicted and measured temperatures at six locations on the preform. Thermal errors were calculated as stated in Equation (9.1) on page 99. Figure 9.24 shows the predicted and measured wet out times for each step.

9.4 Discussion

9.4.1 Temperatures

Temperature results compare favorably between the model and the experiment. During the infiltration of the preform (before 50 minutes) the predicted temperatures are within 3–4% of the measured temperatures. There are a few interesting points to note. If you look at the temperatures from the start of the experiment to about 20 minutes, the model is seen to overpredict at every point. This is caused by the presence of the bleeder cloth in the experiment. The bleeder will act like a blanket and slow the initial penetration of the autoclave heat into the part. The thermal effects of the bleeder were not included in the model, so the model begins to see the autoclave temperatures sooner than the real part. After the initial lag time, the experimental and predicted temperatures begin to converge.

The highest error is found at thermocouple location 5 (see Figure 9.21). Both models show a significant thermal overshoot as compared to the experiment. Point 5 is under the two stack step, the thinnest step. As was noted in Chapter 7, this thermal overshoot is usually caused by a mesh that is too coarse. This is very likely here, as this step is modeled by only two elements through its thickness. If a finer mesh had been used in this step, the thermal overshoot would likely be either smaller or non-existent.

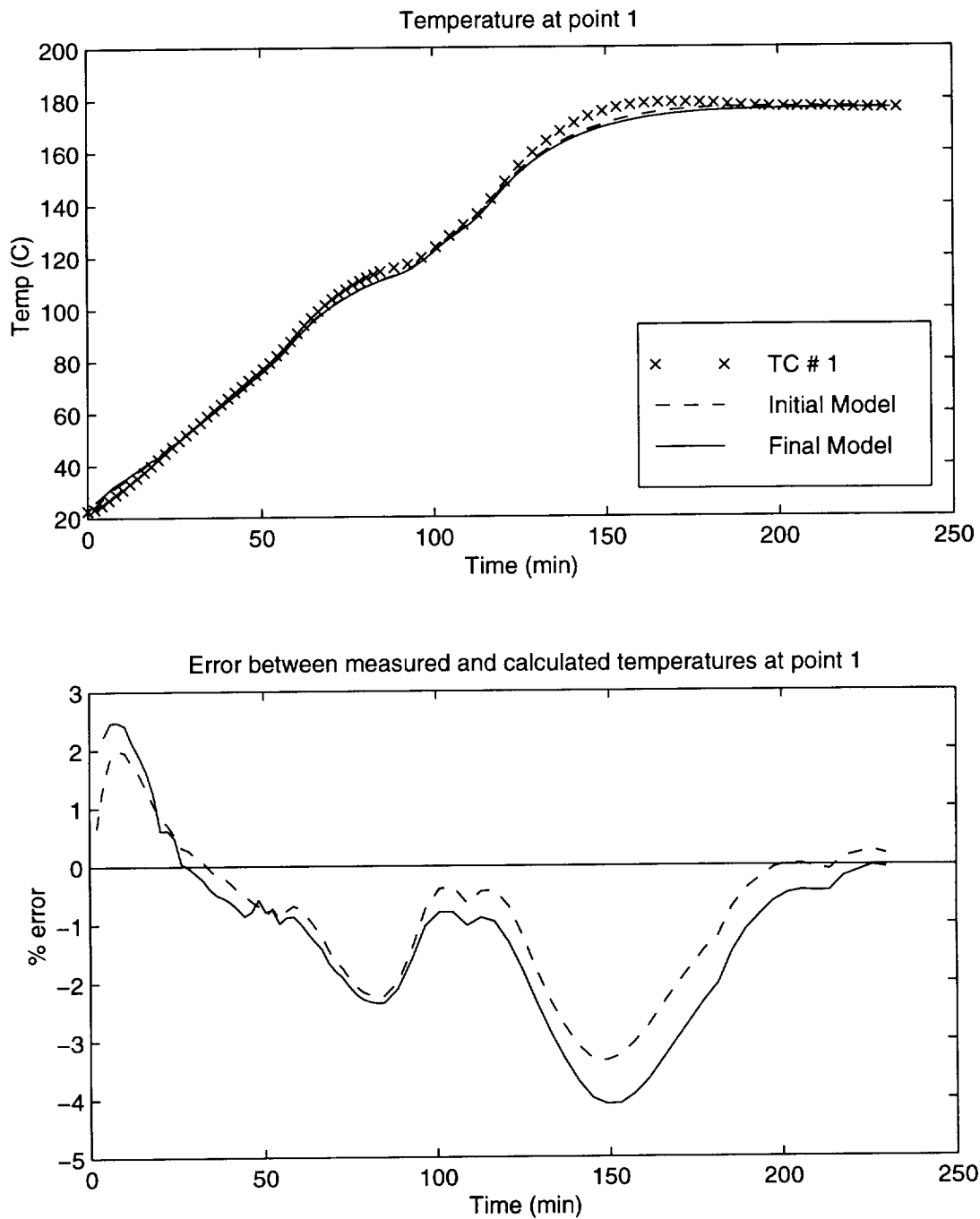


Figure 9.18: Comparison of thermal profiles at point 1. Thermocouple locations are shown in Figure 9.3.

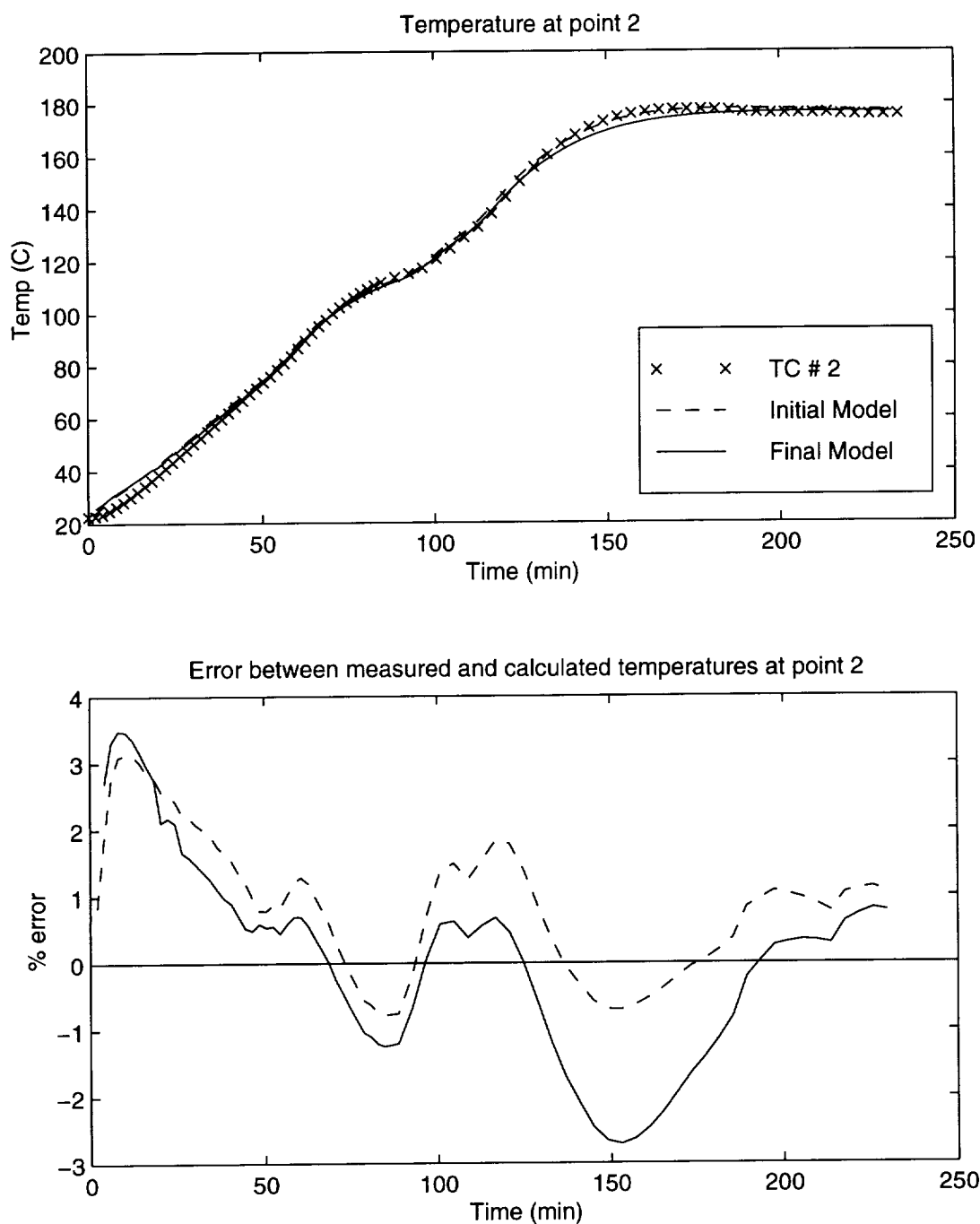


Figure 9.19: Comparison of thermal profiles at point 2. Thermocouple locations are shown in Figure 9.3.

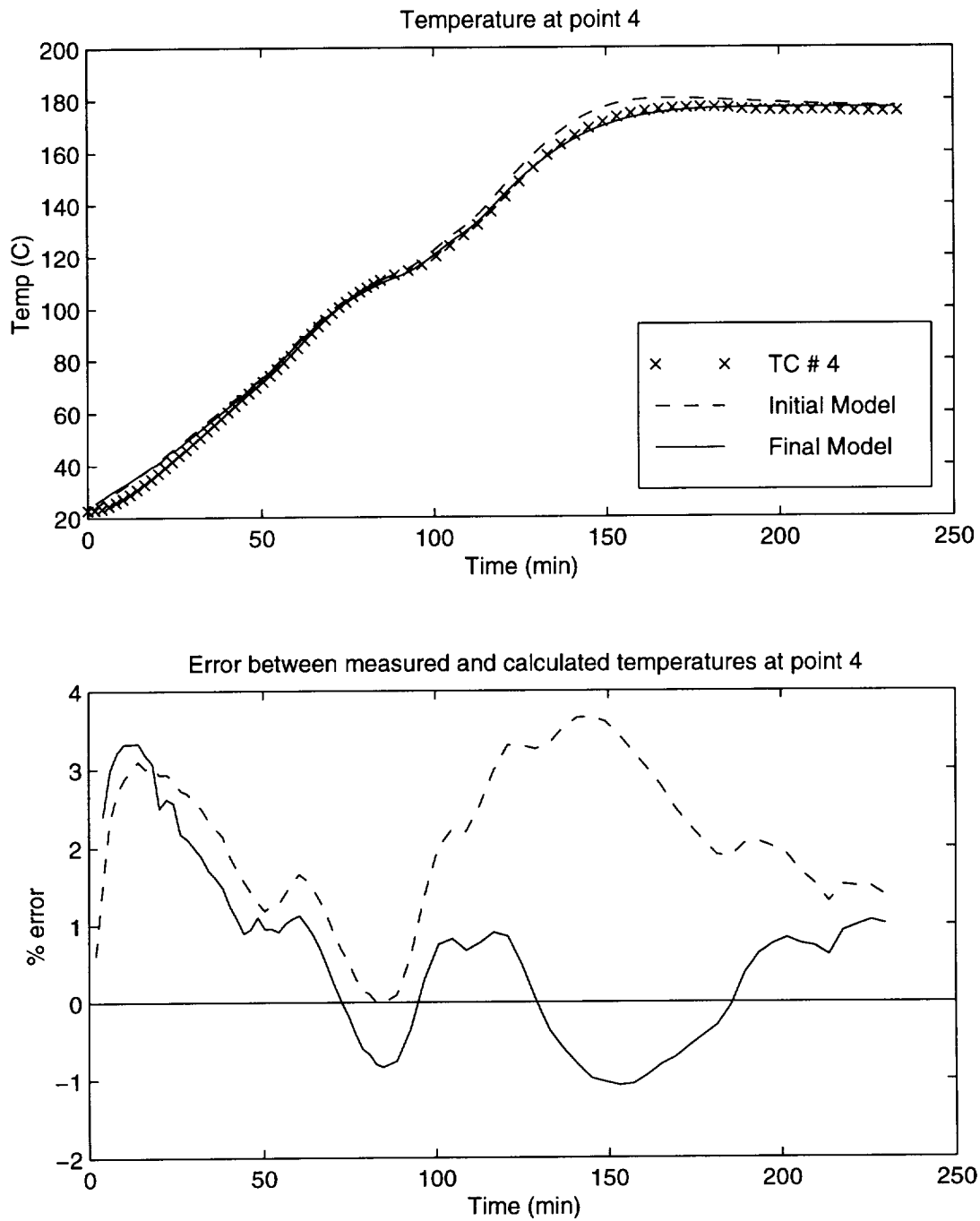


Figure 9.20: Comparison of thermal profiles at point 4. Thermocouple locations are shown in Figure 9.3.

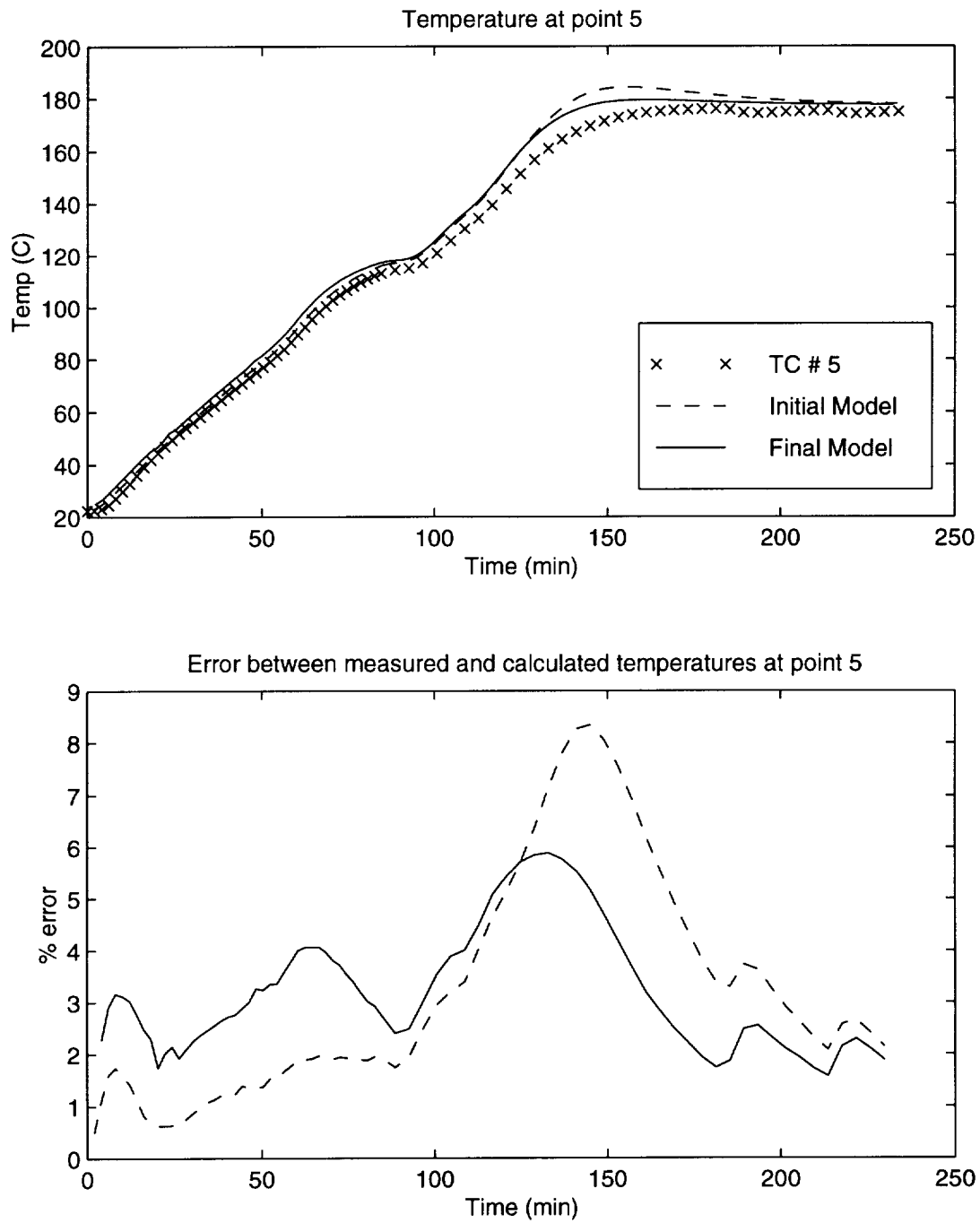


Figure 9.21: Comparison of thermal profiles at point 5. Thermocouple locations are shown in Figure 9.3.

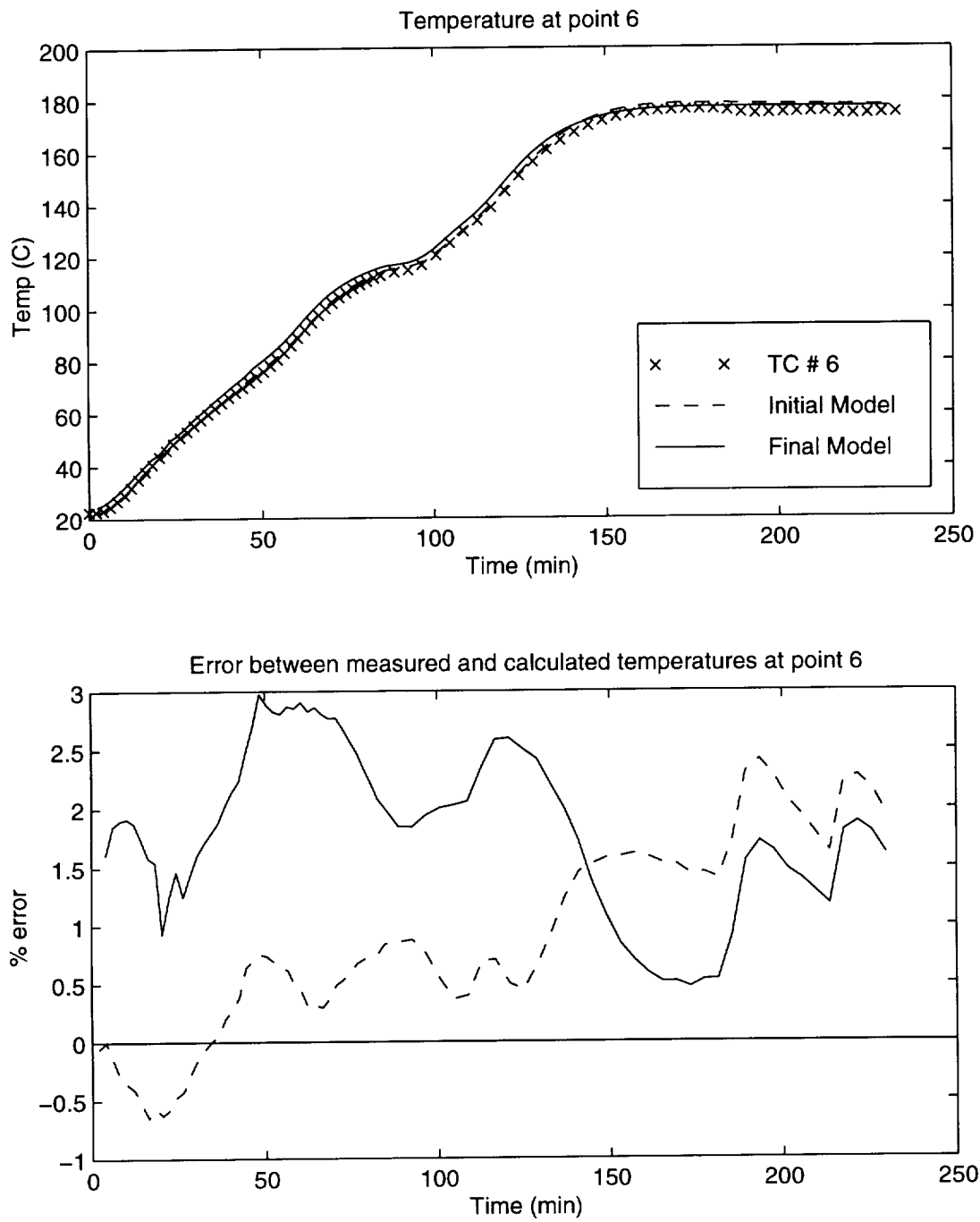


Figure 9.22: Comparison of thermal profiles at point 6. Thermocouple locations are shown in Figure 9.3.

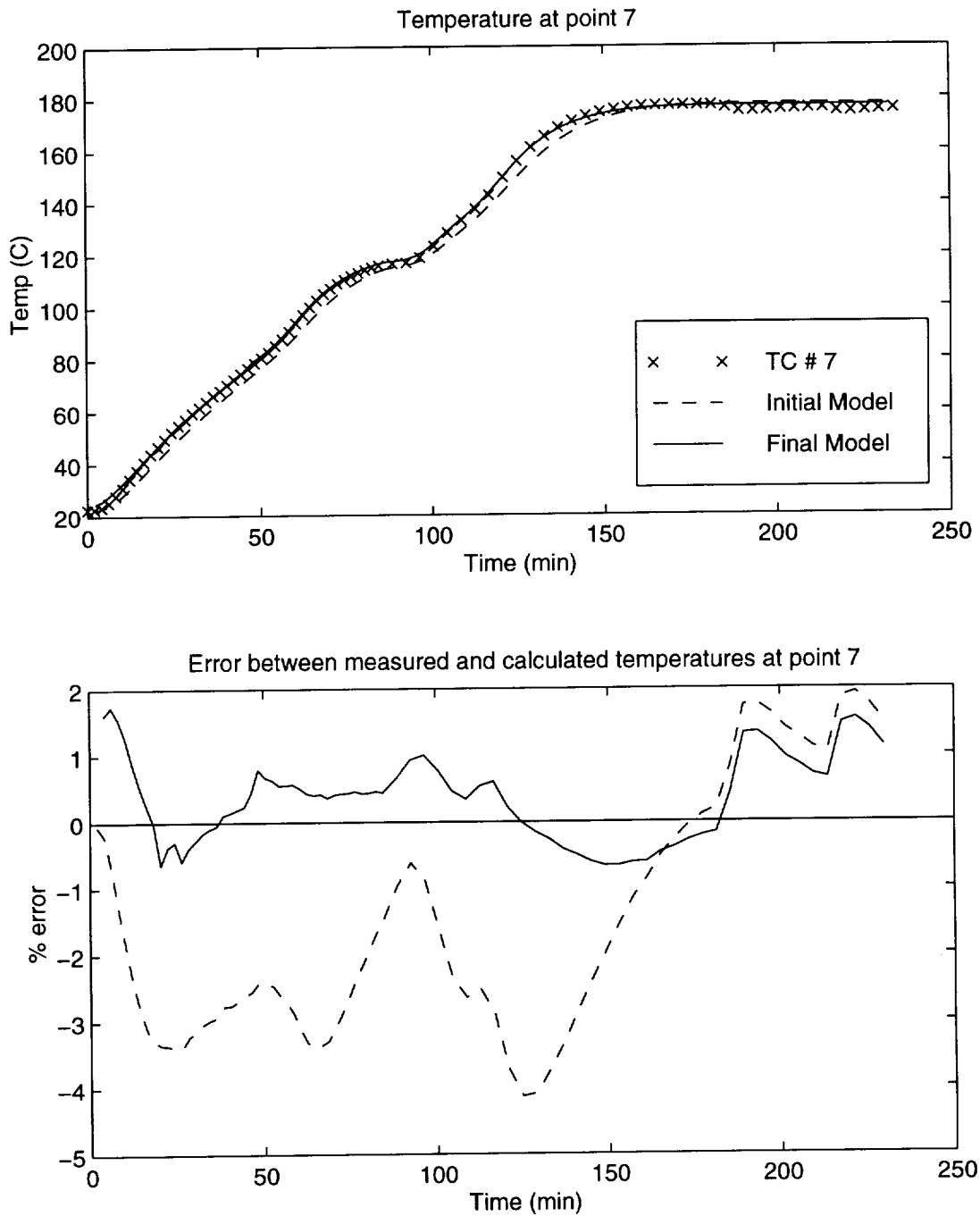


Figure 9.23: Comparison of thermal profiles at point 7. Thermocouple locations are shown in Figure 9.3.

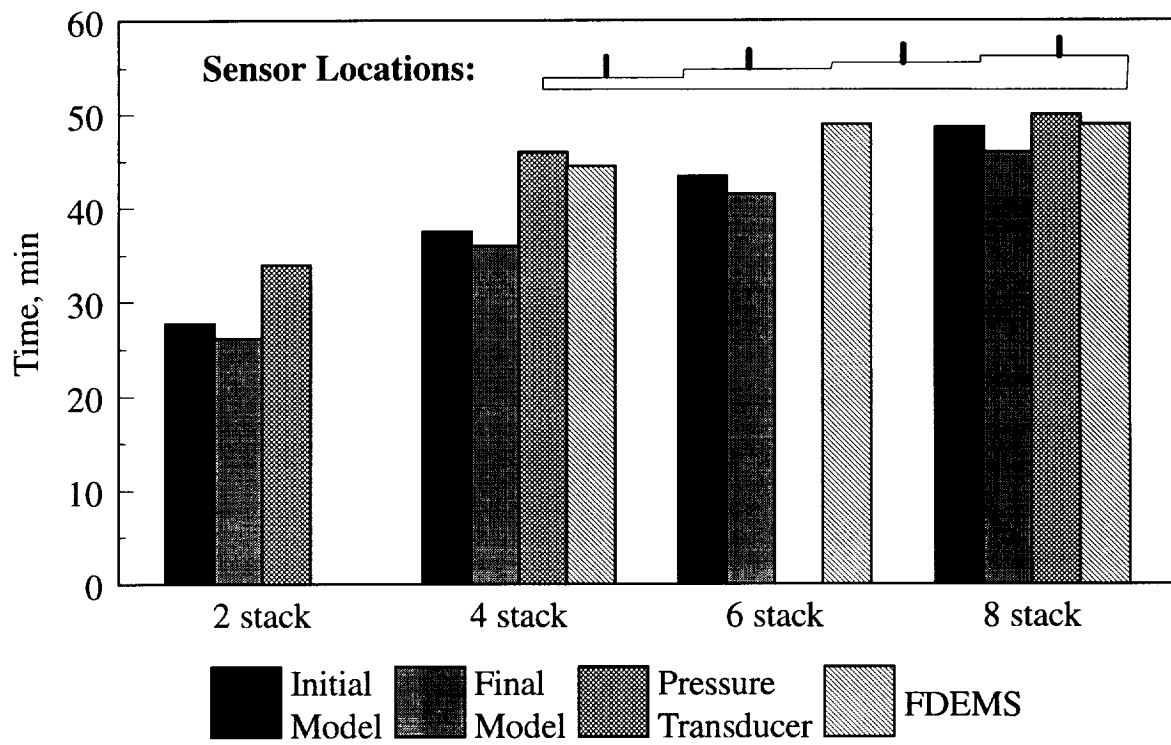


Figure 9.24: Comparison of predicted and measured infiltration times for the stepped panel.

9.4.2 Fill Times

Fill times do not agree as well as the temperatures did. The model predicts earlier wet out than the experiment for all the steps. The percentage difference between the predicted and measured fill times are: 2 stack, -23% ; 4 stack, -22% ; 6 stack, -15% ; 8 stack, -9% . The general trend here is that as the steps get thicker, the difference between the predicted and measured wet out times decreases. One explanation for this is that the filling of the thin steps is dominated by flow at low temperatures. The kinetics model is based on data at temperatures greater than 60°C , and viscosities for temperatures lower than that are extrapolated from the viscosity model. The 2 and 4 stack sections fill while the highest temperature in the model is about 50°C . This indicates that the viscosity model tends to underpredict the viscosity for low temperatures.

The measured wet out times for the 6 and 8 stack steps were identical. This seems to indicate that after the 4 stack step was filled, the resin may have leaked between the top tooling plate and the preform, resulting in early wet out times for the 6 and 8 stack steps.

9.5 Conclusions

Given the correct heat transfer coefficients, the model is able to match the measured temperatures in the experiment. Finding these convective coefficients will be necessary before the model can be used in predictive work.

The fill times matched better for the thicker sections than the thinner sections. This was probably due to the inaccuracy of the viscosity model below 60°C . As the flow through the preform was dominated by flow at warmer temperatures, the viscosity model moved into the range of temperatures it was based on, and the viscosity results were more accurate.

Chapter 10

Two Stiffener Panel

A panel with two stiffeners was manufactured using the RFI process. A two stiffener panel was chosen because the complex shape will introduce a three-dimensional flow pattern. The process was simulated using 3DINFIL and the simulation results are compared to the experimental results. The objective of the test was to verify the flow, cure, and thermal models in a complex shaped RFI part.

10.1 Experiment

10.1.1 Preform and Tooling

The preform skin was constructed of eight stacks of the warp knit fabric and the blades were constructed from the 14 tube braided material described in Chapter 6. Sketches of the preform are shown in Figure 7.2 on page 46 and Figure 10.1.

The mold for this part was constructed from 6061-T6 aluminum. A sketch of the tooling is shown in Figure 10.2. The base plate was approximately 121.92 cm long by 60.96 cm

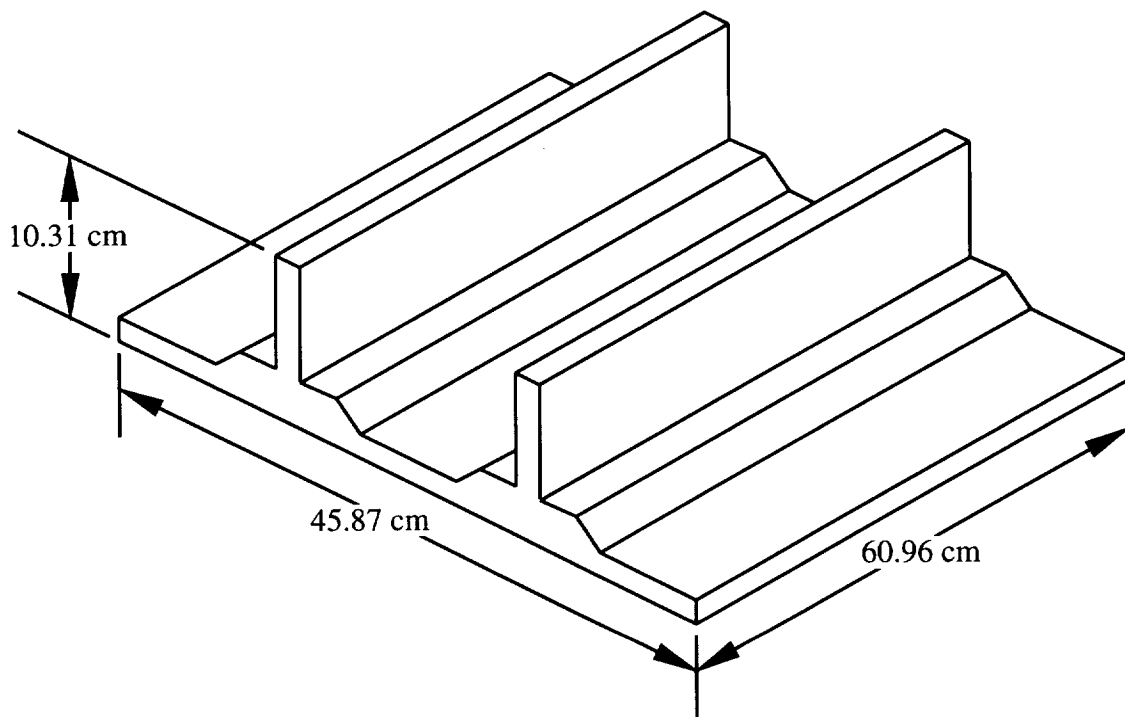


Figure 10.1: Sketch of the two stiffener preform.

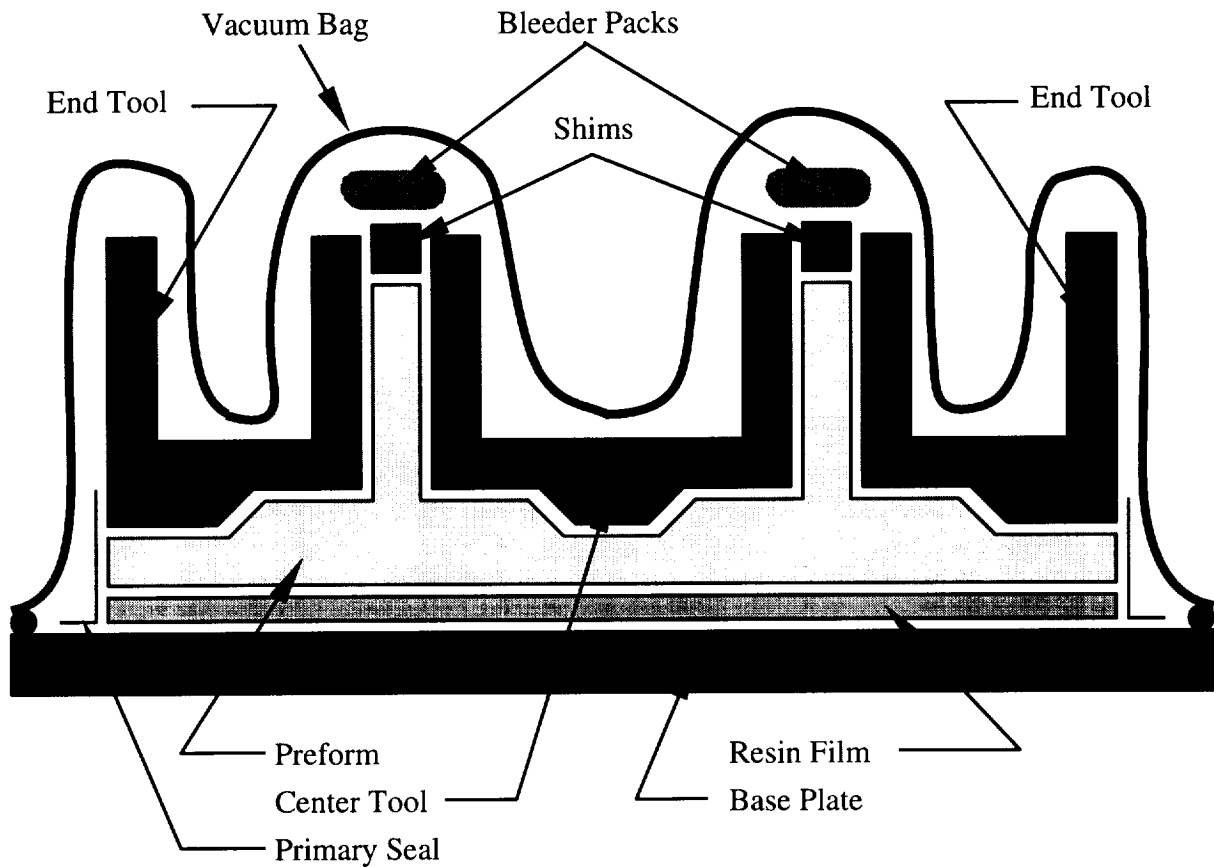


Figure 10.2: Tooling used to infiltrate the two stiffener panel.

wide by 1.27 cm thick. The thickness of the upper mold components varied from about 1.4 to 2.3 cm. Detailed schematic diagrams of the tooling can be found in Appendix A.

Mounted in the molds were four Entran flush mount pressure transducers, model EPX0-X03-150P and three FDEM sensors. Nine thermocouples were mounted in and around the panel. Thermocouples 2 and 4 were mounted between the resin film and the base plate, and thermocouple 5 was mounted between the skin and the center tool. The locations of the sensors are shown in Figures 10.3–10.5. The remaining six thermocouples were mounted in the autoclave air about 5 cm away from the assembly as shown in Figure 10.6.

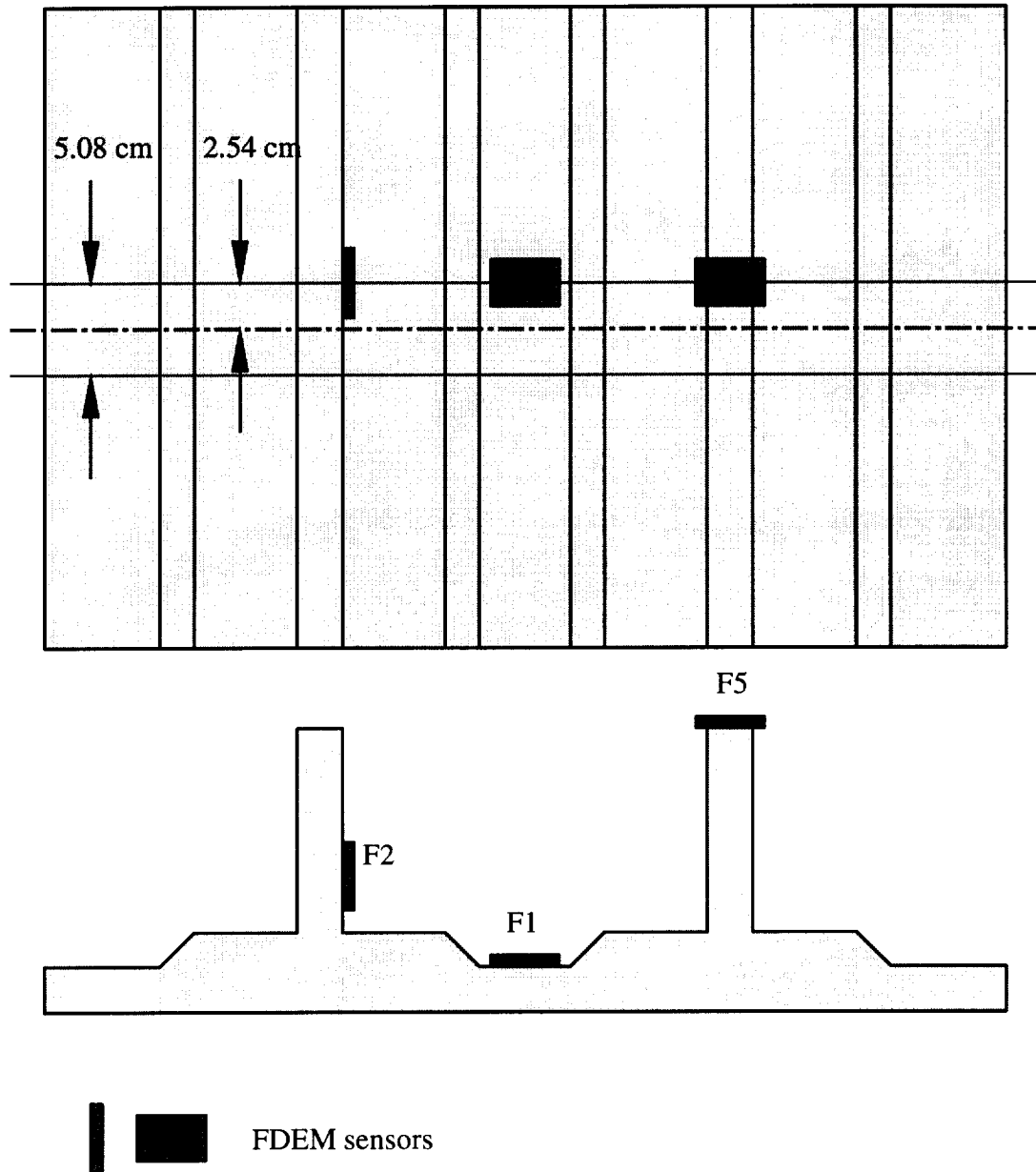


Figure 10.3: Locations of the FDEM sensors on the two stiffener panel.

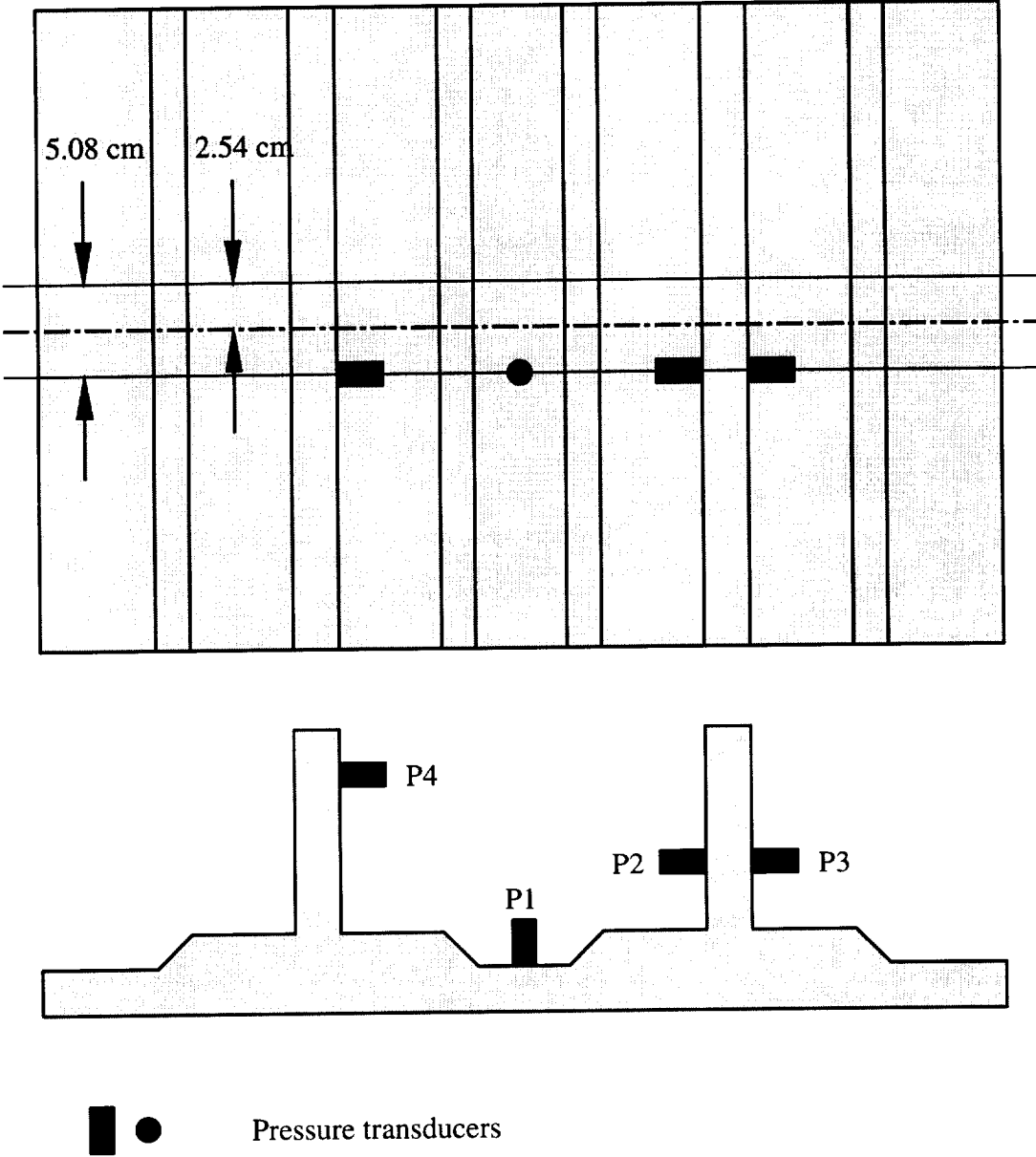


Figure 10.4: Locations of the pressure transducers on the two stiffener panel.

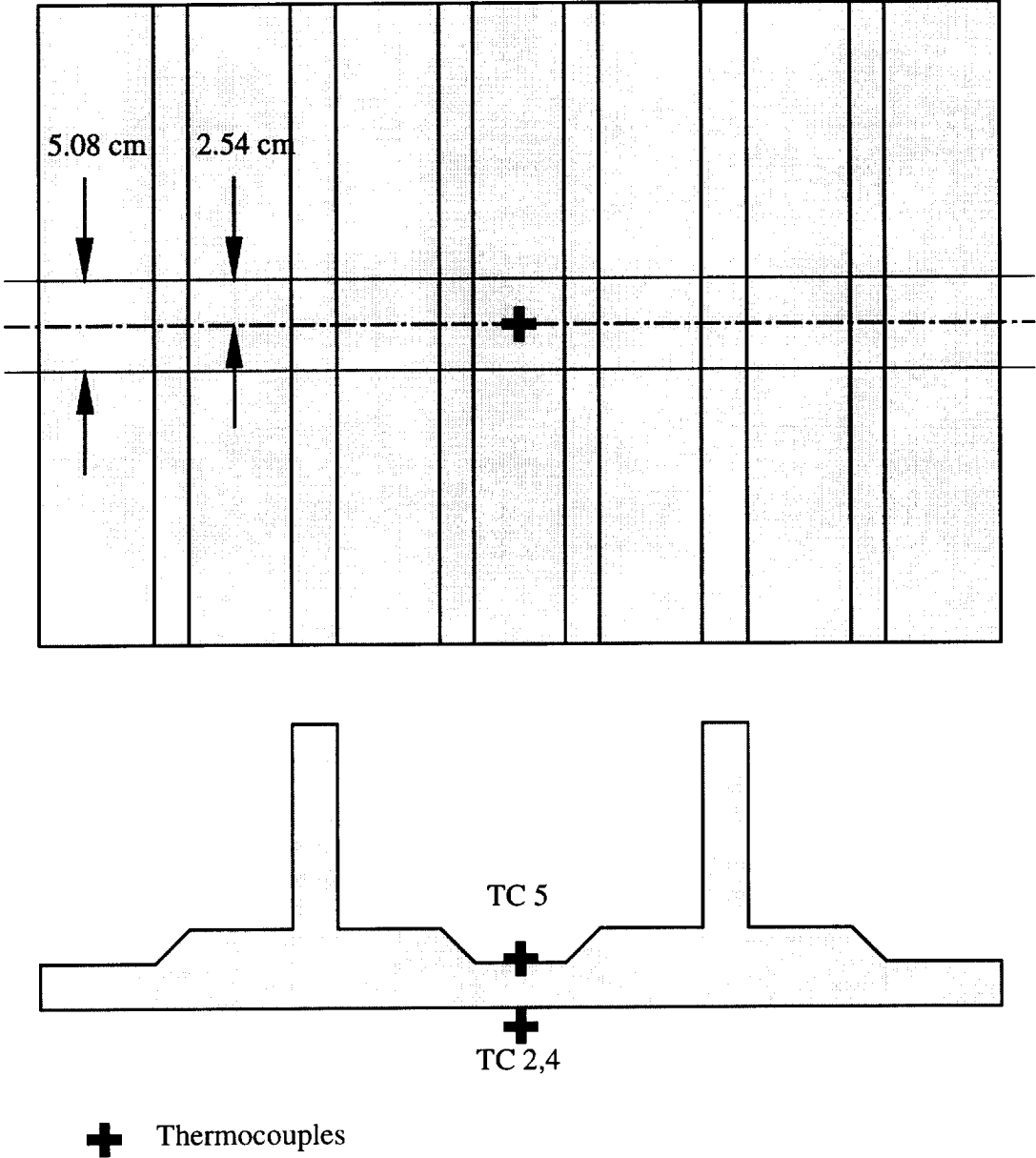
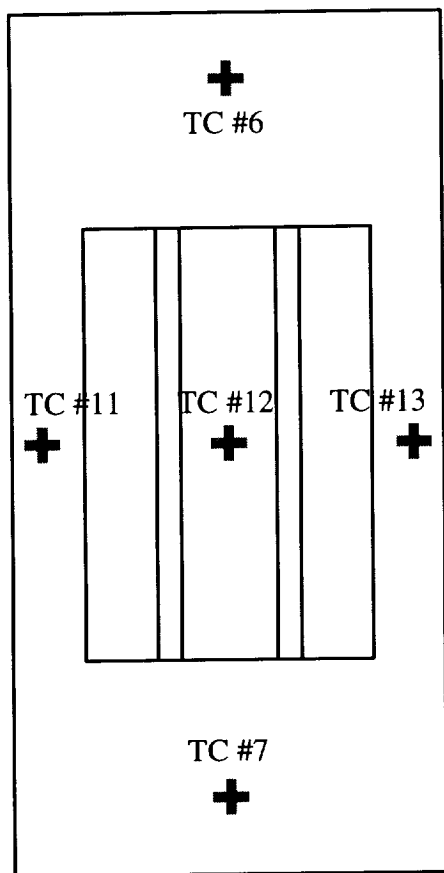
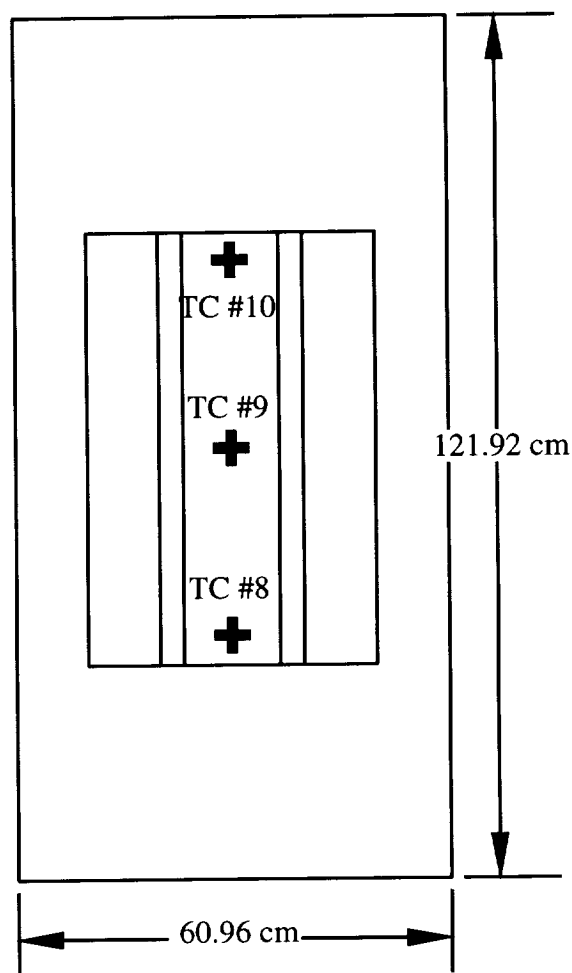


Figure 10.5: Locations of the thermocouples on the two stiffener panel.

Thermocouples under the base plate.



Thermocouples above the mold.



Autoclave Door

Figure 10.6: Locations of the thermocouples mounted beneath the base plate and above the surface of the top tooling components.

Table 10.1: Size and Run Time of the Models.

Model	Flow Model		Thermal Model		CPU Time
	Nodes	Elements	Nodes	Elements	
Initial	1008	434	2112	970	3.8 min
Final	8995	7276	17325	14994	77.8 hr

10.1.2 Procedure

The panel was laid up following the same procedure as the stepped panel in Chapter 9.

10.2 Simulation Model

Following the same procedure used for the stepped panel, two models were built of the two stiffener panel. The initial model was one element thick in the Z-direction, and the final model was a fully three-dimensional model.

10.2.1 Geometry and Mesh

The dimensions of the model were defined by the tools. The only dimension not defined by the tools was the cured thickness of the skin, which was taken to be 12.19 mm. The meshes used are shown in Figures 10.7 and 10.8. Table 10.1 lists the number of nodes and run times of the two models.

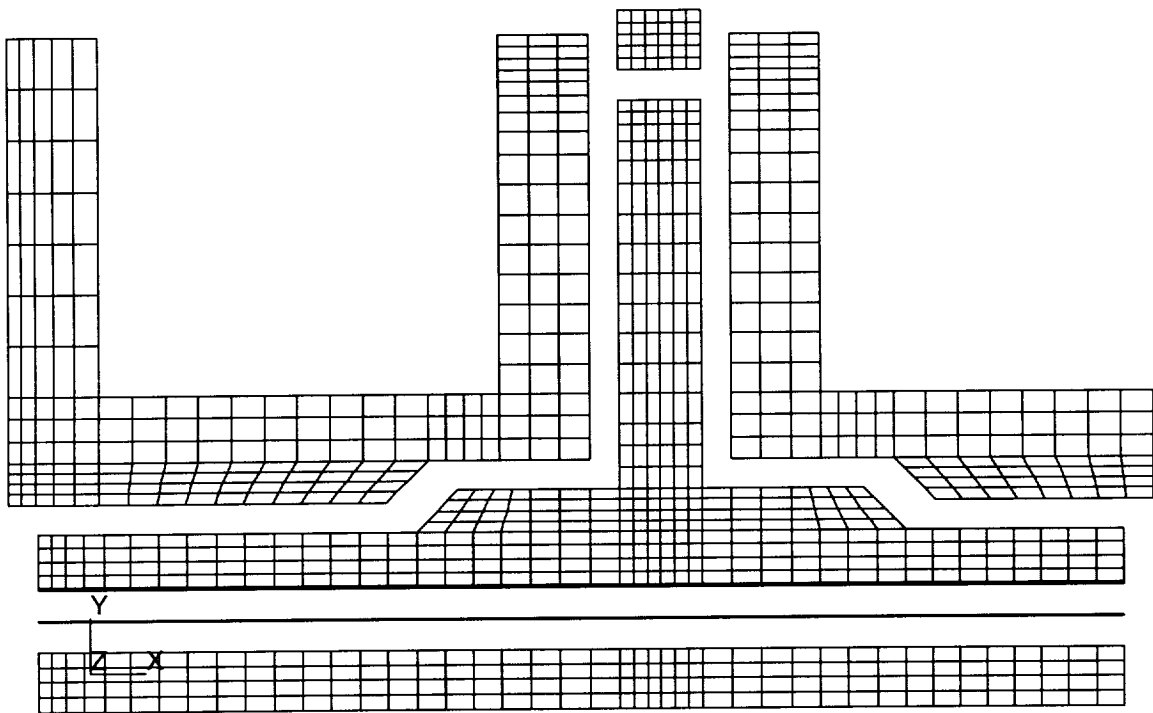


Figure 10.7: Mesh used in the initial model of the two stiffener panel. The model is one element thick in the Z direction.

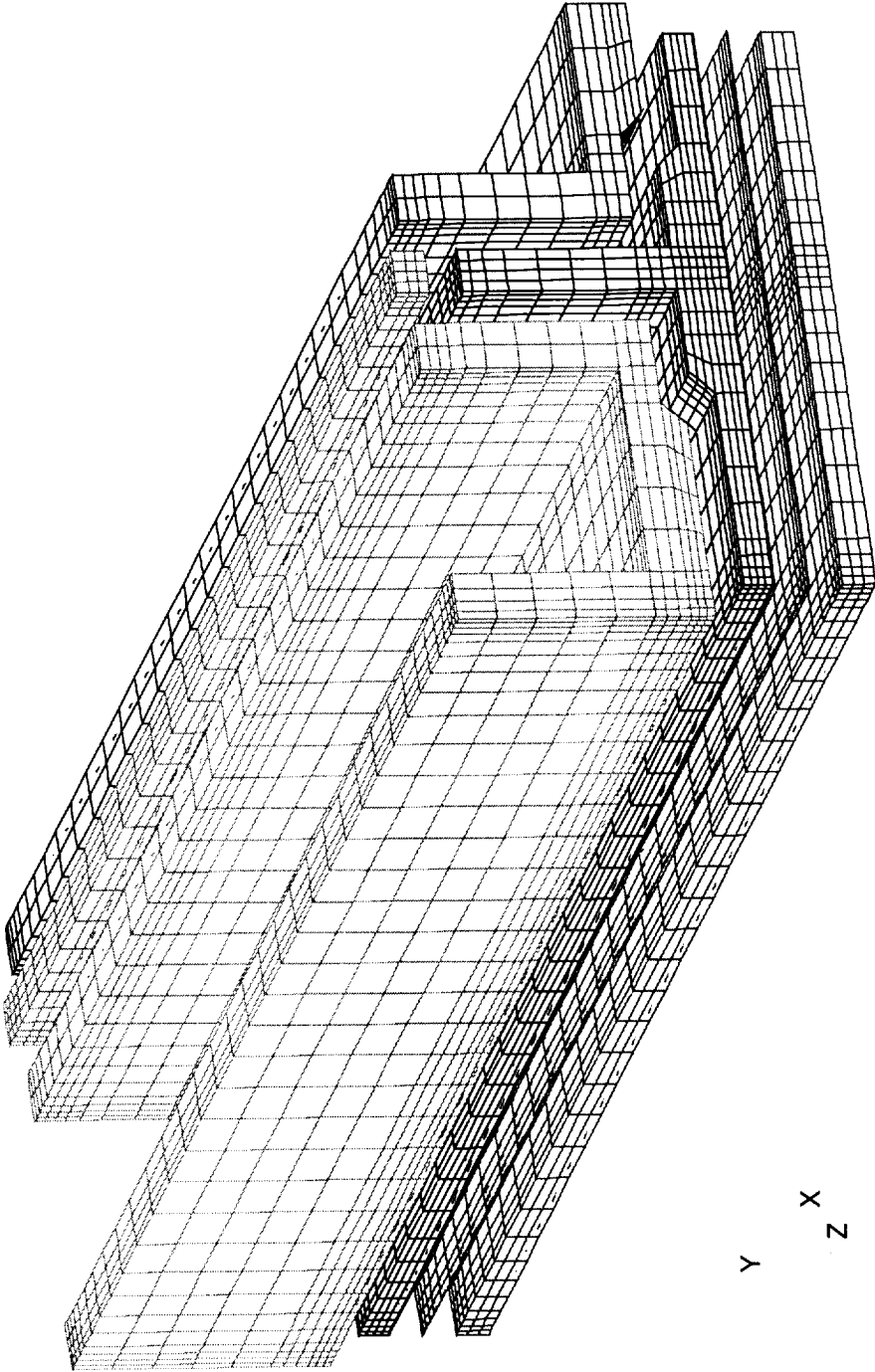


Figure 10.8: Mesh used in the final model of the two stiffener panel.

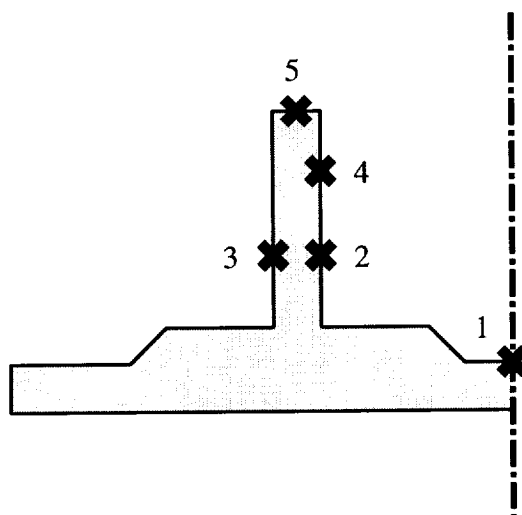


Figure 10.9: Sensor locations in the finite element model.

Both models used the half symmetry present in the setup to reduce the size of the models. The sensors in the actual part were distributed between the two stiffeners, but the model only has one stiffener. Since it was assumed that the process would be symmetric between the two stiffeners, the sensors locations in the model were numbered as shown in Figure 10.9. Table 10.2 shows the correspondence between the locations in the model and the physical sensors (see Figures 10.3 and 10.4).

Table 10.2: Correspondence between the locations in the finite element model and the physical sensors.

Model Location	Pressure Transducer	FDEMS
1	1	1
2	2	2
3	3	n/a
4	4	n/a
5	n/a	5

10.2.2 Boundary Conditions

The autoclave pressure was applied to the lower surface of the skin. The pressure started at 1 Pa and ramped to 827 kPa in 10 minutes, then held constant for the duration of the process.

The measured autoclave temperatures are shown in Figure 10.10. It should be noted that thermocouple 8 recorded a much lower air temperature than the other thermocouples. One of the heating coils in the autoclave did not work, and thermocouple 8 was nearest the cooler area.

The thermal model had convective boundary conditions applied to the surfaces of the model. Different convective coefficients and temperature cycles were applied to different parts of the model. The one element thick model used convective coefficients of 25 and 30 $\text{W}/\text{m}^2\cdot^{\circ}\text{C}$ and used autoclave air temperature data as shown in Figure 10.11.

Convective coefficients for the final model were 30 $\text{W}/\text{m}^2\cdot^{\circ}\text{C}$ on the top of the model and 25 $\text{W}/\text{m}^2\cdot^{\circ}\text{C}$ on the bottom. Six different thermal boundary conditions were applied to the model. The model was divided into thirds and the measured autoclave temperatures were applied as shown in Figure 10.12. No convective coefficients were applied on the plane of symmetry.

10.2.3 Materials

There were three preform materials used in the flow model, one each for the blade, the skin, and the flange regions. The permeabilities of the skin and flange regions were calculated at the full autoclave pressure using the constants in Appendix B. Because the blade thickness was controlled by the thickness of the shim, the fiber volume fraction of the blade was

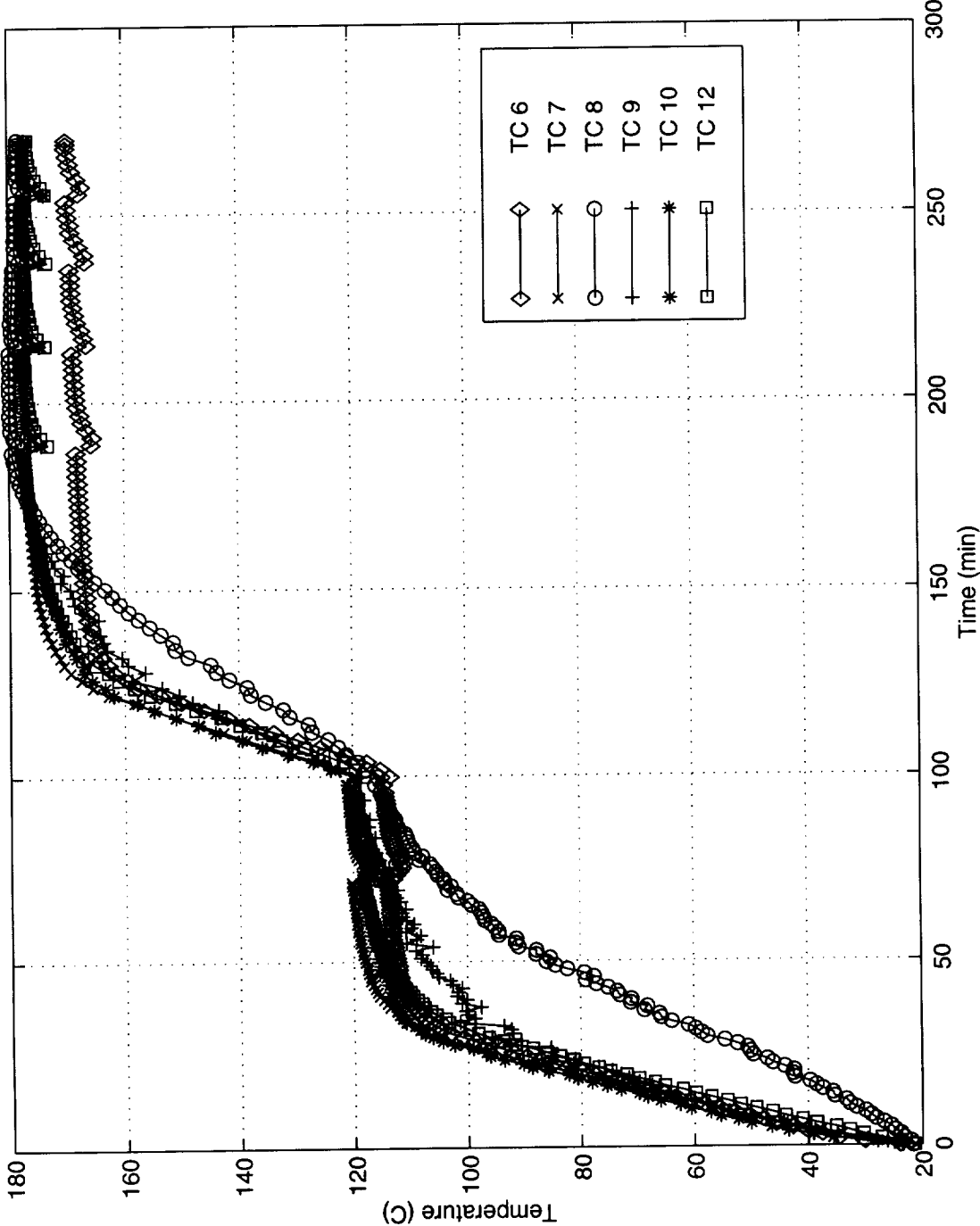


Figure 10.10: Measured autoclave temperatures used in the two stiffener model.

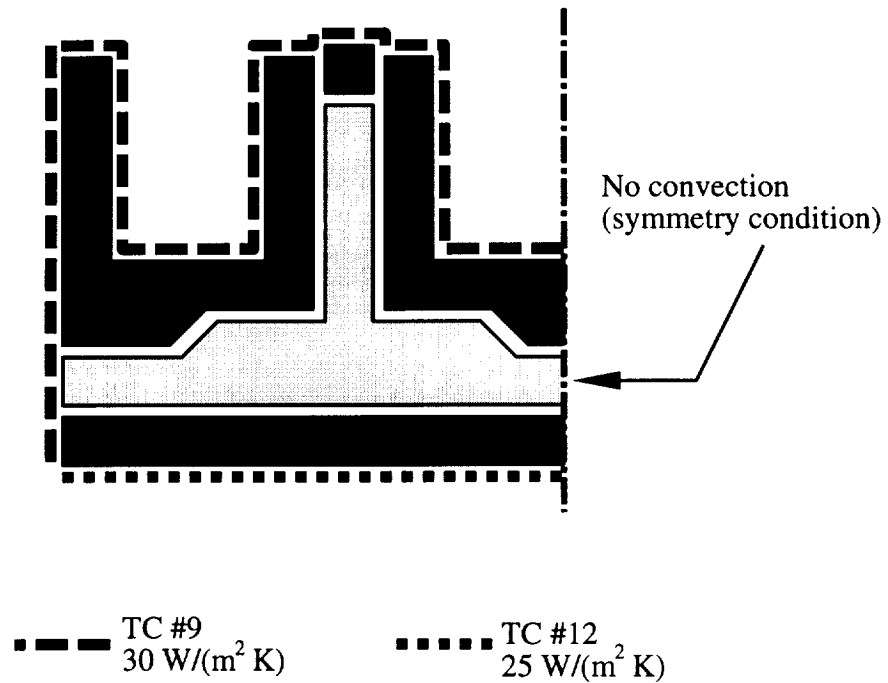


Figure 10.11: Convective boundary conditions on the initial model.

calculated using the following information:

$$v_f = \frac{A_w N}{\rho_f t} = 0.585 \quad (10.1)$$

where

$$\begin{aligned}
 A_w &= .1286 \text{ g/cm}^2/\text{per stack} \\
 N &= 14 \text{ stacks} \\
 \rho_f &= 1.8 \text{ g/cm}^3 \\
 t &= 0.672 \text{ cm}
 \end{aligned}$$

Here A_w is the areal weight per tube of fabric, N is the number of tubes, ρ_f is the density of the fiber, and t is the thickness of the blade. The thickness of the blade is determined by the dimension of the shim.

Based on these calculated fiber volume fractions, the permeabilities of each region were calculated. The permeabilities used are shown in Table 10.3. They were applied as shown in Figure 10.13. The thermal properties used are those listed in Appendix B.

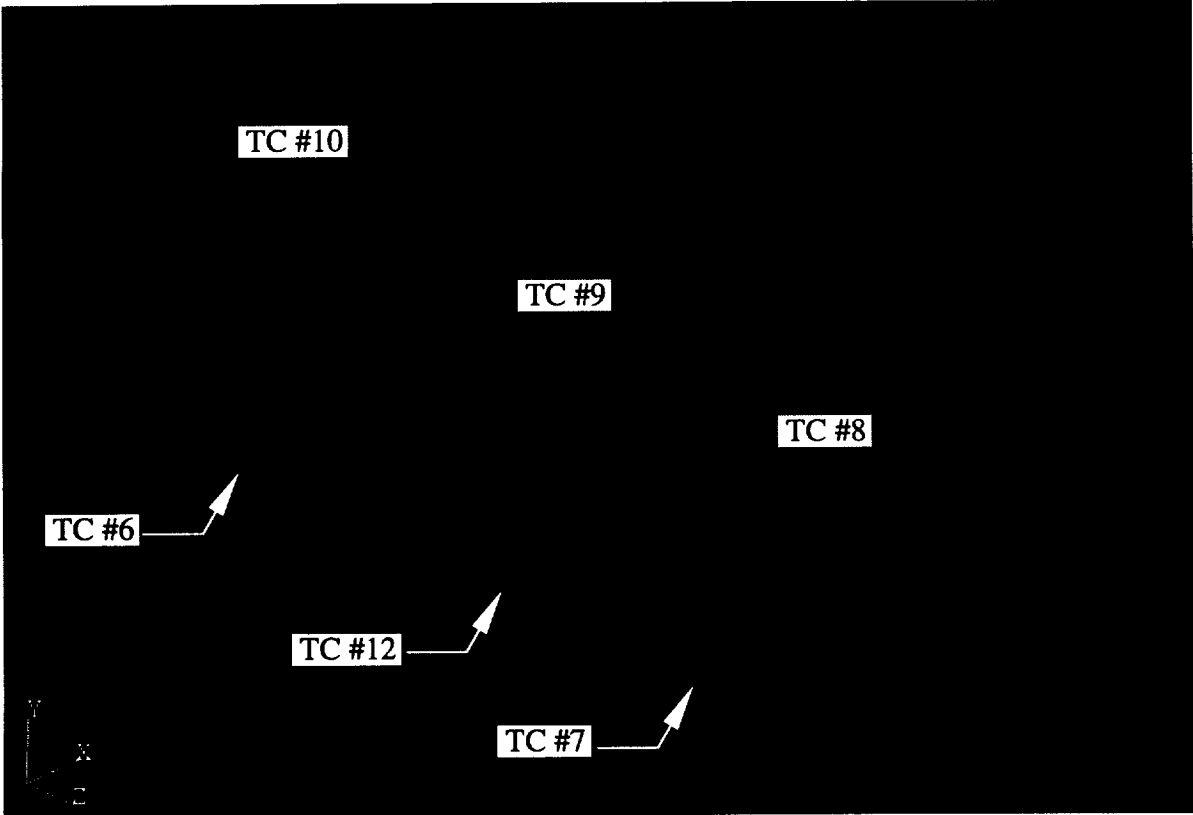


Figure 10.12: Convective boundary conditions on the final model.

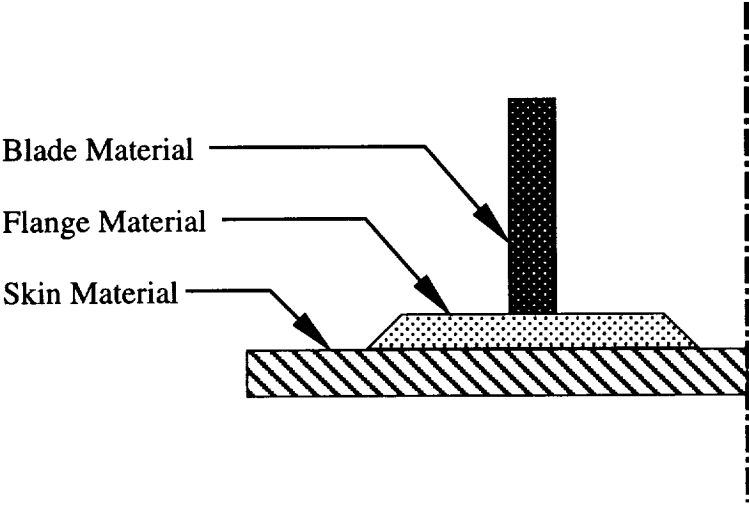


Figure 10.13: Materials in the two stiffener panel.

Table 10.3: Permeabilities applied to the two stiffener model.

Material	Permeability m^2
Skin: Warp Knit 63.9% FVF	
IPP (S_{zz})	2.129×10^{-12}
IPN (S_{xx})	9.020×10^{-13}
TTT (S_{yy})	4.456×10^{-13}
Flange: 4 Tube Braid 64.5% FVF	
IPP (S_{zz})	2.855×10^{-12}
IPN (S_{yy})	1.039×10^{-12}
TTT (S_{xx})	2.591×10^{-13}
Blade: 14 Tube Braid 58.5% FVF	
IPP (S_{zz})	8.419×10^{-12}
IPN (S_{yy})	5.372×10^{-12}
TTT (S_{xx})	5.983×10^{-13} *

* No 14 tube data available, computed using 4 tube TTT fit.

10.3 Results

The predicted flow front progressions are shown in Figures 10.14 and 10.15. Measured and predicted temperature profiles are shown in Figures 10.16 and 10.17. Finally, wet out times are shown in Figure 10.18.

10.4 Discussion

10.4.1 Temperatures

Predicted and measured temperatures matched within $\pm 6\%$ for both the initial and final models. It is shown in Figure 10.16 that the model initially overpredicts, then underpredicts the temperatures at points 2 & 4. This is most likely due to the presence of the breather

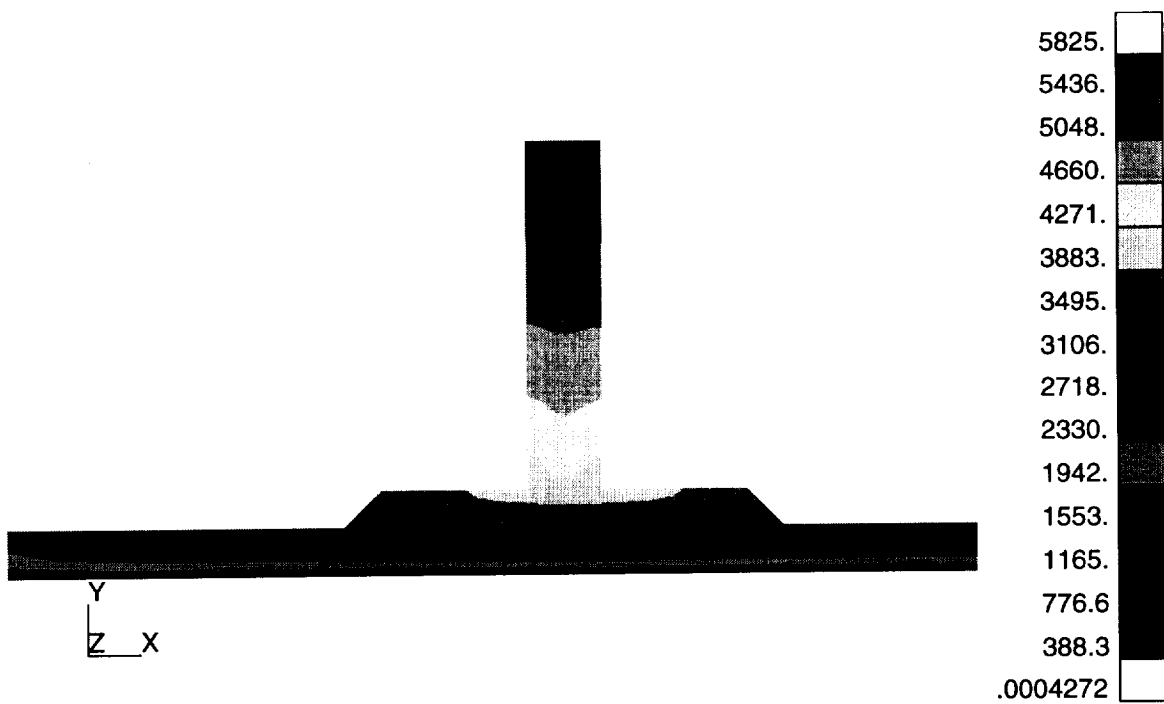


Figure 10.14: Flow front progression in the initial model. The color bands represent the flow front location at different times. The units are in seconds.

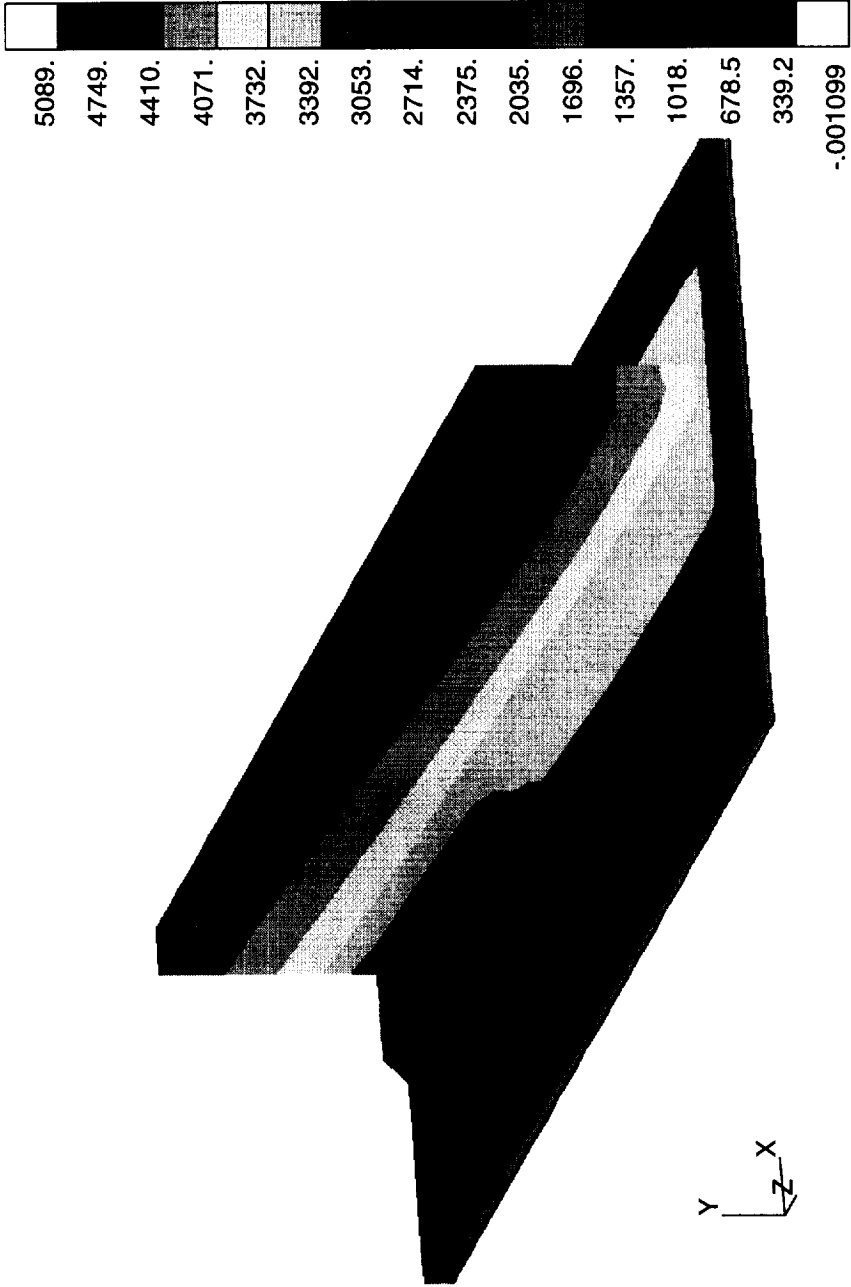


Figure 10.15: Flow front progression in the final model. The color bands represent the flow front location at different times. The units are in seconds.

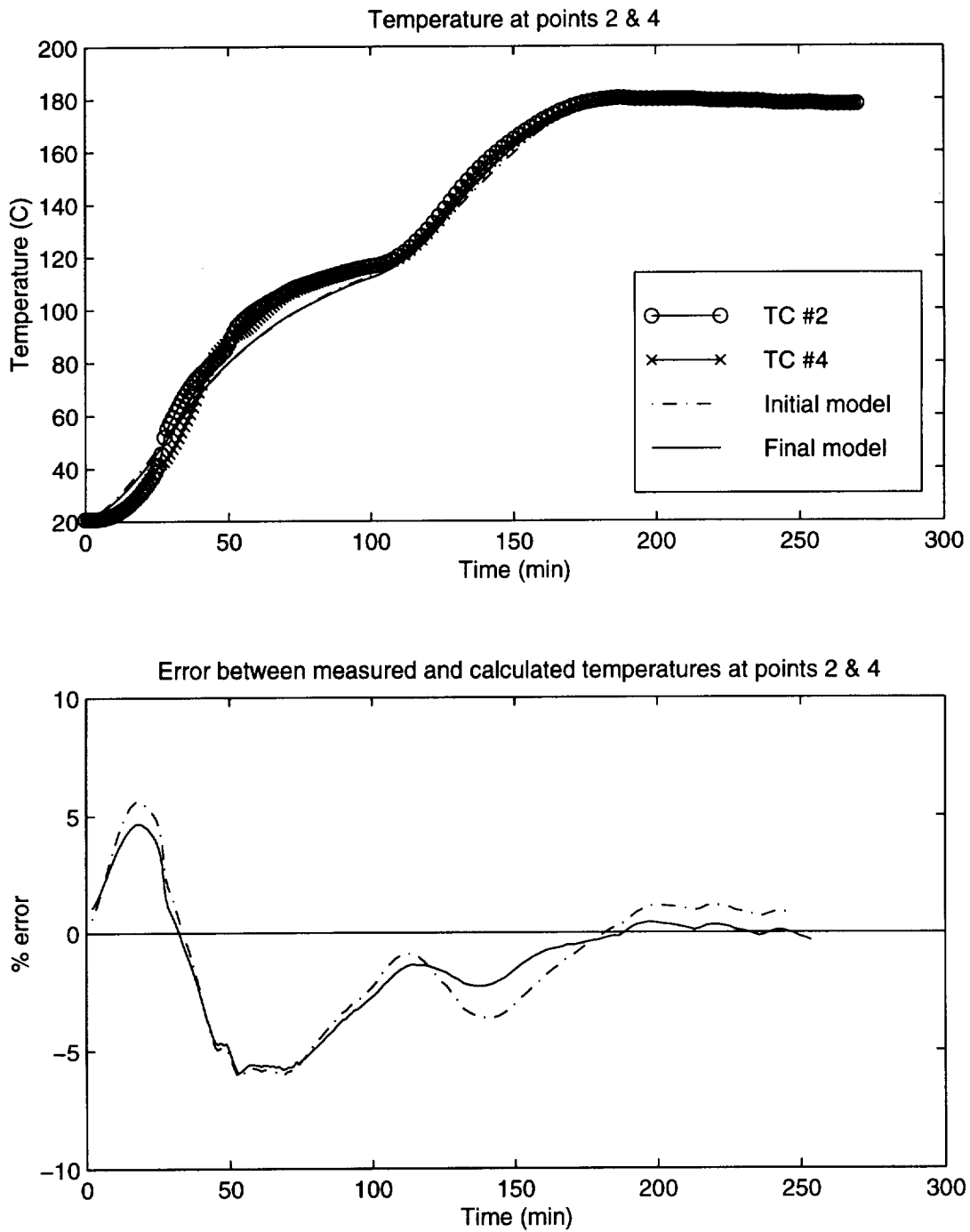


Figure 10.16: Measured and predicted temperatures at thermocouples 2 and 4. Thermocouple locations are shown in Figure 10.5.

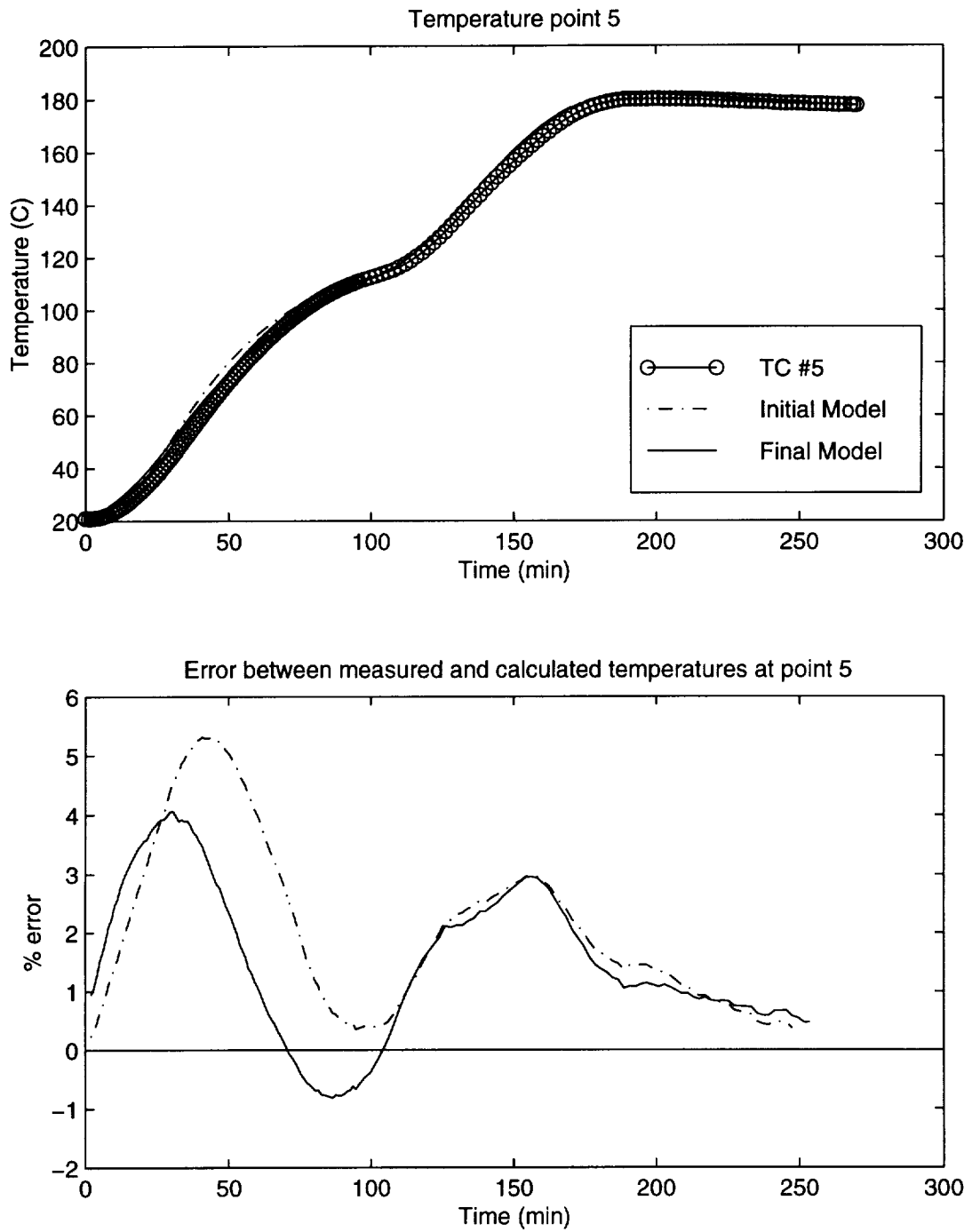


Figure 10.17: Measured and predicted temperatures at thermocouple 5. Thermocouple locations are shown in Figure 10.5.

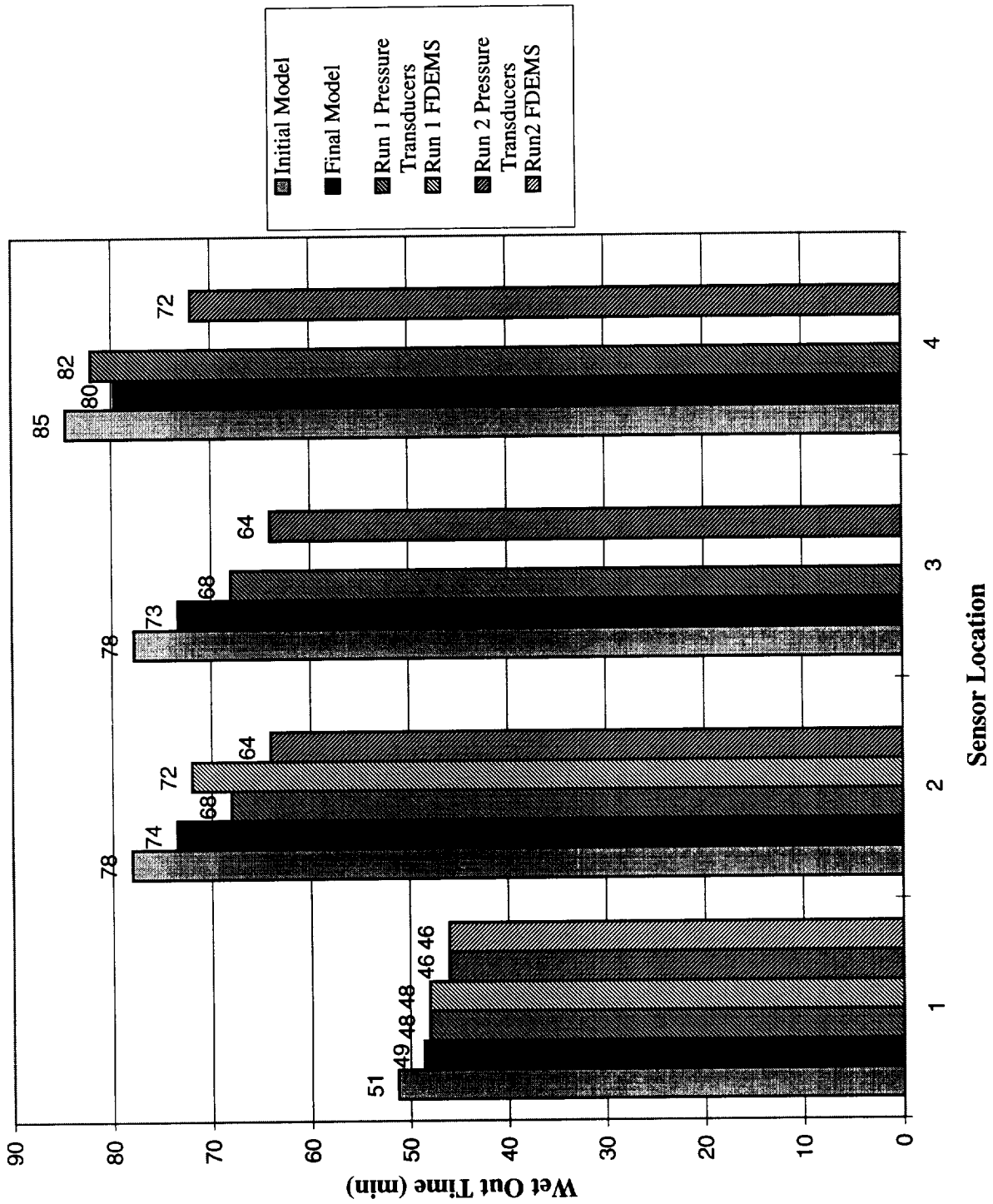


Figure 10.18: Predicted and measured infiltration times for the two stiffener panel.

material placed over the surface of the part when it was autoclaved. The breather material is a glass fiber cloth that has low thermal conductivity. Since the breather was not included in the model, it may be a source of error.

10.4.2 Fill Times

Figure 10.18 shows the wet out times for the various sensor locations. In the second experimental run, the sensors wet out much sooner than the first run. Wet out times differ by as much as 14% between the two runs. There seems to be some inherent variability in the RFI process.

The model predictions were generally conservative in this case. All of the predicted wet out times were longer than the experimentally measured times. The final model tended to predict wet out sooner than the initial model. This is because of the more realistic boundary conditions applied to the fully three dimensional model. The initial model had only two temperature cycles applied (from TC #9 and #12). While this may have been representative of the center section that the initial model was supposed to model, conduction from the ends of the model was neglected. Due to conduction, the final model tended to be warmer overall than the initial model, therefore the final model would fill faster.

The closest match in wet out times was at location 4 where the prediction of the final model was within 4% of the average of the experiments. The wet out times of the other locations varied from 7% to 12%.

10.5 Conclusions

When the correct thermal boundary conditions are applied to the model, the predicted and experimental fill times agree well. The wet out times for the two experiments differed by as much as 13%. Predicted wet out times were generally conservative. The model overpredicted the wet out times by 7% to 12%.

Chapter 11

Conclusions and Future Work

11.1 Conclusions

This study has developed and verified a comprehensive three-dimensional RTM/RFI simulation model. The model can be used to simulate the processing of complex shaped composite structures including the flow of resin through a carbon fiber textile preform, heat transfer in the preform/tool assembly, and cure kinetics of the resin.

The formulation for the flow model is given using the finite element/control volume (FE/CV) technique based on Darcy's Law of creeping flow through a porous media. The FE/CV technique is a numerically efficient method for finding the flow front location and the fluid pressure. The heat transfer model is based on the three-dimensional, transient heat conduction equation, including heat generation. Boundary conditions include specified temperature and convection. The code was designed with a modular approach so the flow and/or the thermal module may be turned on or off as desired. Both models are solved sequentially in a quasi-steady state fashion.

A model was derived for the cure kinetics of the Hercules 3501-6 reduced catalyst resin.

Several experiments were performed and computer simulations of the experiments were run to verify the simulation model. Isothermal, non-reacting flow was simulated in a T-stiffened section, and non-isothermal, reactive flow was simulated in a stepped panel and a panel with two 'T' stiffeners. Flow front predicted times were generally within 5–15% of the measured times.

11.2 Future Work

Many of the necessary parameters needed by this model are not known with any degree of certainty. Parameters include the permeability of the preform and the batch to batch variability of this parameter, and the thermal conductivity of the preform material. The resin model also needs more study. The simulation model predicts resin flow at temperatures below 60°C, and experimental data supports this prediction. If flow in this range is to be modeled, the resin model must be extended to even lower temperatures. Before this simulation model can be used as a predictive tool, these inputs and their variation must be known.

To increase the utility of the code, it should be extended to include the compaction behavior of the preform. This will allow the permeability of the preform to change and more accurately reflect the actual processing conditions. This will increase the computational resources. An important area of work will be finding either more efficient algorithms to solve the problem, or adapting the current algorithms to multi-processor systems.

Bibliography

- [1] Macrae, J. D., “Development and Verification of a Resin Film Infusion/Resin Transfer Molding Simulation Model for Fabrication of Advanced Textile Composites”, Master’s thesis, Virginia Polytechnic Institute and State University, (1994).
- [2] Chen, V., A. Hawley, M. Klotzsche, A. Markus, and R. Palmer, “Composite Technology for Transport Primary Structure”, in *First NASA Advanced Composite Technology Conference*, pp. 71–126, (1990).
- [3] Fracchia, C. A., J. Castro, and C. L. Tucker, “A Finite Element/Control Volume Simulation of Resin Transfer Mold Filling”, in *Proceedings of the American Society for Composites, Fourth Technical Conference*, pp. 157–166, (1989).
- [4] Davé, R., “A Unified Approach to Modeling Resin Flow During Composite Processing”, *Journal of Composite Materials*, vol. 24 (1991), pp. 22–41.
- [5] Friedrichs, B. and S. I. Güçeri, “A Hybrid Numerical Technique to Model 3-D Flow Fields in Resin Transfer Molding Process”, *Polymer Engineering and Science*, vol. 35 (1995), no. 23, pp. 1834–1851.
- [6] Gauvin, “Permeability Measurement and Flow Simulation Through Fiber Reinforcement”, *Polymer Composites*, vol. 17 (1996), no. 1, pp. 34–42.
- [7] Loos, A. C. and J. D. MacRae, “A Process Simulation Model for the Manufacture of a Blade-Stiffened Panel by the Resin Film Infusion Process”, *Composites Science and Technology*, vol. 56 (1996), pp. 273–289.
- [8] Cai, Z. and D. J. Lawrie, “A Simplified Mold Filling Program for the RTM Process”, in *24th International SAMPE Technical Conference*, pp. T675–T686, (1992).
- [9] Boccard, A., W. I. Lee, and G. S. Springer, “Model for Determining the Vent Locations and the Fill Time of Resin Transfer Molds”, *Journal of Composite Materials*, vol. 29 (1995), no. 3, pp. 306–333.

- [10] Voller, V. R. and S. Peng, "An Algorithm for Analysis of Polymer Filling of Molds", *Polymer Engineering and Science*, vol. 35 (1995), no. 22, pp. 1758–1765.
- [11] Calhoun, D. R., S. Yalvaç, D. G. Wetters, C.-H. Wu, T. J. Wang, J. S. Tsai, and L. J. Lee, "Mold Filling Analysis in Resin Transfer Molding", *Polymer Composites*, vol. 17 (1996), no. 2, pp. 251–264.
- [12] Lee, L. J., W. B. Young, and R. J. Lin, "Mold Filling and Cure Modeling of RTM and SRIM Processes", *Composite Structures*, vol. 27 (1994), pp. 109–120.
- [13] Young, W.-B., "Three-Dimensional Nonisothermal Mold Filling Simulation in Resin Transfer Molding", *Polymer Composites*, vol. 15 (1994), no. 2, pp. 118–127.
- [14] Loos, A. C., J. D. MacRae, D. Hood, D. E. Kranbuehl, and H. B. Dexter, "Resin Film Infusion (RFI) Process Simulation of Complex Shaped Composite Structures", in *37th AIAA/ASME/ASCE/AHS/ASC Structures, Structural Dynamics and Materials Conference*, pp. 1828–1837, (April 1996).
- [15] Yoo, Y.-E. and W. I. Lee, "Numerical Simulation of the Resin Transfer Mold Filling Process Using the Boundary Element Method", *Polymer Composites*, vol. 17 (1996), no. 3, pp. 368–374.
- [16] Tucker, C. L., III, "Heat Transfer and Reaction Issues in Liquid Composite Molding", *Polymer Composites*, vol. 17 (1996), no. 1, pp. 60–72.
- [17] Dessenberger, "Thermal Dispersion in Resin Transfer Molding", *Polymer Composites*, vol. 16 (1995), no. 6.
- [18] Lin, R. J., L. J. Lee, and M. J. Liou, "Mold Filling and Curing Analysis in Liquid Composite Molding", *Polymer Composites*, vol. 14 (1993), no. 1, pp. 71–81.
- [19] Chen, Y.-T. and C. W. Macosko, "Chemorheology of Polycyanate for Resin Transfer Molding", in *24th International SAMPE Technical Conference*, pp. T630–T644, (1992).
- [20] Castro, J. M. and C. W. Macosko, "Studies of Mold Filling and Curing in the Reaction Injection Molding Process", *AICHE Journal*, vol. 28 (1982), no. 2, pp. 250–260.
- [21] Reddy, J. N., *An Introduction to the Finite Element Method*, McGraw Hill, Inc., New York, (1993).
- [22] Somanath, N. and A. C. Loos, "A Finite Element Cure Model and Cure Cycle Optimization of Composite Structures", Tech. Rep. CCMS-88-14, Virginia Tech Center for Composite Materials and Structures, (1988).

- [23] Osswald, T. A. and C. L. Tucker, "Compression Mold Filling Simulation for Non Planar Parts", *International Polymer Processing V*, (1990), pp. 79–87.
- [24] Baddourah, M. A., "Vector Sparse Solver (VSS) FORTRAN code", Written for NASA Langley. Contact Olaf Storaasli at NASA Langley for further information.
- [25] Dexter, H. B., R. J. Palmer, and G. H. Hasko, "Mechanical Properties and Damage Tolerance of Multiaxial Warp Knit Structural Elements", in *Fourth NASA/DOD Advanced Composites Technology Conference, NASA CP-3229*, (June 7–11 1993).
- [26] Hinrichs, S., R. J. Palmer, A. Ghumman, J. Deaton, K. W. Furrow, and L. C. Dickinson, "Mechanical Property Evaluation of Stitched/RFI Composites", in *Fifth NASA/DOD Advanced Composites Technology Conference, NASA CP-3294*, (August 22–25, 1994).
- [27] Furrow, K. W., "Material Property Evaluation of Braided and Braided/Woven Wing Skin Blade Stiffeners", Contractor Report 198303, NASA, (April 1996).
- [28] Fingerson, J. C., A. C. Loos, and H. B. Dexter, "Verification of a Three-Dimensional Resin Transfer Molding Process Simulation Model", Tech. Rep. CCMS-95-10, Virginia Tech Center for Composite Materials and Structures, (September 1995).
- [29] Weideman, M. H., "An Infiltration/Cure Simulation Model for Manufacture of Fabric Composites by the Resin Infusion Process", Master's thesis, Virginia Polytechnic Institute and State University, (1992).
- [30] Hammond, V. H., A. C. Loos, H. B. Dexter, and G. H. Hasko, "Verification of a Two-Dimensional Infiltration Model for the Resin Transfer Molding Process", Tech. Rep. CCMS-93-15, Virginia Tech Center for Composite Materials and Structures, (September 1993).
- [31] Loos, A. C., M. H. Weideman, J. Edward R. Long, D. E. Kranbuehl, P. J. Kinsley, and S. M. Hart, "Infiltration/Cure Modeling of Resin Transfer Molded Composites Using Advanced Fiber Architectures", in *First NASA Advanced Composite Technology Conference*, pp. 425–441, (1990).

Appendix A

Detailed Drawings of Tooling Components

Detailed Drawings of Tooling Components

A.1 Stepped Panel Tooling Schematics

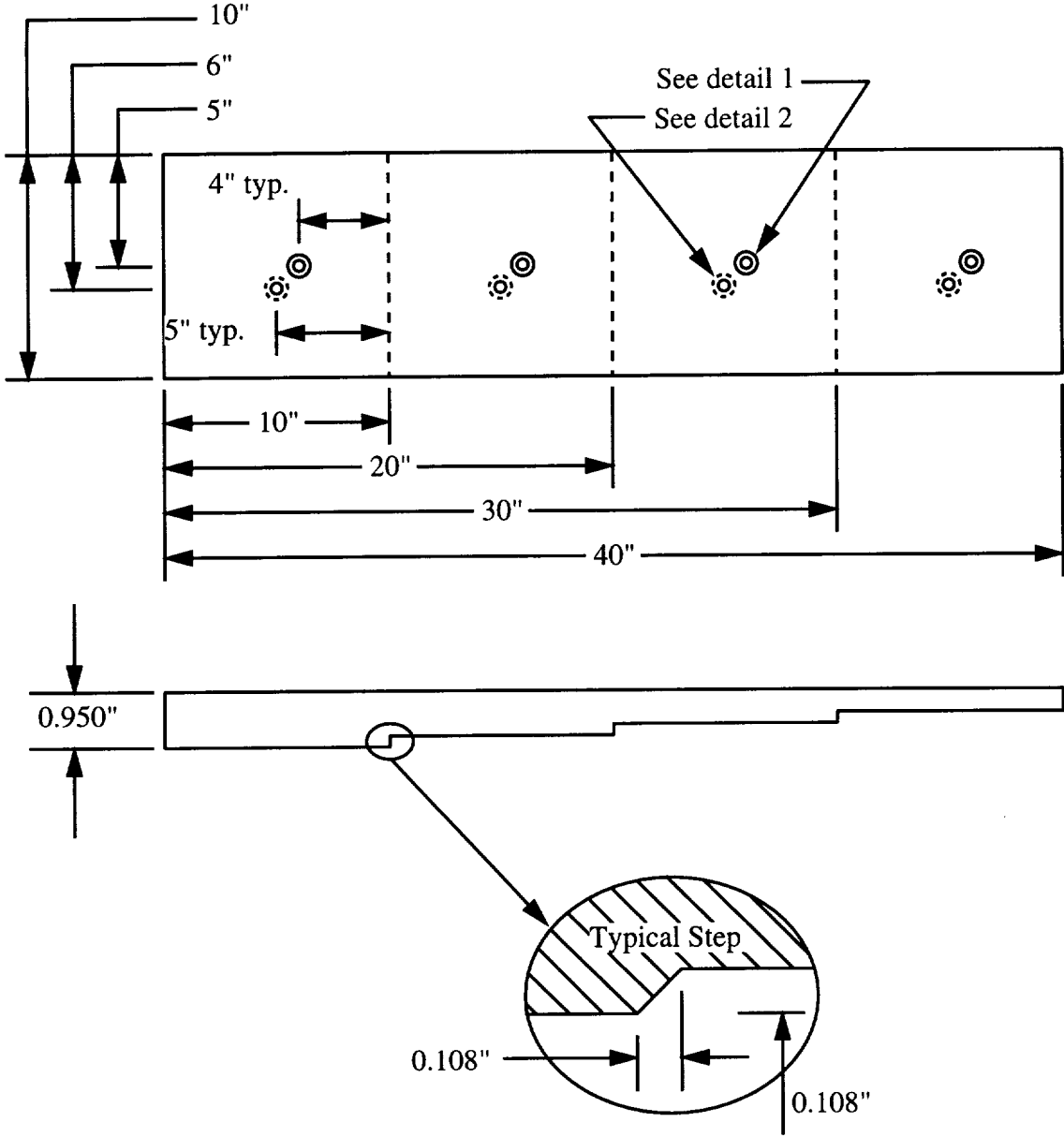
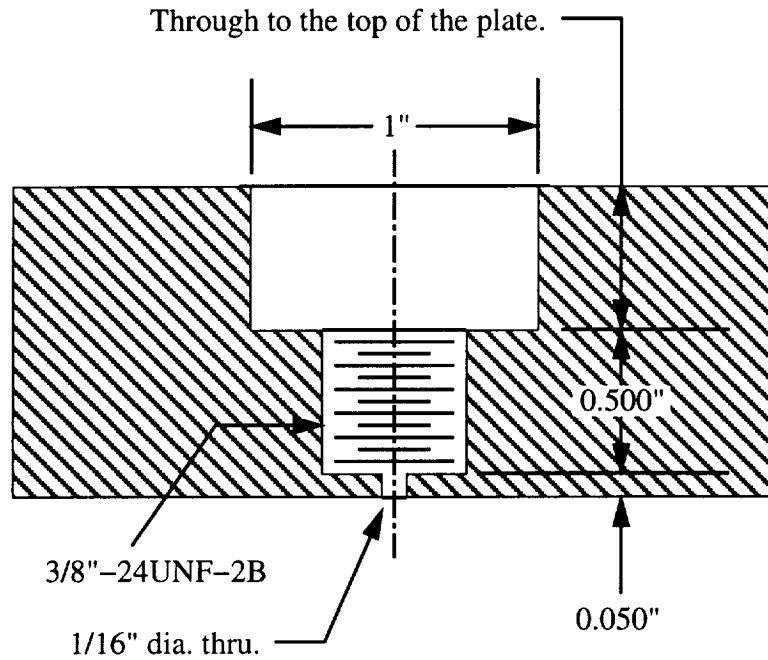


Figure A.1: Baseplate.

Detail 1: Pressure Transducer Tap



Detail 2: FDEMS Tap

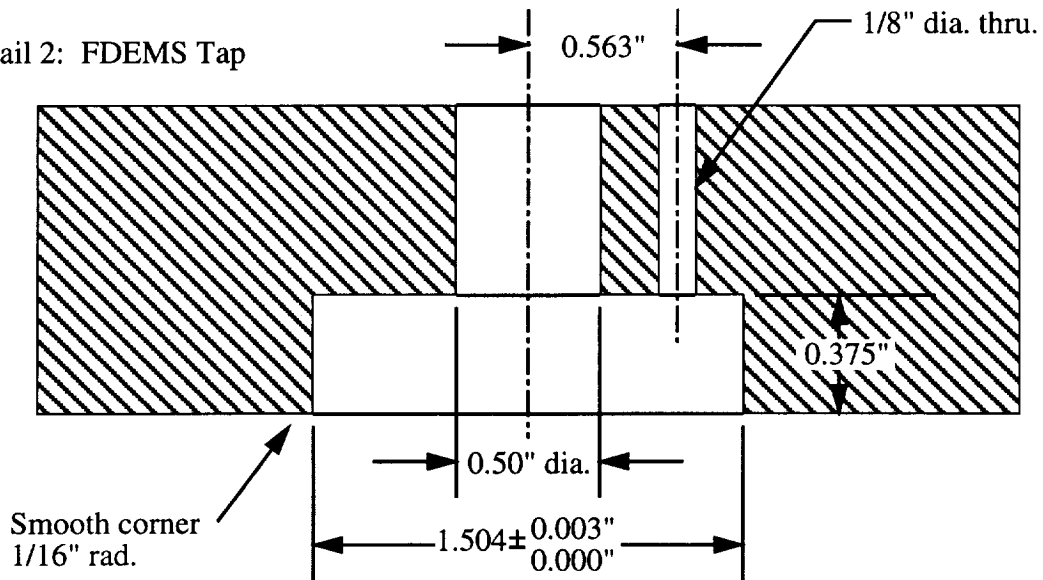
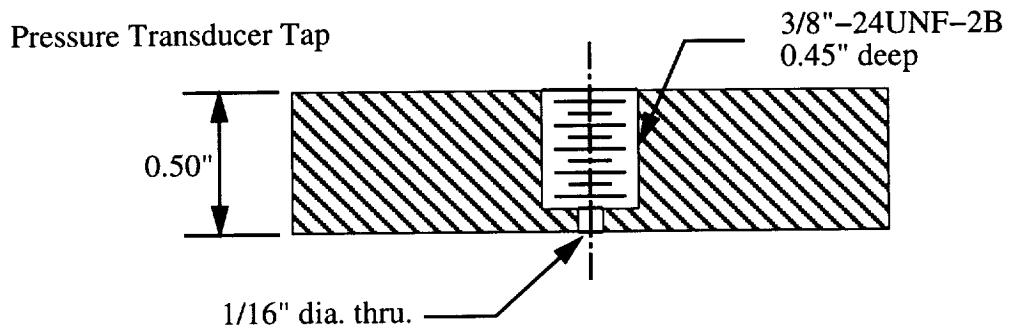
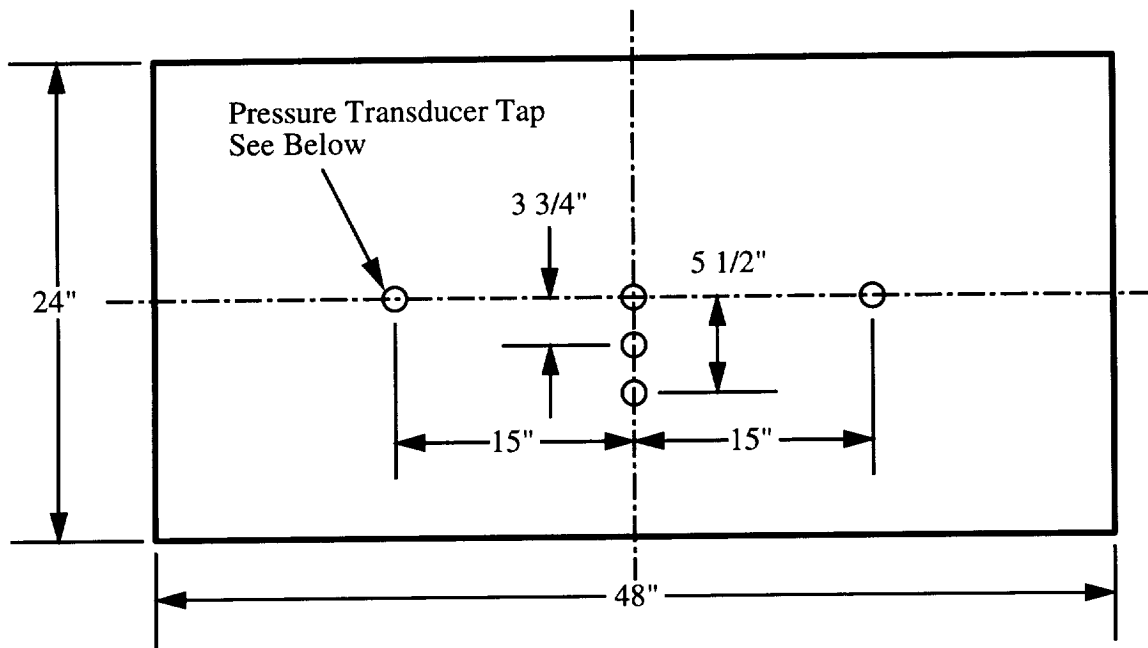


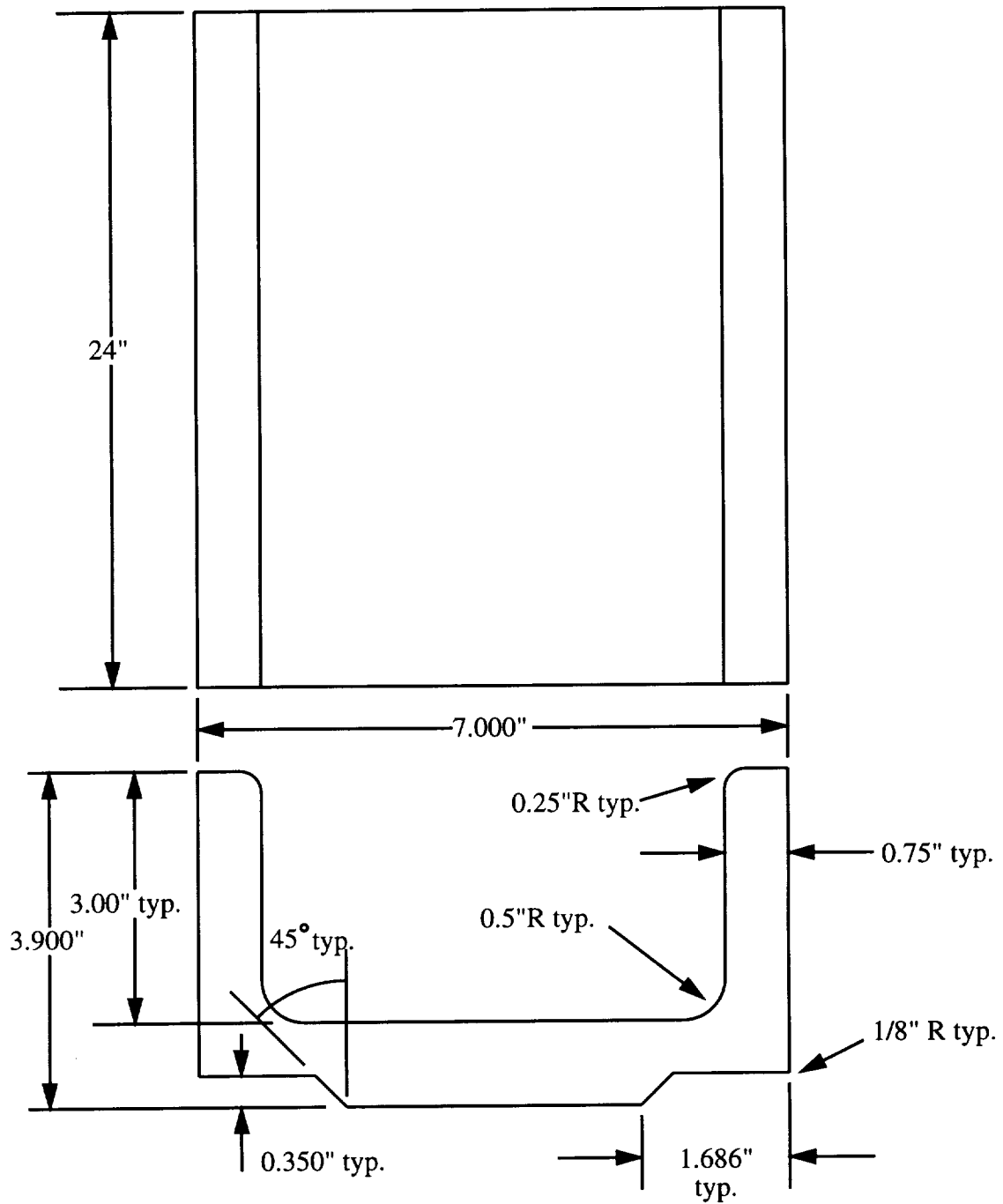
Figure A.2: Detailed drawings of the sensor tap geometry.

A.2 Two Stringer Panel Tooling Schematics



Material: Aluminum

Figure A.3: Baseplate for the two stiffener panel.



Material: 6061-T6

Figure A.4: Middle tool for the two stiffener panel. See Figure A.5 for sensor locations.

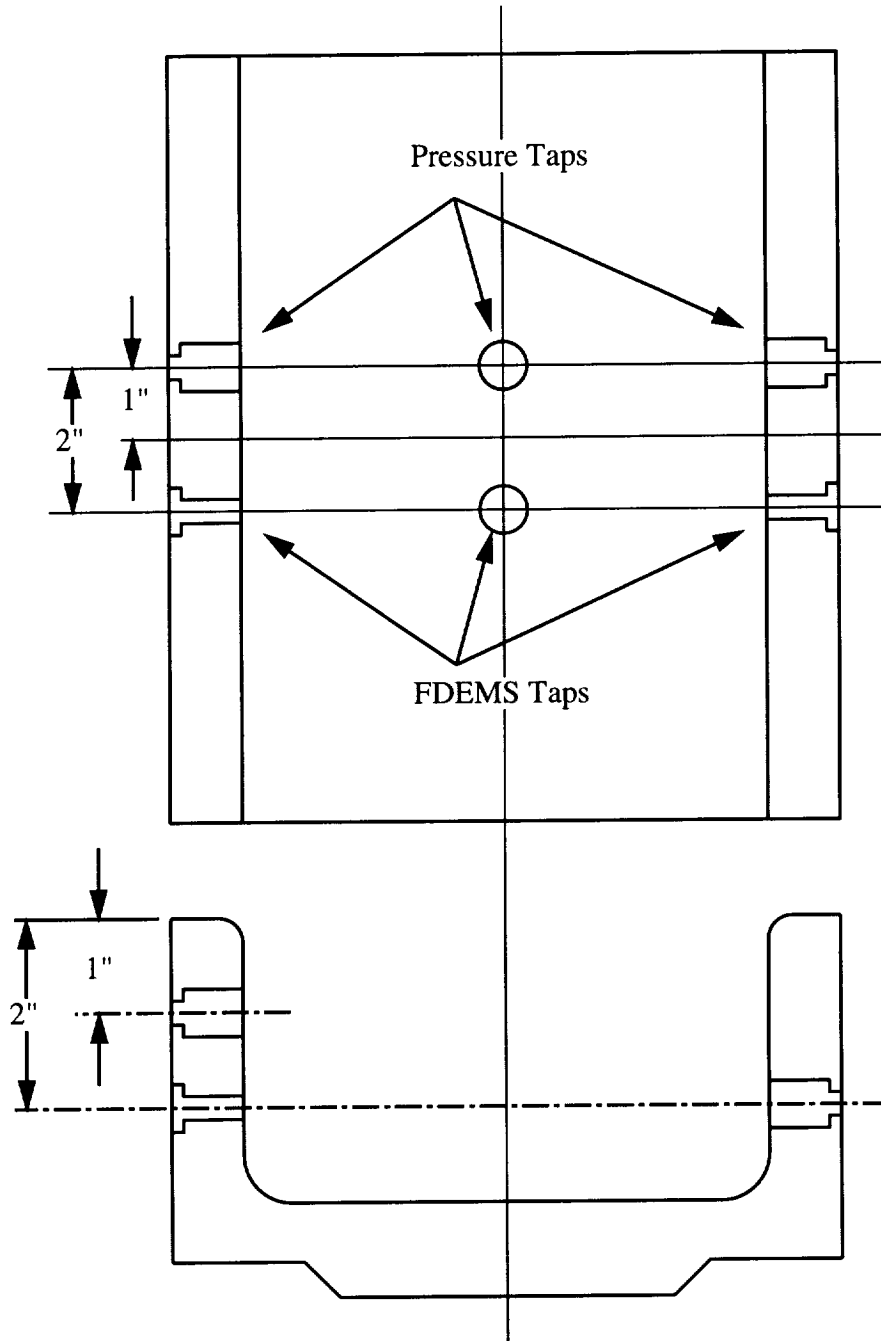
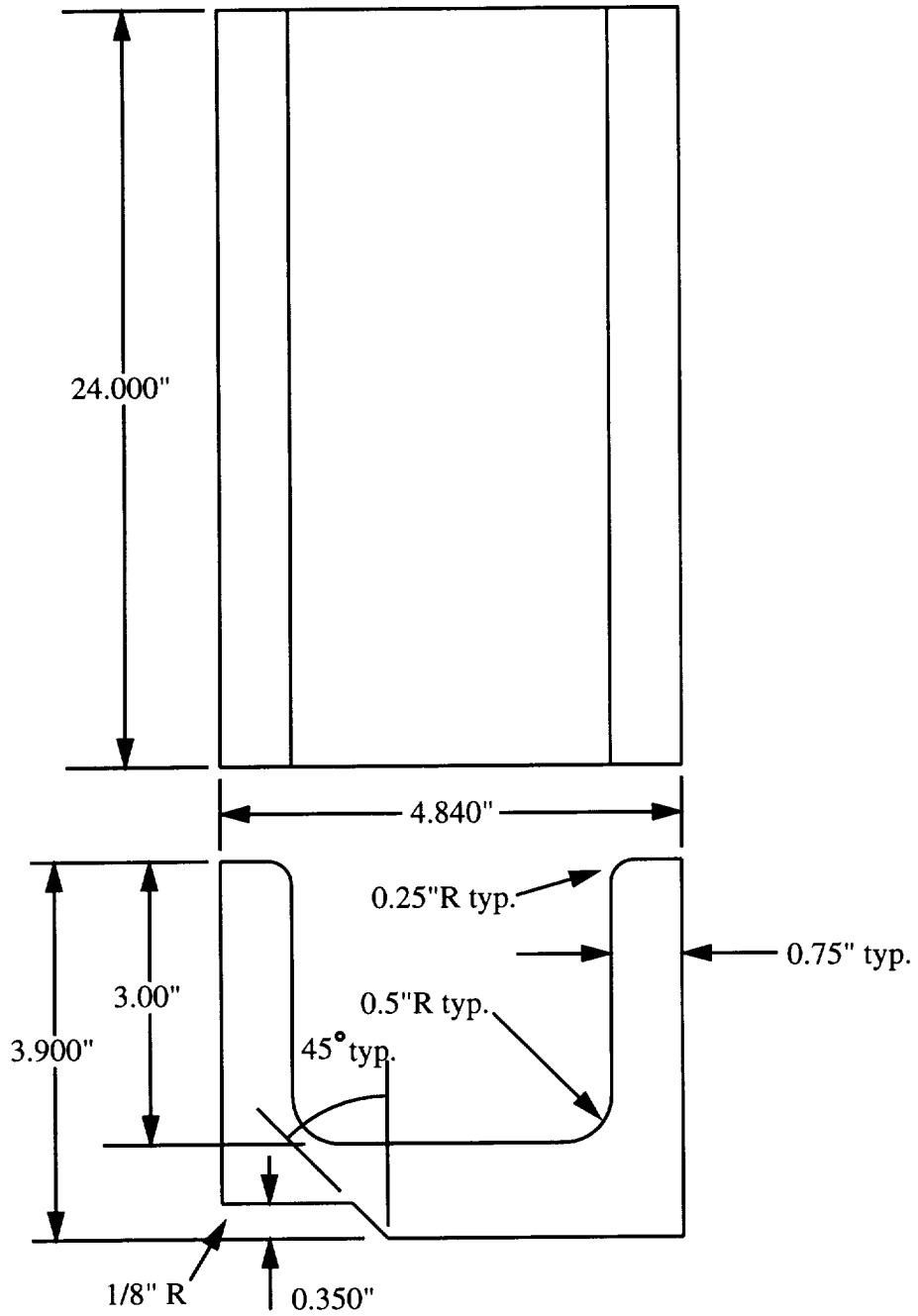


Figure A.5: Sensor locations for the two stiffener panel.



Material: 6061-T6

Figure A.6: End tool for the two stiffener panel.

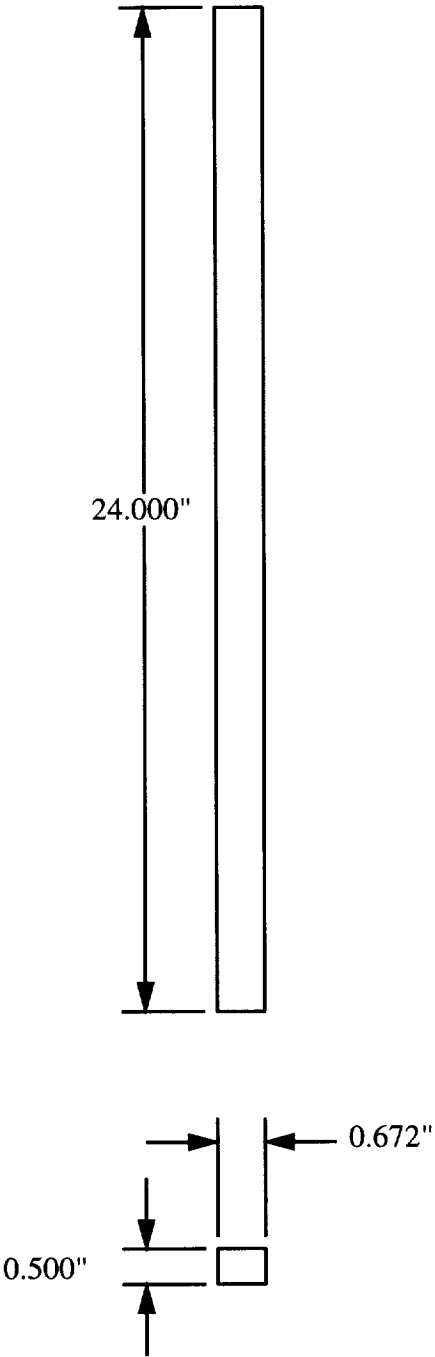


Figure A.7: Shim for the two stiffener panel.

Appendix B

Material Properties

Material Properties

B.1 Flow Properties

B.1.1 FVF

The fiber volume fraction (FVF) fit equation is:

$$v_f = a_0 + a_1p + a_2p^2 + a_3p^3 + a_4p^4 \quad (\text{B.1})$$

where v_f is the FVF, a_i are the fit constants, and p is the pressure measured in kPa. Equation (B.1) is valid up the pressure ' p_{max} ' listed in the following table.

Note: The fit constants give a value for total FVF of the preform, not the carbon FVF. The total FVF must be used as input to the permeability fits in the next section.

	a_0	a_1 $\times 10^{-4}$	a_2 $\times 10^{-7}$	a_3 $\times 10^{-10}$	a_4 $\times 10^{-14}$	p_{max} (kPa)
Tenax 8 Stack Warp Knit	0.50742	4.45047	-5.86561	3.57627	-8.12660	1515.
AS4	0.52491	3.23476	-4.19359	2.79126	-7.11793	1450.
14 Tube Braid	0.55653	3.87254	-10.6127	15.6092	-82.2488	801.
4 Tube Braid	0.52363	5.23703	-11.8842	13.6207	-57.6054	922.

B.1.2 Permeability

The following equation is used to calculate permeabilities:

$$S = a(v_f)^b \quad (\text{B.2})$$

where S is the permeability in m^2 , v_f is the FVF, and a and b are the fit constants listed in the following table.

To calculate the permeabilities at plus/minus one standard deviation, use:

$$S \pm \sigma = \exp [\ln (av_f^b) \pm \sigma'] \quad (\text{B.3})$$

where σ' is the value listed in the following table.

	a	b	σ'
Tenax 8 Stack Warp Knit ¹			
to stitching	9.03×10^{-15}	-12.18	0.1693
⊥ to stitching	3.27×10^{-15}	-12.53	0.2800
TTT	1.26×10^{-14}	-7.95	0.1447
AS4 6 stack ² .2" 1/8"			
to stitching	1.1×10^{-15}	-16.912	-
⊥ to stitching	3.5×10^{-16}	-16.041	-
TTT	2.6×10^{-14}	-6.81	-
14 Tube Braid ¹			
to stitching	4.76×10^{-16}	-18.26	0.1949
⊥ to stitching	1.36×10^{-16}	-19.76	0.1477
TTT	-	-	-
4 Tube Braid			
to stitching ³	2.5×10^{-15}	-16.05	-
⊥ to stitching ¹	9.8×10^{-16}	-15.88	-
TTT ¹	5.88×10^{-15}	-8.63	0.1127

¹Tamara Knott

²Tamara Knott, 8/19/97

³Tamara Knott, 9/8/97

B.2 Thermal Properties

	Conductivity $W/(mK)$	ρ Kg/m^3	c_p $J/(Kg^\circ C)$	ρc_p $10^6 J/(m^3^\circ C)$
Aluminum 6061-T6	152	2700	831 ⁴ -963 ⁵	2.243-2.600
Carbon Epoxy OML Tool ⁶	6.09 in plane 0.61 TTT	-	-	1.852
Preform ⁶	0.822 in plane 0.082 TTT	-	-	1.267
Glass Fiber	0.865 ⁷ -1.0817 ⁸	2490 ⁷ -2540 ⁸	711.76 ⁷ -824.96 ⁸	1.772-2.095
Glass Cloth ⁹	0.0335	2560	670	1.715

B.3 Mechanical Properties

	Coefficient of Thermal Expansion			Elastic Modulus			Shear Modulus			Poisson's Ratio		
	α_{11}	α_{22}	α_{33}	E_{11}	E_{22}	E_{33}	G_{12}	G_{23}	G_{31}	ν_{12}	ν_{23}	ν_{13}
	$(\times 10^{-6}/^\circ C)$			(GPa)			(GPa)					
Aluminum 6061-T6 ¹⁰	22.59			68.26			-			.33		
Carbon Epoxy OML Tool	3.5	3.5	45-50	46	46	8	5-6	-	-	0.1	-	-
AS4/IM7 Saertex 11= to stitching 22= \perp to stitching 33=TTT	?0.1?			83.6	35.5	11.0	17.1	33.6	33.6	.403	.390	.390
Bleeder and Breather ¹¹	5.1			72.4			-			-		

⁴Machinists Handbook

⁵Kim Rohwer

⁶From Doug MacRae

⁷Fiber Properties: Dr. Loos' Homework, Spring 1995, Set #5

⁸Fiber Properties: BGF Industries, Inc. Greensboro, NC

⁹Young, 1994 Polymer Composites

¹⁰Mill's Handbook, Vol. 5, Nov. 1994

¹¹BGF